PERMANENT MAGNET MACHINE DESIGN WITH COLD SPRAY MAGNETS

Sumeet Singh

A Thesis

In the Department

of

Electrical and Computer Engineering

Presented in Partial Fulfillment of the Requirements

For the Degree of

Doctor of Philosophy (Electrical and Computer Engineering) at

Concordia University

Montréal, Québec, Canada

May 2022

CONCORDIA UNIVERSITY

SCHOOL OF GRADUATE STUDIES

This is to certify that the thesis prepared

By: Sumeet Singh

Entitled: Permanent Magnet Machine Design with Cold Spray Magnets

and submitted in partial fulfillment of the requirements for the degree of

Doctor of Philosophy (Electrical and Computer Engineering)

complies with the regulations of the University and meets the accepted standards with respect to originality and quality.

Signed by the final examining committee:

_____Chair
Dr. Yousef R. Shayan

_____External Examiner
Dr. Joseph Olorunfemi Ojo

_____External to program
Dr. Ramin Sedaghati

_____Examiner
Dr. Chunyan Lai

_____Examiner
Dr. Luiz. A.C. Lopes

_____Thesis Supervisor
Dr. Pragasen Pillay

Approved by: _____

Dr. Wei-Ping Zhu, Graduate Program Director

May 16th, 2022

_____

Dr. Mourad Debbabi, Dean,
Gina Cody School of Engineering and Computer Science

ABSTRACT

Permanent Magnet Machine Design with Cold Spray Magnets

Sumeet Singh, Ph.D.

Concordia University, 2022

With the global trend toward electrification of transport, the interest in various configurations of electric motors is growing. Surface permanent magnet synchronous machines (SPMSM) are used in many high-performance applications due to low inertia, high torque density, and overload capability. Several applications require low torque pulsations as they can lead to mechanical vibrations and acoustic noise in the electric motor. Various techniques have been proposed in the literature to reduce the torque pulsations either by using machine control strategies or by machine design. Optimization of the rotor permanent magnet (PM) shape is one of the effective methods for reducing torque pulsations. Unfortunately, the low versatility of the motor magnet fabrication technologies limits the development of new motor geometries. Current techniques used for the assembly of PMs in motors such as adhesives, slots, or screws are complex, labor-intensive, and offer very little flexibility for advanced motor design geometries. Consequently, alternative fabrication techniques such as cold spray additive manufacturing are worth exploring. Cold spray additive manufacturing is used for shaping PMs for the direct fabrication of electric motor parts without the need for additional assembly steps. This novel technique allows an increase in the design flexibility of electrical machine geometries targeting improved performance.

In this thesis, the PM rotors considered are the conventional rectangular-shaped with unskewed magnets (Model A), skewed magnets (Model B), and sinusoidal-petal-shaped magnets (Model C) along the axial direction. The magnitude of magnetization current pulse required to magnetize these rotors is calculated using an FEA package and an impulse magnetizer setup is designed and prototyped for in-situ magnetization. Various stator terminal connection configurations are analyzed and compared for the magnetizer. The performance of the shaped cold sprayed permanent magnet rotors and their effects on back EMF, electromagnetic torque, and cogging torque are analyzed experimentally and comparisons are made between the different rotor designs.

Laminated electrical silicon steel sheets are mainly used to produce the stator and rotor core of an electrical machine. In comparison, there are soft magnetic composites (SMC) which consist of a high purity fine iron powder particle coated with the insulation material. Hence, its electrical resistance is much higher than that of laminated steel. Its isotropic magnetic and physical properties help flux to conduct in a three-dimensional direction and effectively dissipate the heat produced from core losses. The product developed using SMC material uses compaction, heating, and pressing techniques to achieve the desired shape and final size of the machine core parts. Hence, the material wastage is lower as compared to the laminated steel core.

In this thesis, the impact of a few manufacturing parameters on SMC properties to ensure that optimized motor performance is achieved was analyzed using three SMC different materials (A, B, and C) using FEA software. Furthermore, machine design parameters are tuned to achieve optimal flux weakening. Finally, an FEA-based performance analysis of a 7.12 kW radial flux PMSM with laminated steel and SMC stator core is used to estimate the torque density and losses in the machines. Two different designs of 24/20 slot-pole and 12/8 slot-pole configuration using conventional surface permanent magnet rotor designs are considered. In addition, the ring-type Halbach-array PM rotor fabricated using cold spray additive manufacturing for 12/8 slot-pole is analyzed and optimized with the SMC stator core for high-speed electric vehicle application

ACKNOWLEDGMENT

Foremost, I would like to acknowledge and express my most sincere gratitude to my supervisor ***Dr. Pragasen Pillay*** for his invaluable guidance, motivation, immense knowledge, and continuous support throughout my Ph.D. research. I am very grateful to work with a most caring advisor and mentor during my Ph.D. program. I also would like to thank him for his financial support and letters of recommendation.

Besides my supervisor, I would like to thank the rest of my thesis committee: ***Dr. Chunyan Lai, Dr. Luiz A.C. Lopes, Dr. Ramin Sedaghati, and Dr. Joseph Olorunfemi Ojo*** for their encouragement, insightful comments, and valuable time.

My sincere thanks also go to ***Dr. Mathews Boby*** for all his comments and advice during my research and for writing this thesis. I thank my fellow lab mates in the power electronics and energy research (PEER) group: ***Mohanraj Muthusamy, Tamanwè Payarou, Rajendra Thike, and Cyusa Christophe*** for their help with the experimental measurements and technical discussions.

My sincere appreciation goes to all the members of the CRD project for their consultation, motor prototyping, and technical support especially ***Dr. Maged Ibrahim, Dr. Fabrice Bernier, Dr. Jean-Michel Lamarre, and Dr. Serge Grenier***.

I would like to extend many thanks to my dearest friends ***Aditya Kumar Bhatt, Seyedeh Nazanin Afrasiabi, Yupeng Liu, Bigyan Basnet, Manisha Verma, and Ashutosh Patel*** for their valuable friendships, lunch, coffee, and the fun times in Montreal. I also would like to thank all the other members of the PEER group.

Last but not the least, I would like to acknowledge and thank my biggest source of encouragement, all my family members for their unconditional support and love throughout my whole life.

This research work is done as a part of the InnovÉÉ/NSERC CRD Project entitled "Novel permanent magnet motor topologies using advanced magnetic materials". This research work is done as part of the NSERC/Hydro-Quebec Senior Industrial Research Chair entitled "Design and

Performance of Special Electrical Machines" held by Professor Pragasen Pillay at Concordia University, Montreal. This research is also partly funded by the NSERC Discovery Grant entitled "Novel Electric Machine Design Topologies for Electrified Transportation". I would like to acknowledge the support of the National Research Council of Canada (NRC).

DEDICATION

This Ph.D. thesis is dedicated to my parents

Bijay Kumar Singh

and

Renu Singh

for their endless love, support, and encouragement

TABLE OF CONTENTS

LIST OF FIGURES

LIST OF TABLES

LIST OF ABBREVIATIONS

EV	Electric vehicles
HEV	Hybrid electric vehicles
PM	Permanent magnet
ICE	Internal combustion engine
RFPM	Radial-flux permanent magnet
REO	Rare earth oxide
SmCo	Samarium-cobalt
NdFeB	Neodymium iron boron
AlNiCo	Aluminum nickel cobalt
FEA	Finite element analysis
UTS	Ultimate tensile strength
NES	Non-grain-oriented electrical steel
SMC	Soft magnetic composite
SPMSM	Surface permanent magnet synchronous machines
AM	Additive manufacturing
SRM	Switched reluctance motor
MEC	magnetic equivalent circuit
FEM	Finite element method

THD	Total harmonic distortion
IPM	interior permanent magnet
CPSR	constant-power speed range

LIST OF SYMBOLS

H	Magnetic field strength
μ_r	Relative permeability
B	Magnetic flux density
μ_O	Permeability of free space
BH_{max}	Maximum energy product
B_r	Remanence flux density
P_{cu}	Copper loss
R_{cu}	Winding resistance
I	RMS value of the stator current
ω_e	Angular frequency
P_{iron}	Total iron loss density
P_h	Hysteresis loss
P_e	Eddy current loss
k_h	Hysteresis constants
k_e	Eddy current constants
β_{st}	Steinmetz constant
λ	Flux linkage
N	Number of turns of wire
ϕ_g	Air gap flux
θ_e	Rotor position

B_g	Air gap flux density
A_g	Air gap cross-sectional area
R_{ro}	Air gap radius at the magnet surface
θ_p	Angular pole pitch in rad mech
L_{stk}	Stack length
K_e	Back EMF constant
K_t	Torque constant
ϕ_m	Magnetic flux
I_{mag}	Magnetization current
B_m	Magnetic flux density
$\Re_r$	Rotor core reluctance
$\Re_s$	Stator core reluctance
$\Re_l$	Leakage reluctance
$\Re_g$	Air-gap reluctance
$\Re_m$	Magnet reluctance
L_s	Stator inductance
R_s	Stator resistance
I_p	Peak current
R_{eff}	Effective resistance
l_m	Length of the magnet
P_c	Permeance coefficient

g	Air gap length
C_φ	Flux concentration factor
l	Flux path length
μ	Permeability of the material
w_{tb}	Stator tooth width
w_{bi}	Back iron width
φ_g	Air gap flux
B_{max}	Maximum flux density
k_{st}	Lamination stacking factor

CHAPTER – 1

INTRODUCTION

This chapter presents a literature review of permanent magnet electric motors for electric vehicle applications. It presents an overview of magnetic materials, surface-mounted rotor permanent magnet shaping, and cold spray additive manufacturing techniques. It introduces soft magnetic composite materials and their properties along with the organization of the dissertation and original contributions.

1.1. Introduction to Permanent Magnet Electric Machines for Electric Vehicles

Electric vehicles (EVs) and hybrid electric vehicles (HEVs) have emerged as viable alternative solutions in the transportation sector to replace the dependency on fossil fuels and reduce emissions. Electric machines especially for traction applications require high power density, high torque density, high efficiency, high reliability, low cost, low torque ripple, vibration, noise, etc. [1-3]. Therefore, permanent magnet (PM) based electric machines are one of the most prominent choices for traction machines. The production volume of the motor vehicle has increased tremendously in the automotive industry since the 1950s, as shown in Fig. 1.1 [4]. The top 10 motor vehicle-producing countries all over the world are shown in Fig. 1.2 [4]. In recent years, the sales and production of electric vehicles have also increased due to an increase in geopolitical awareness, notable incentives from the government, and lower costs to run. Therefore, the research in the field of machine design to achieve high performance and efficiency is an interesting topic for the benefit of the automotive industry. It is predicted that looking at the present electric car revolution, by 2025, EVs will be as cheap as gasoline-based cars. By 2038, EV sales shall overtake internal combustion engine (ICE) cars [5].

Designing an electric machine is a challenging task as its electromagnetic, thermal, and mechanical performances are coupled and need to be taken into consideration together at the same time. The performance of the electric machine can be improved by using thinner electrical steel laminations and lower air gap width, but these attributes increase the cost and manufacturing

difficulties of the machines. A lot of research has been done in the past years with the focus on designing electric machines to improve their performance, making the batteries last longer, and making the control drives more efficient. The motor operation is optimized such that it produces the least amount of losses in the whole drivetrain. In the current years, the advancement in artificial intelligence technology has led to self-driving cars like Tesla Model S and Model X which are been efficient with have fast charging capabilities. Manufacturers like Ford, Toyota, General Motors, BMW, and Volkswagen are producing such electric vehicles. A comparative analysis of various EVs is tabulated in Table 1.1 [7 – 9]. Before going into details of electric machine design and to get a better understanding of the structure of electric vehicles, Fig. 1.3 shows an overview of a Tesla Model S car [6]. It consists of an electric motor, a control unit to drive the motor, a battery pack with a battery management unit, etc.

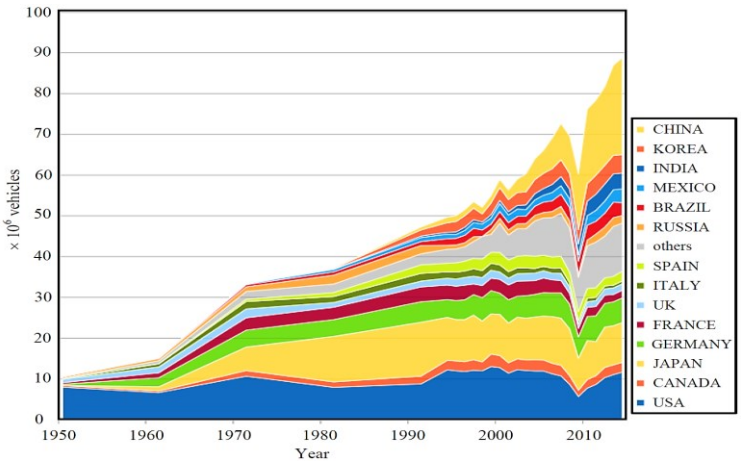

Fig. 1.1: World motor vehicle production [4]

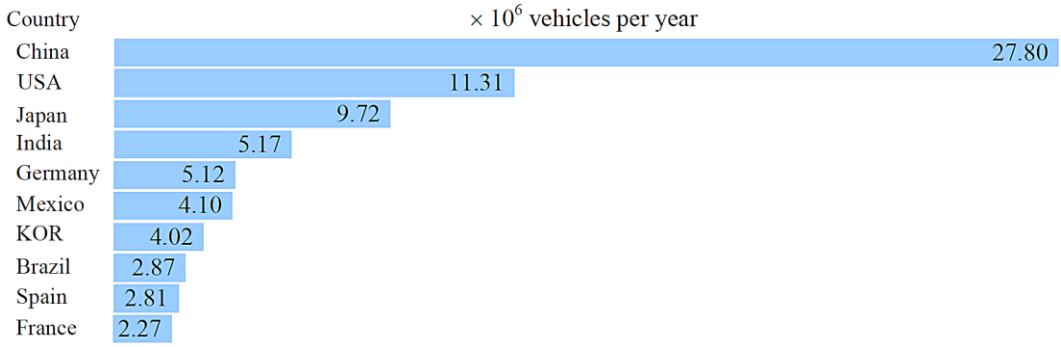

Fig. 1.2: Top 10 motor vehicle producing countries 2018 [4]

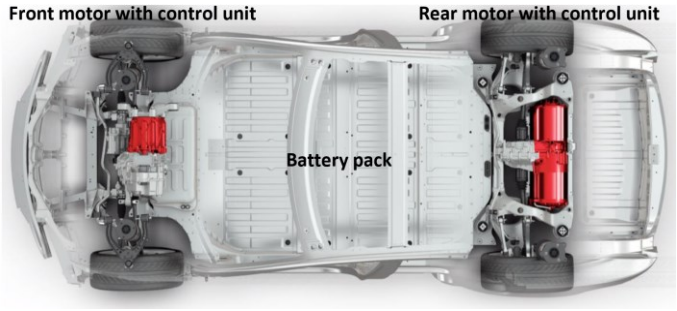

(a)

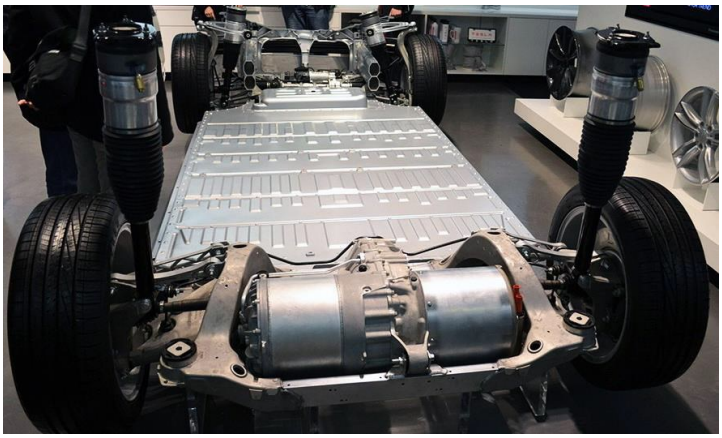

(b)

Fig. 1.3: Basic structure of an electric vehicle. (a) Overview of Tesla Model S car (b) Actual base of Tesla Model S car with an electric motor, control unit, and battery pack [6].

At the center of the vehicle and below the seats, the battery pack with the required series and parallel configurations is placed. Therefore, it offers two great advantages, first, the whole vehicle has a lower center of gravity which makes the vehicle more stable, and second, it does not occupy space in the back and front of the vehicle. The radial-flux permanent magnet synchronous machines (RFPM) are the most commonly used machines for traction applications. Fig. 1.4 shows the front and side views of an RFPM machine with its direction of the magnetic flux path and coil current direction. The magnetic flux flows in the radial direction whereas the current in the coil flows in the axial direction. RFPM machines are cheaper and simpler to manufacture compared to other types like axial-flux or transverse flux machines as they have a similar stator to the ones of the induction machines. There are two possible configurations to manufacture RFPM machines either as inner-rotor or outer-rotor assembly as shown in Fig. 1.5 (a) and (b) respectively.

TABLE 1.1: ELECTRIC VEHICLE COMPARISON BY MANUFACTURERS [7 – 9]

Vehicle model	*Motor type*	*Motor size (kW)*	*Torque (Nm)*
Ford focus electric	Permanent magnet	107	249
Kia soul electric	Permanent magnet	81	157
Hyundai IONIQ electric	Interior permanent magnet	88	295
Nissan leaf	Permanent magnet	80	157
Volkswagen e-golf	Permanent magnet	100	290
Tesla model 3 (base)	Permanent magnet	228	563
BMW i3	Permanent magnet	127	249
Tesla model X	Induction	193	249
Mercedes B250e	Permanent magnet	87	187

For surface RFPM machines, permanent magnets are placed and assembled on the surface of the rotor. The major advantage of the surface RFPM machine is its lower construction cost compared to other PM machines. The drawback of the surface RFPM is the direct exposure of the permanent magnets to the demagnetization field. Moreover, surface permanent magnets experience centrifugal forces which increase with the shaft speed and can cause magnet poles to get move from the rotor core.

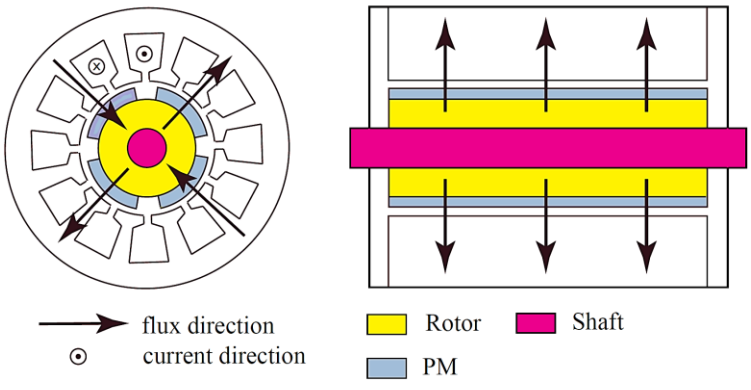

Fig. 1.4: Front and side views of a radial–flux PM machine with magnetic flux and coil current flow direction [10]

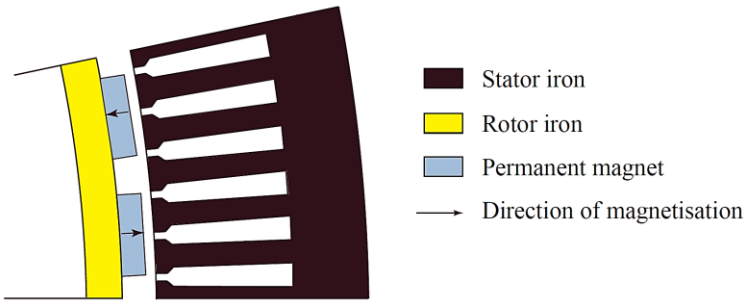

(a)

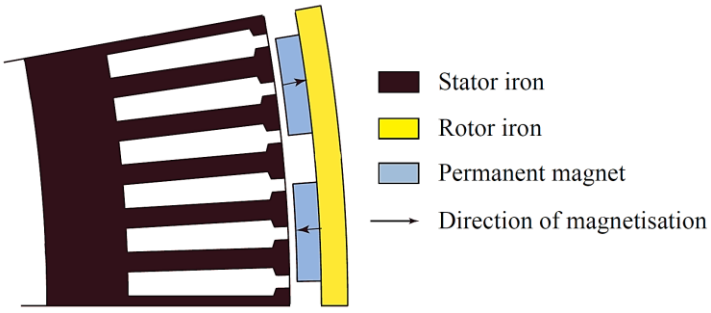

(b)

Fig. 1.5: Surface radial – flux PM machine. (a) Inner – rotor configuration. (b) Outer – rotor configuration [10].

For outer-rotor configurations, the outer diameter of the rotor is larger than the inner rotor hence, it can accommodate a high number of magnet poles. Furthermore, the centrifugal forces acting on the magnet poles of the outer-rotor configuration help it from getting detached. This type of configuration is more suitable for wind turbine applications as its rotating blades can be directly connected to the hub assembly of the outer rotor. Another configuration of RFPM machines is the inset-PM type rotor, where the permanent magnet poles are placed on the rotor core surface such that the space between the poles is filled with the iron core. The iron core between the permanent magnets creates a saliency and produces a reluctance torque in addition to the magnet torque. The RFPM with the inset-PM rotor is shown in Fig. 1.6 (a). When the permanent magnet poles are completely buried inside the rotor core laminations, it is called a buried-PM type rotor. The benefit of the buried-PM configuration compared to the surface-mounted PM is the possibility to concentrate the magnetic flux produced by the permanent magnets in the rotor core. This will help to achieve higher air-gap magnetic flux density in the machine.

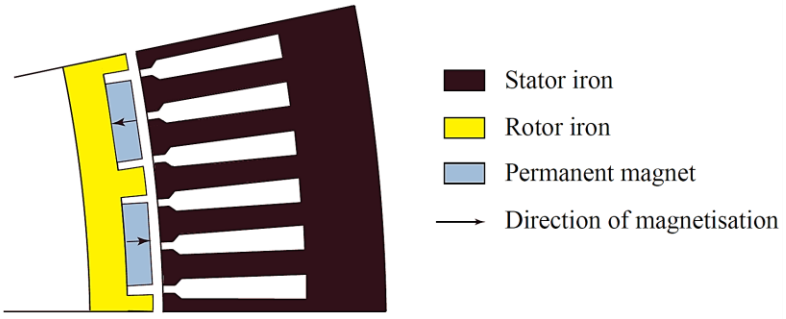

(a)

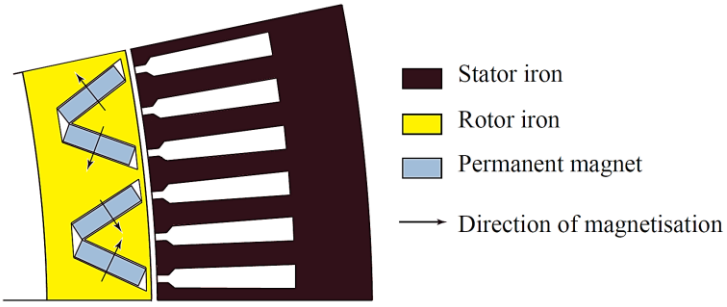

(b)

Fig. 1.6: Radial – flux PM machine. (a) Inset – PM rotor configuration. (b) Buried – PM rotor configuration [10].

The benefit of the buried-PM configuration compared to the surface-mounted PM is the possibility to concentrate the magnetic flux produced by the permanent magnets in the rotor core. This will help to achieve higher air-gap magnetic flux density in the machine. Furthermore, the permanent magnet poles experience lower centrifugal force and mechanical stress, also the possibility of demagnetization is reduced. There are various ways to arrange permanent magnet poles inside the rotor core but one of the most common configurations is the V-shaped buried-PM configuration as shown in Fig. 1.6 (b). The drawback of the buried-PM rotor configuration is magnetic flux leakage through the iron barrier and bridges. The thickness of the lamination bridges is constrained by the mechanical strength of the material. Therefore, these magnetic fluxes which leak through the bridges instead of flowing through the air gap do not contribute to the torque production. Moreover, the high number of pole designs is not possible due to the smaller area available inside the rotor core and the angle between the V-shaped buried-PM. If the angle between the V-shaped PM is small then the rotor core may get saturated easily. The production cost of the

buried-PM type rotor is higher compared to surface and inset-PM rotor due to their rotor core lamination cutting.

For RFPM machines, another possible configuration is a tangential – magnetized PM rotor as shown in Fig. 1.7. The PMs and iron pieces are fixed on a non – ferromagnetic shaft such that it produces a tangential direction flux from the rotor. This configuration does not have bridges and barriers on the rotor core hence, the magnetic flux leakages are low compared to the V-shaped PM rotor configuration. There are many other design configurations of PM machines for electric vehicle applications such as axial-flux PM machines, and transverse-flux PM machines, but in this thesis, the RFPM machine with surface-mounted PM is considered for research purposes.

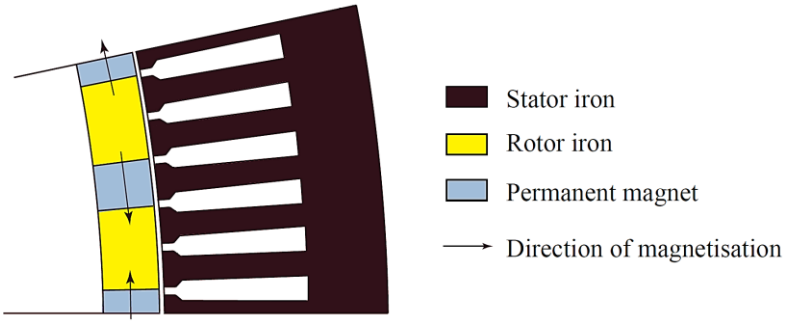

Fig. 1.7: Radial – flux PM machine with tangential – magnetized PM rotor configuration [10].

1.2. Overview of Magnetic Materials and Surface-mounted PM Machines

The permanent magnet (PM) machines are a more popular option than the induction machines in the commercial electric vehicle market [11]. The first PM-based machine was fabricated using a bar-type magnet which was very poor in quality and was not feasible to use for industrial applications. Therefore, it set an opportunity for inventors to research in the field of magnetic materials composition, powder sizes, and shapes which led to the efficient use of permanent magnets in machines today. After innumerable experimental tests and research in the 1930s, it was observed that the mixing of aluminum, nickel, and cobalt with iron produces a stronger, more efficient, and commercially viable permanent magnet called an AlNiCo magnet compared to the naturally occurring magnetite lodestone. Later during the 1950s, ceramic-type ferrite-based permanent magnets began to be used for small appliances. After a decade during the 1960s, a permanent magnet with the compounds of rare-earth metals such as samarium and cobalt

was discovered but soon later during the 1980s, it got overshadowed by the invention of the neodymium-iron-cobalt based permanent magnets. The current demand and ongoing research trend indicate that the advancement in the field of high-energy permanent magnet-based machines will continue to grow for various applications like the usage of nanocomposite permanent magnets.

Nanocomposite permanent magnets are artificially made up of nanostructured hard and soft composite materials. Fig. 1.8 shows the improvement and development of various hard permanent magnet materials and their respective maximum energy product (BH_{max}) starting from

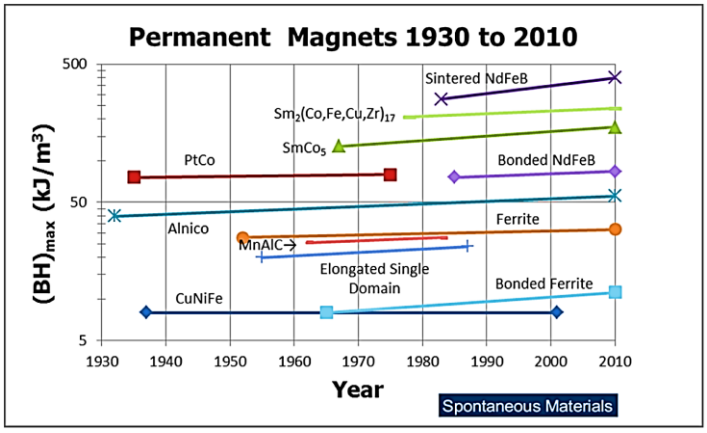

Fig. 1.8: Overview of the permanent magnet materials from the year 1930 to 2010 with their maximum energy product (BH_{max}) [12].

the year 1930 to 2010 [12]. As of now, the permanent magnet materials available in the market are almost ten times stronger than the materials available before the year 1960. The rare-earth magnets were found initially in the United States and Japan; hence these countries were the main producers of the magnetic materials. Later during the year the 1980s, the cost of the rare-earth magnet materials got reduced as a new source of these materials was discovered in China. Molycorp's mountain pass mine in California faced difficulty due to its aging infrastructure and it required a huge amount of investment. As rare earth materials were getting cheaper, the mountain pass mine was no more economically viable hence by the year 1990s China became the major producer of magnetic materials as shown in Fig. 1.9 [13].

From the year 2000 to 2005 to take benefit of cheaper manufacturing costs, most of the companies in the field of rare-earth magnet production either stopped production or relocated to

China. Due to this, the demands for the rare earth magnet increased tremendously, and supplies were in limited quantity. Therefore, China decided to reduce the export of the materials such as dysprosium, europium, and terbium during the year 2009. In March 2012, at the World Trade Organization the European Union, Japan, and the United States filed an official complaint against China's unfair trade and policy for the export of rare earth magnets [13]. In the upcoming decades as the demand is increasing due to research and the revolution of the permanent magnet-based electric machines, the cost and availability of rare earth materials will be a major concern.

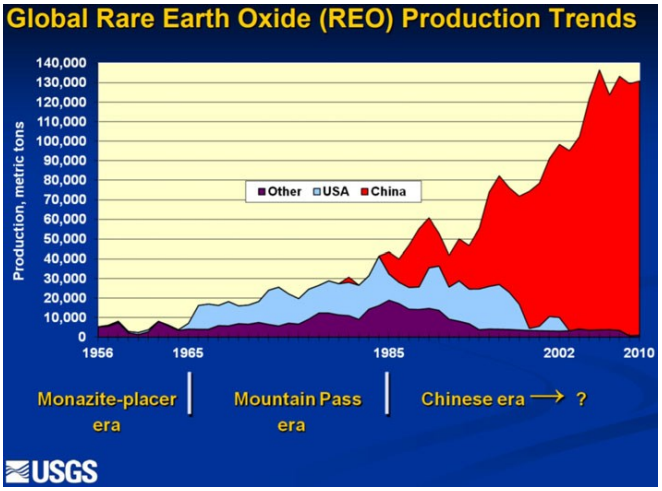

Fig. 1.9: Global rare earth oxide (REO) production trends [13].

The usage of permanent magnets for various applications has tremendously increased the development and improvement of permanent magnet materials, especially rare-earth magnets. In PM machines, field excitation is not required hence there are no excitation losses which in turn increases the overall efficiency of the machine. With the help of PM material, the magnetic flux density in the air gap is higher compared to the machine with electromagnetic excitation. The ferromagnetic materials can be categorized as soft magnetic materials and hard magnetic materials. It depends on the amount of magnetic field strength (H) needed for saturation of the material. The relative permeability (μ_r) is a measure that represents the material property of how easily it can get magnetized by an external field (H). The magnetic flux density (B) of the material is given as shown in equation (1.1) where μ_O is the permeability of free space.

$$B = \mu_O \mu_r H \tag{1.1}$$

In a soft magnetic material, the magnetic field strength (H) needed for saturation is low, and the permeability (μ_r) is high. The area enclosed by the hysteresis loop is small and hence the hysteresis losses are low. Therefore, the lamination cores made up of soft magnetic materials are suitable to complete flux paths in machines.

Hard magnetic materials such as permanent magnet materials are used in an electric machine to generate the magnetic flux in the air gap. Hard magnetic materials have low relative permeability ($\mu_r = 1$) and needs a high magnetic field for saturation. The maximum energy product $(BH)_{max}$ is used to grade the permanent magnet materials. It means that to produce a specific flux density in the machines, the highest energy product will have the smallest volume of the permanent magnet. The remanence flux density (B_r) is a measure of the permanent magnet material's residual magnetization without any external field. Therefore, the remanence of the permanent magnet defines the amount of magnetic flux it can generate. So, to obtain a high energy product, a high remanence flux density is required. The magnetic flux density of a permanent magnet is expressed by the idealized expression as shown in equation (1.2).

$$B = B_r + \mu_0 \mu_r H \tag{1.2}$$

Coercivity is another important factor of magnetic materials. It is a measure that defines the amount of reverse field required to drive the magnetization of permanent magnet material to zero after being saturated. Materials having a high coercivity means that the magnetic material can sustain a high demagnetization field. Hard magnetic materials such as permanent magnets exhibit high coercivity. The typical physical properties of various permanent magnet materials such as AlNiCo, ferrite, neodymium (NdFeB), and samarium-cobalt (SmCo) are tabulated in Table 1.2.

As mentioned in section 1.1, in the RFPM machines the magnetic flux flows in the radial direction through the air gap whereas the current flows in the axial direction. Therefore, a resulting force acting on the rotor surface is in the tangential direction. The surface-mounted PM rotor configuration for machines is as shown in Fig. 1.10. A carbon or glass fiber-based bandage is used on the rotor core surface to protect magnets from getting detached as it is subjected to high centrifugal forces. Another possible way is to use a non-magnetic steel cylinder to cover the

magnets which are stronger than the bandage. But due to the flux variations, eddy current losses will be higher in steel cylinders compared to composite bandage/ sleeves. The permeability of the

TABLE 1.2: TYPICAL PHYSICAL PROPERTIES OF MAGNETS [14].

Parameters	***Units***	***AlNiCo***	***Ferrite***	***NdFeB***	***SmCo***
Curie Temperature	℃	860	450	310-370	700-800
Max. Operating Temperature	℃	525-550	250	80-240	250
Resistivity	μΩcm	47-54	-	560-580	450-600
Hardness	Hv	520-630	480-580	160	50-90
Density	g/cm^3	6.9-7.3	4.8-4.9	7.4	8-8.5
Relative Recoil Permeability	μ rec	1.7-4.7	1.05-1.2	1.05	1.1
Saturation Field Strength	kOe	2.7-6.3	10	30-40	>37.5
	kA/m	*215-500*	*800*	*2,400-3,200*	*>3,000*

magnet is almost the same as the permeability of air hence, the q-axis and d-axis reluctances of the machine are equal. As the surface-mounted PM machines have no saliency, the total electromagnetic torque is produced by the interaction of the magnets and currents only.

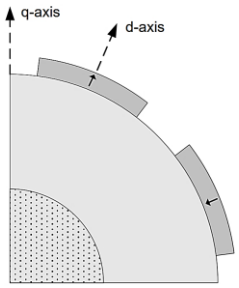

Fig. 1.10: Quarter section view of an 8-pole rotor with surface-mounted permanent magnets

The losses in the surface-mounted PM machines are iron (or core) losses and copper losses. There are also mechanical losses such as windage and bearing loss, but their magnitude is smaller compared to electrical losses. But these mechanical losses are significant and need to be considered if the rotational speed of the machine is high. The copper losses of the stator windings are given

as shown in equation (1.3) where R_{cu} is the winding resistance of one phase and I is the rms value of the stator current.

$$P_{cu} = 3R_{cu}I^2 \tag{1.3}$$

Iron losses are the losses generated due to the variation of the flux density in the machine core and it creates magnetic hysteresis and eddy currents in the iron laminations. The hysteresis loss is proportional to the peak magnitude and frequency of the flux density whereas eddy current loss is proportional to the time rate of change of the flux density. The iron (or core) losses of the machine are difficult to analyze analytically as it is generated by the time and space harmonics of the total rotating flux in the air gap. The losses in the rotor core are of less importance compared to the stator core as the flux density in it is mainly constant. Normally, a finite element analysis (FEA) is used to calculate the core losses in the machine. The sinusoidal flux density of varying frequency and magnitude (Epstein frame test) is used to measure the iron losses in the magnetic material. For a sinusoidal flux density of amplitude B with angular frequency ω_e, the total iron loss density P_{iron} is given by equation (1.4).

$$P_{iron} = P_h + P_e = k_h B^{\beta_{st}} \omega_e + k_e B^2 {\omega_e}^2 \tag{1.4}$$

where P_h and P_e are the hysteresis and the eddy current loss density respectively, k_h and k_e are hysteresis and eddy current constants and β_{st} is the Steinmetz constant. All constants depend on the iron lamination material. The friction between the rotor surface and air produces windage losses which are negligible at a moderate speed if the rotor surface area is small. The bearing losses usually depend on various factors such as its type – ceramic or ball bearing, lubrication, load on the shaft, and rotational speed of the machine.

1.3. Shaping of Rotor PM and Cold Spray Additive Manufacturing

Electric vehicles demand high torque density, overloading capabilities, lower torque pulsation, lower vibrations, and noise in the machines. The high amount of torque pulsation in machines can lead to a harsh driving experience for passengers. The spacing between the rotor PM poles, the ratio of slot width to slot pitch, PM arc angle, and the shape of the PM can be

optimized while designing the PM machines to reduce torque pulsation. Therefore, it is very important to research and develop to efficiently design the machine using rare earth PM. Torque ripple and cogging torque are two components of torque pulsation in electric machines. Cogging torque occurs due to the interaction between the slotted structure of the stator core and the rotor PMs. Various techniques have been proposed for minimizing torque pulsations in the literature. It is done either by machine control strategies in which harmonic current components are injected into windings or by different machine design geometries such as skewing, different slot openings, permanent magnet (PM) shaping, and shifting. One effective way to reduce torque pulsations is the modification and optimization of PM geometry as PM shape and its leakage flux have a significant effect on cogging torque. As the rotor rotates and moves from one PM pole to the next pole, the rate of change in airgap flux density at the magnet edges contributes to cogging torque. Hence, the lower the rate of change in flux density the lower the cogging torque. A commonly used method to reduce cogging torque in PMSM is skewing either stepwise or continuous as shown in Fig. 1.11. But it reduces the useful flux linkage of the magnet to the stator windings. Also, it increases the manufacturing complexity due to the number of skewing stacks and exhibits an unbalanced axial electromagnetic force which leads to vibration and noise.

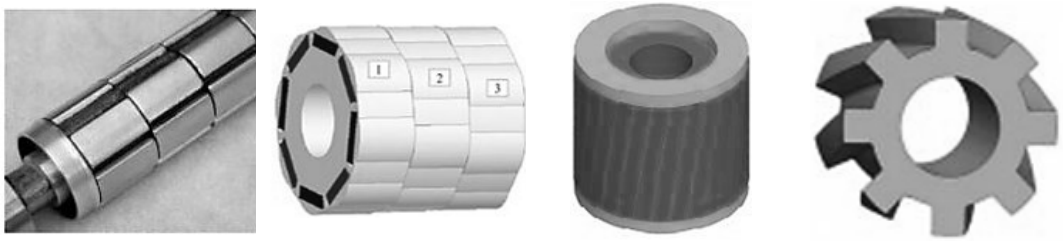

(a) (b) (c) (d)

Fig. 1.11: (a) Stepwise skew of the rotor for a surface PM machine. (b) The stepwise skew of the rotor for an interior PM machine. (c) Skewed squirrel cage rotor of an induction machine. (d) The skewed rotor of a synchronous reluctance machine [15].

PMs shaped in the radial direction such as the bread-load type design result in a non-uniform air gap that eliminates some harmonics in the air gap flux linkage. But there is a chance of permanent demagnetization due to differences in magnet thickness. The torque density of machines also reduces as the effective air gap is increased. To achieve the desired PM shape, the

conventional approach is to divide magnets into several segments which reduces the manufacturing complexity as shown in Fig. 1.12. The number of shaped magnet segments is decided based on the trade-off between the performance and the fabrication cost of the PMs. Unfortunately, the low versatility of the motor magnet fabrication technologies limits the development of new motor geometries. Also, the cost of these magnets in a PM electric motor can represent up to 50 % of the total motor cost as shown in Table 1.3 [16]. The high cost of the rare-earth materials necessary to fabricate PMs and the numerous required assembly steps are responsible for that high fraction.

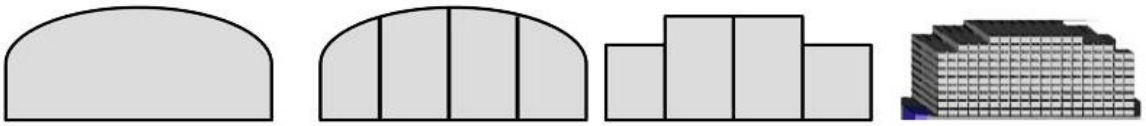

(a) (b) (c) (d)

Fig. 1.12: Segmented rotor magnet shaping technique of Bread-loaf magnet. (a) Bread-loaf shape without a segmented magnet. (b) Bread-loaf shape with segmented magnets. (c) Bread-loaf shape with rectangular shape segmented magnets. (d) Bread-loaf shape with multiple rectangular shape segmented magnets.

TABLE 1.3: FABRICATION COST DISTRIBUTION OF AN AUTOMOTIVE ELECTRIC MOTOR [16].

Motor part	***Cost fraction, %***
Bearings	1
Insulation	1
Shaft	2
Rotor iron	6
Stator iron	9
Stator copper	10
Housing	18
Magnets	53

Therefore, a new design concept to efficiently use the permanent magnet along with a manufacturing technique to reduce the torque pulsation without any risk of permanent demagnetization in the machine is required. Additive manufacturing offers potential new avenues to fabricate magnets allowing for unprecedented magnet shape flexibility without adding cost due to shape complexity. In the last few years, several authors have demonstrated that NdFeB permanent magnets can be produced using several novel additive manufacturing techniques such as big area additive manufacturing (BAAM) extrusion, fused filament fabrication (FFF), binder jetting, selective laser melting, and cold spray [16].

In big area additive manufacturing (BAAM) extrusion, using the melt extrusion process, the BAAM system deposits customized thermoplastic composites and high-performance engineered thermoplastics, that enable rapid manufacturing of parts completely unbounded in size. In the BAAM printing process, the nozzle deposits layers of the bonded magnetic materials which are fused and solidified to form the desired shape. Instead of requiring pre-extruded filament feedstock which is used in industry-standard extrusion-based systems, BAAM combines melting, compounding, and extruding functions to deposit polymer products at a controlled rate. It is observed that the printing of the extruded nylon magnet composite has a better flow than the widely explored 3D printing of plastic filament acrylonitrile butadiene styrene (ABS), and it also renders high accuracy. Therefore, the overall results obtained with the BAAM fabricated bonded magnets are much better than those of traditional injection molded magnets [16].

The binder jetting additive manufacturing process consists of a powder bed for the build area, an inkjet print-head, a roller, and either a powder hopper or feed bin that supplies powder. The process begins by dropping the build volume by the desired layer thickness and spreading a thin layer of powder over the build area with the roller. The print-head then passes over the build area and selectively deposits binder into the 2D cross-sectional shape of the current layer. The build volume drops again, more powder is spread, and the process continues until all layers of the part are completed. Here, isotropic NdFeB magnet powder particles (Magnequench MQP) are spread evenly over the feed and build sides of the print bed and printing can begin. The build side, where the binder is deposited, drops by one layer thickness, and the feed side, containing powder for subsequent layers, raises by the same distance. The print bed then moves under a heat lamp to set the bound powder and is subsequently covered in a new layer of powder by moving under the

roller. Upon printing completion, the entire build side of the print bed was removed and placed in an oven for the curing of the binder. Curing temperatures ranged from 100-150 °C for 4-6 hours, higher temperatures require less time to cure the binder. After cooling, the loose powder around the now cured and bound powder geometry can be brushed away revealing the bonded magnet. All unbound powder surrounding the printed geometry does not degrade during post-processing and can be used again for later prints [16].

In selective laser melting, laser powder bed fusion (LPBF) for the generation of metal parts is becoming an established processing technique for individualized products and small series displaying structural complexity and short time-to-market. However, it is at the moment limited to a few structural metals like steel, aluminum, and titanium alloys. The current development state of additive manufacturing of magnetic materials is limited to some proof of principle studies. Permanent magnets are used in electrical engines to provide a magnetic flux without the application of an electric current. Furthermore, permanent magnets require sufficient resistance against demagnetization in a reversed magnetic field. The basic properties of permanent magnets are remanent polarization, which corresponds to the magnetic field created by the magnet, and coercivity, which denotes the magnetic field that is needed to demagnetize a magnet. Remanence and coercivity both determine the maximum energy product $(BH)_{max}$, which acts as a figure of merit for permanent magnets. Since the development of NdFeB in 1984, it became the most advanced permanent magnet material and is nowadays used for recording devices, holdings, electrical motors, or wind turbines. NdFeB permanent magnets receive their superior magnetic performance from the hard magnetic $Nd_2Fe_{14}B_1$ intermetallic phase as well as careful chemical and microstructural design. Conventionally, magnet production is realized by powder metallurgical route consisting of powder fabrication, pressing and magnetic field alignment, sintering, and post-sintering heat treatment. With this technique, design freedom is limited to cylinders, cubes or cuboids, rings, and ring segments, and $(BH)_{max}$ can reach up to 474 kJ/m^3. If a higher degree of geometrical flexibility is necessary, bonded magnets can be used [16].

Among these new techniques, cold spray additive manufacturing offers the possibility of a very fast consolidation rate (> 1 kg/hour) which is a clear advantage for potential mass production applications. The cold spray operation principle is based on the acceleration of powder particles (typically 5-50 μm) to high velocity (> 600 m/s) using compressed N_2 gas and a de Laval nozzle

configuration. Accelerated particles impact the substrate with high kinetic energy producing particle and substrate deformation allowing for direct deposition on parts without the need for assembly. The resulting material is typically close to 100 % dense and possesses excellent adhesion and high mechanical properties. While the cold spray process uses relatively high gas temperatures (usually between 300-1000 °C), it is a solid-state process and both particle and substrate composition can be maintained with little to no oxidation. In previous studies, cold spray parameters were optimized for the production of NdFeB-Al composites, and a methodology for the fabrication of rotors with complex-shaped PMs was demonstrated. Cold sprayed NdFeB permanent magnets were processed using an aluminium binder and isotropic NdFeB powder resulting in very high ultimate tensile (>200 MPa) but limited magnetic remanence (0.5 Tesla). In the current work, the fabrication methodology that was developed for the realization of complex-shaped PM was adapted to the fabrication of the proposed skewed and petal shape rotors. The high mechanical strength of the cold-spray magnets can allow electrical machine rotors to operate at higher speeds, thus leading to elevated power densities. In addition, the flexibility given by the cold-spray process can allow the fabrication of an interior PM rotor with alternate layers of permanent magnets and soft magnetic materials with no need for the bridges and center-posts that tend to limit the performance of conventional laminated interior PM rotors [16].

The first step towards the high magnetic performance of magnets built by cold spray is to find the parameters leading to the maximal magnetic loading of the composite. Indeed, high magnetic content is needed to obtain a material with good magnetic properties. At the National Research Council of Canada (NRC Canada), magnetic remanence and intrinsic coercivity were obtained using a hysteresis graph Permagraph L equipment from Magnet Physik (Fishers, Indiana, USA). Measured magnetic quantities are shown on a typical hard magnetic material complete BH curve in Fig. 1.15 [16]. A good PM should possess both a high remanence (strongly related to the strength of the magnet) and a high coercivity absolute value (resistance to demagnetization of the magnet under a magnetic field). Two powder pre-mixes by NRC Canada were cold spray processed using a gas temperature of 600 °C. Figure 1.16 shows the measured magnetic properties obtained from these compositions. Measurement of the samples yielded a negligible change in coercivity (3 %) for the two compositions, while the remanence is 70 % higher for the 90 % pre-mix (90 % = 0.45 T, 75 % = 0.26 T). Volume fraction analysis showed that the magnetic fraction

is also 70 % higher for the 90 % mix and is thus directly responsible for the magnetic properties improvement.

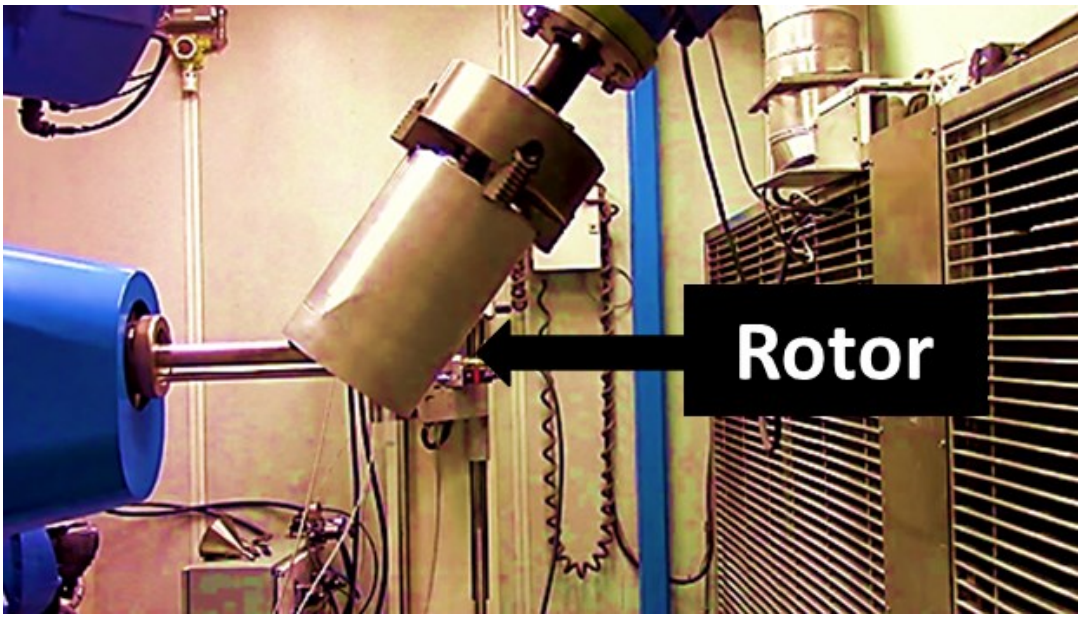

Fig. 1.13: Additive manufacturing process of a permanent magnet at National Research Council (NRC), Canada

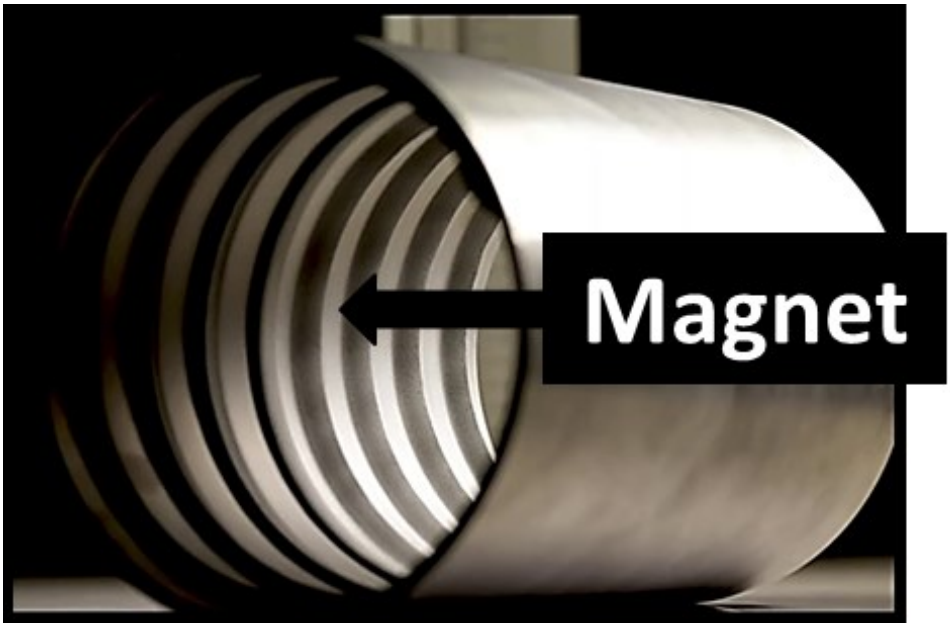

Fig. 1.14: Cold spray of a PM material inside the surface of a cylinder at National Research Council (NRC), Canada

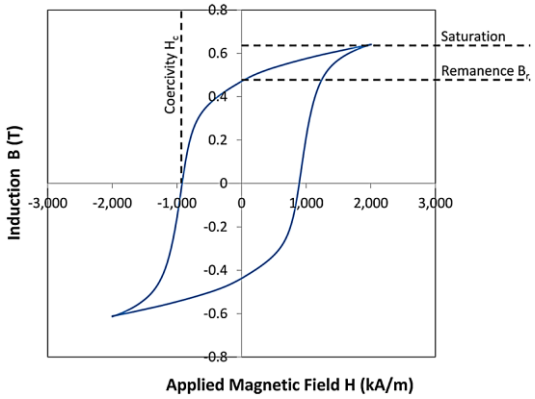

Fig. 1.15: Typical hysteresis curve obtained during the magnetic measurements (The remanence (Br) is the y-axis cross-over point while the intrinsic coercivity (Hci) is the x-axis cross-over point) [16].

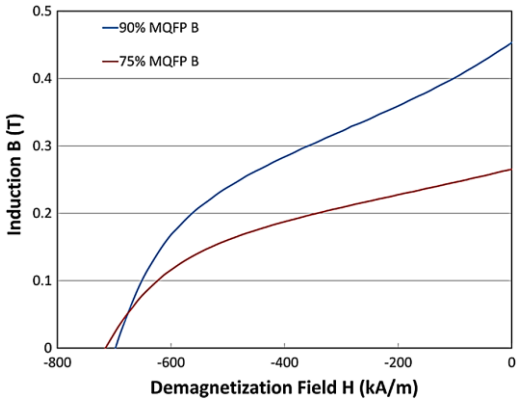

Fig. 1.16: Hysteresis curve of coatings produced using two different powder mix ratios: Blue – 90 % MQFP-B, 10 % H15, Red – 75 % MQFP-B, 25 % H15 [16].

Fig. 1.17 presents the maximum remanence value obtained for different fabrication techniques compared to the industry standard sintered magnets. At this point, sintered magnets offer the best remanence with values reaching up to 1.4 T. This is mainly due to the use of aligned anisotropic powder and volume fraction density of 95 + % obtained by pressing and sintering. Other techniques such as bonded magnets and additive manufacturing require the use of a binder material. This limits the maximum magnetic material volume fraction. While the obtained magnetic properties are interesting, there is still improvement needed to reach the industry's best values. Ultimate tensile strength (UTS) values for permanent magnets fabricated by different techniques are presented in Fig. 1.18.

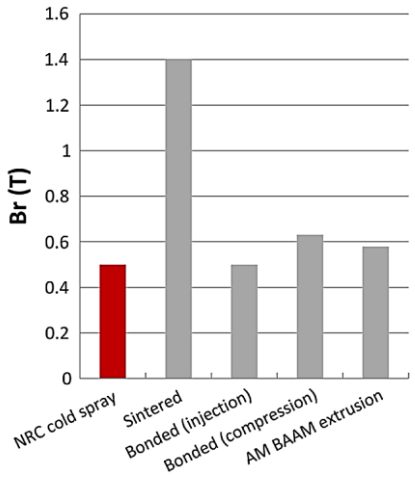

Fig. 1.17: Comparison of the remanence obtained for NdFeB fabricated by different manufacturing processes [16].

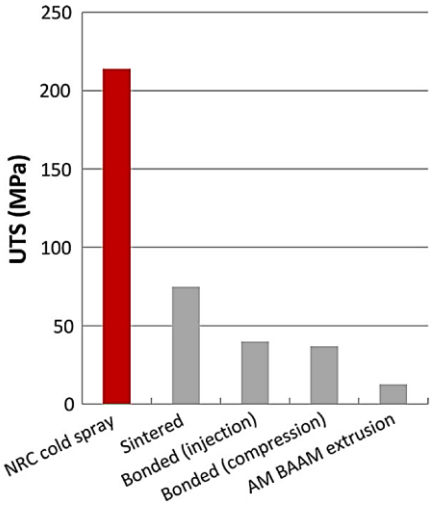

Fig. 1.18: Comparison of the ultimate tensile strength obtained for NdFeB fabricated by different manufacturing processes [16].

Cold spray-fabricated magnets exhibit the best performance with UTS above 200 MPa. This value can be attributed to the use of a metallic binder and the excellent inter-particle cohesion obtained via the high particle deformation in the cold spray process. As their adhesion and cohesion are higher than that of commercial glues, cold spray-fabricated magnets are a strong candidate to be used in applications where high mechanical integrity is required. The above-discussed analysis shows the potential of cold spray additive manufacturing of PMs for the realization of complex electric motor parts.

1.4. Soft Magnetic Composites (SMC) Materials

With the rapid research and development in the field of material science, the overall performance of electric machines has improved tremendously in the past years. For instance, the usage of rare-earth-based permanent magnets with high energy density has improved the efficiency and power density of the machines. The stator and rotor cores are made up of non-grain-oriented electrical steel (NES), which is an alloy with 0 – 3 % of silicon as an additive.

For the radial flux machine, the stator and rotor cores are made up of using electrical lamination steel sheets with insulation coating. These are stacked and punched together to reduce the excessive eddy current due to the magnetic flux flowing through it. The mechanical properties, permeability, and saturation flux density of the different electrical lamination steel sheets are very well-investigated by various researchers. However, the eddy current loss increases significantly with the supply frequency, which is one of the constraints for the maximum speed attainable by the machines. By using the thinner thickness of electrical steel sheets, the eddy current losses can be reduced significantly but it also leads to a much higher cost. Moreover, the magnetic flux can flow through laminated steel sheets in two-dimensional directions only within a plane due to insulation among the sheets. That's the reason why the manufacturing technique of the electrical machine has remained the same for the past decades. Alternative to laminated steel, powder metallurgy is a rapidly evolving technology to produce a wide variety of machine parts with complex shapes. These parts are created by compacting the mixture in a die and then heated or cured in a controlled temperature furnace to bond the particles.

In recent decades, trends in electric vehicle industries have increased the demand for new and better magnetic materials hence the SMC was born. The SMC consists of a fine iron powder

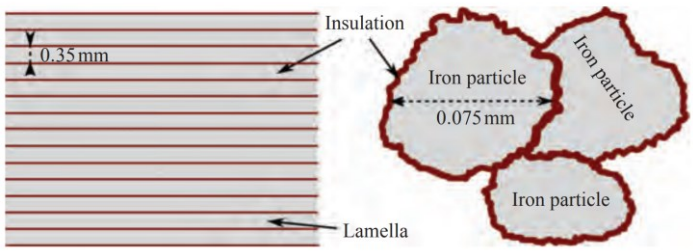

Fig. 1.19: Schematic structure of NES and SMC [17]

coated with an insulating layer as shown in Fig. 1.19 [17]. Due to the magnetic isotropy and inherent shape-making capabilities of powder metallurgy to make novel shapes can be realized, which are very difficult or even impossible to manufacture using traditional laminated sheets. The SMC also offers the potential for lower core losses and reduces the overall cost of the components.

The 'soft' term in SMC refers to the material's magnetic properties and it has nothing to do with its physical hardness. A soft magnet gets easily magnetized and demagnetized whereas a hard or permanent magnet always maintains its magnetization level. Hence the soft magnetic material will be able to switch magnetic fields easily and give the ability to rotate the rotating part of the machine. Therefore using SMC, a novel motor with an optimized shape for enhanced electromagnetic performance can be designed. The overall electrical resistance of SMC material is much higher than that of laminated steel because of the thin layer of insulation around each iron particle. Hence, the eddy current losses can be effectively reduced as it is the most dominant component in iron losses at a high operating frequency. The typically applicable regions of SMC, ferrite, and laminated electrical steel in terms of saturation flux density and frequency are illustrated in Fig. 1.20. The fabrication technique of SMC-based parts usually consists of only compaction and heat treatment processes. This process is simple and cost-effective when produced in large volumes in comparison with that of laminated electrical steel core [17]. Motor parts manufactured using SMC can achieve high surface quality with tight tolerance. For example, some of the parts fabricated using soft magnetic composite are as shown in Fig. 1.21.

In addition, the raw material wastages during the production and fabrication process of motor parts with SMC are very limited. The SMC-based motor parts also have a very high recycling ability for raw materials. The copper conductors and other materials can easily be separated from the SMC-based cores therefore, a high material utilization can be achieved as shown in Fig. 1.22. By summarizing all the advantages of SMC materials, it can be inferred that the motor parts can be manufactured with complex shapes and 3D magnetic flux conductivity through their cores. Hence, it provides great opportunities for motor designers and researchers to design novel motors with innovative shapes and magnetic circuits.

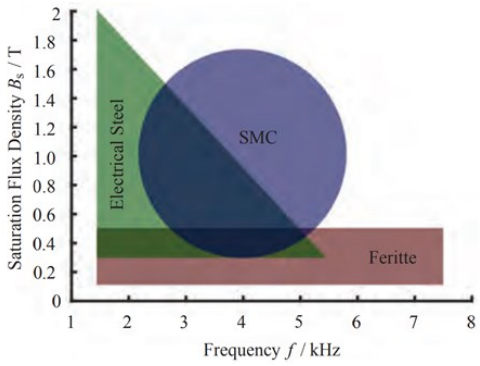

Fig. 1.20: Application regions of SMC, electrical steel, and ferrite [17 – 18]

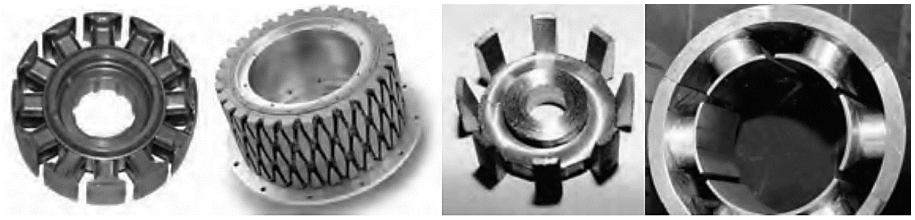

Fig. 1.21: Example of motor parts fabricated using soft magnetic composite (SMC) [17]

It is very important to discuss some of the obvious disadvantages of the SMC materials which are preventing their widespread usage. The magnetic permeability of SMC material is low compared to laminated steel and its hysteresis losses are high. In the magnetic analysis, the relative permeability of the insulation layer around the iron powder is close to air. Due to this, the saturation flux density and unsaturated magnetic permeability are low. Hence, it is not suitable for the electric motor design where a high magnetizing current is required such as a reluctance machine. The mechanical properties such as peak stress handling capability are low. The geometrical part size of the compacted SMC material is also limited. These disadvantages must be taken into consideration while designing electric motors with SMC.

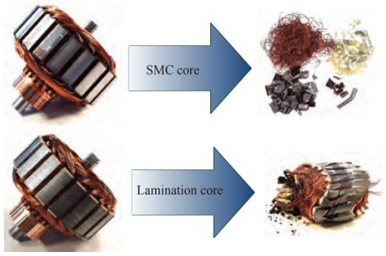

Fig. 1.22: SMC vs. laminated steel core recycling capability [17]

1.5. Organization and Outline of the Dissertation

This dissertation is divided into six chapters. It is organized as follows:

Chapter 1 presents the introduction of the permanent magnet electric machine for electric vehicles. It introduces an overview of the magnetic material and surface-mounted PM machines. It presents the introduction of rotor PM shaping and cold spray additive manufacturing. The basics of soft magnetic composite material and its properties are also presented.

Chapter 2 presents the analytical analysis and design of the surface mount petal-shaped permanent magnet rotor topology to leverage the additively manufactured technology developed by NRC, Boucherville. The in-situ post-assembly magnetization finite element-based current analysis is discussed. The electromagnetic results from the finite element-based of conventional rectangular-shaped skewed and unskewed permanent magnet rotor (Model A and Model B) and petal-shaped permanent magnet rotor (Model C) are analyzed and compared in this chapter. The machine characteristics such as back-EMF, cogging torque, and electromagnetic load torque are analyzed using an analytical approach and the 3D Finite Element Analysis (FEA) method.

Chapter 3 presents the hardware setup of the impulse magnetizer, constraints, magnetization issues, and test results of the cold spray permanent magnet rotor. It also presents the experimental electromagnetic analysis such as back EMF, rated torque, and cogging torque of all the three cold spray permanent magnet models.

Chapter 4 presents the design of a 15 kW surface PMSM using soft magnetic composite (SMC) material. It presents the properties of the different soft magnetic composite materials and their impact on the losses and efficiency of surface-mounted permanent magnet electric motors. It also discusses the criteria for the 7.12 kW surface PMSM design parameters such as magnet flux linkage, the d-q axis inductances, and characteristics currents to achieve a constant power speed range during flux weakening operation.

Chapter 5 presents the design of a 7.12 kW high torque density surface PMSM for a Renault Twizy car. It discusses the performance improvement of an electric motor using advanced soft magnetic composite (SMC) materials in the stator core and compared it with the laminated

steel-based designs for electric vehicle application using 3D finite element software. It also discusses the ring-type Halbach-array rotor for high-speed PMSM design.

Chapter 6 presents the conclusion of the completed research work and provides recommendations for possible future research works.

1.6. Original Contributions in this Dissertation

The research contributions achieved in this Ph.D. work can be summarized as follows:

Chapter 1, detailed literature on the permanent magnet electric machine for the electric vehicle application and its design benefits using cold spray additive manufactured permanent magnet and soft magnetic composite materials for the motor cores.

The contribution in chapters 2 and 3 is an optimization of the shape of the rotor permanent magnet for reducing torque pulsations and harmonic content in the back EMF. Unfortunately, the low versatility of the magnet fabrication technologies limits the development of new motor geometries. Cold spray additive manufacturing can be used for shaping permanent magnets for the direct fabrication of electric motor parts without the need for additional assembly steps. This fabrication technique allows an increase in the design flexibility of electrical machine geometries targeting improved performance. The design for the radial flux inner rotor surface permanent magnet synchronous machines (SPMSM) is presented. The magnet is shaped according to a petal shape along the axial direction while its thickness of it is kept uniform in the radial direction. A software-based finite element simulation is done to obtain the level of the magnetization current magnitude required to magnetize the shaped rotor. The design and test results of an impulse magnetizer and the in-situ post-assembly magnetization of a permanent magnet rotor manufactured by a cold spray additive manufacturing (AM) technique using the prototyped magnetizer are presented in this chapter. The performance of the prototyped machine with a conventional rectangular-shaped rotor PM design with an unskewed and skewed rotor (Model A and B) is compared with sinusoidal-petal-shaped rotor PM (Model C). The effects of rotor PM shape on back EMF, load torque, and cogging torque are analyzed experimentally.

***S. Singh**, et.al., "Cold Spray Additive Manufacturing of a Petal Shaped Surface PM Traction Motor," in-review at IEEE Transactions on Transportation Electrification.*

S. Singh *and P. Pillay, "Sinusoidal Shaped Surface Permanent Magnet Motor Using Cold Spray Additive Manufacturing," 2020 IEEE Energy Conversion Congress and Exposition (ECCE), 2020, pp. 2089-2094.*

M. Boby, ***S. Singh****, J. -M. Lamarre, M. Ibrahim, F. Bernier, and P. Pillay, "In-Situ Magnetization of a Cold Sprayed Permanent Magnet Rotor Using an Impulse Magnetizer," IECON 2021 – 47th Annual Conference of the IEEE Industrial Electronics Society, 2021, pp. 1-6.*

The contribution of chapter 4 is to analyze the impact of Soft Magnetic Composite (SMC) material properties on the losses and efficiency of electrical machines and presents a method for SMC grade selection. The surface radial flux electric motor is simulated using 3D finite element analysis (FEA). The results show that an SMC material with balanced properties achieved the highest efficiency and best overall performance. Also, the machine design parameters such as magnet flux linkage, the d-q axis inductances, and the characteristic current of the motor were tuned to achieve a constant power speed range during flux weakening operation.

M. Ibrahim, ***S. Singh****, et al., "Selection of Soft Magnetic Composite Material for Electrical Machines using 3D FEA Simulations," 2021 IEEE Energy Conversion Congress and Exposition (ECCE), 2021, pp. 3860-3865*

T. Payarou, ***S. Singh****, M. Muthusamy and P. Pillay, "Design Criteria for EV Drivetrain," IECON 2021 – 47th Annual Conference of the IEEE Industrial Electronics Society, 2021, pp. 1-6.*

The contribution in chapter 5 is the usage of soft magnetic composites (SMC) materials in the machine core parts to build a complex 3D structure and to reduce the manufacturing cost. This chapter presents the electromagnetic performance comparison analysis of a 7.12 kW radial flux PMSM with laminated steel and SMC stator core. Two different designs of 24/20 slot-pole and 12/8 slot-pole configurations using conventional surface permanent magnet rotor designs are simulated using a 3D FEA software package. The comparison is mainly focused on the torque density, copper loss, core loss, and active weight of the machine. In addition, the ring-type Halbach-array permanent magnet rotor for the 12/8 slot-pole is analyzed and optimized with the SMC stator core for high-speed electric vehicle application. The THD in phase back EMF and torque ripple is reduced by modifying the SMC stator tooth shape. Also, a scaled-down laboratory

design of ring-type Halbach-array PM rotor with 12/10 slot-pole is simulated using FEA with different lamination thickness of rotor core.

S. Singh *and P. Pillay, "High Torque Density Traction Motor Using Soft Magnetic Composites Material with Surface Ring-type Halbach-array PM Rotor Topology," IECON 2021 – 47th Annual Conference of the IEEE Industrial Electronics Society, 2021, pp. 1-6.*

Chapter 6 has the conclusions and the possible future work of the dissertation.

CHAPTER – 2

PETAL-SHAPED SURFACE PERMANENT MAGNET TRACTION MOTOR

This chapter presents the analytical analysis and design of the surface mount petal-shaped permanent magnet rotor topology to leverage the additively manufacturing technique. The in-situ post-assembly magnetization finite element-based current analysis and constraints are discussed. The electromagnetic results from the finite element-based of conventional rectangular-shaped unskewed and skewed permanent magnet rotor (Model A and Model B) and petal-shaped permanent magnet rotor (Model C) are analyzed and compared in this chapter.

2.1. Introduction

Electric vehicles (EVs) are emerging as a more efficient and environmentally friendly product for the automotive industry intending to reduce fossil fuel consumption and emissions of harmful gases. The conventional gasoline-based engine powertrains are been modified or replaced with electric powertrains. The production volume of motor vehicles has increased tremendously in the automotive industry since the 1950s. In recent years, the sales and production of electric vehicles have also increased due to an increase in geopolitical awareness, notable incentives from the government, lower running costs, etc. Therefore, research in the field of electric machine design to achieve high performance and efficiency is an interesting topic for the benefit of the automotive industry. It is predicted that looking at the present electric car revolution, by 2025, electric vehicles (EVs) will have costs similar to gasoline-based cars. By 2038, EV sales shall overtake internal combustion engines (ICE) cars [19-21].

Permanent magnet synchronous machines (PMSMs) are a good choice for electric vehicles due to their high efficiency and high power and torque density. It can be designed to operate for a wide torque-speed range with high power density. Induction machines are the most researched and well-established technology as they have been manufactured for many decades. It also offers low

production costs, no magnets usage, and is easy to control drive hence, it is very robust. But as the rotor conductors generate high conduction losses, heat is produced by both the stator and rotor. Due to this, the operating efficiency of induction machines is lower when compared to the PMSMs. Another popular topology is the switched reluctance motor (SRM), which does not depend on the permanent magnet and is exceptionally robust. However, there have been some major challenges such as low power factor, high vibration, and high acoustic noise, and the inverter needs to be customized to operate its independent phase windings [22-27]. Therefore, permanent magnet (PM) based electric machines are one of the most prominent choices for traction machines. However, PMSMs can be susceptible to cogging torque which produces torque pulsations and leads to vibration and acoustic noise in the electric motor [28]. Torque ripple and cogging torque are two components of torque pulsation in electric machines. Cogging torque occurs due to the interaction between the slotted structure of the stator core and the rotor PMs. Various techniques have been proposed for minimizing torque pulsations in the literature. It is typically done either by machine control strategies in which harmonic current components are injected into windings or by different machine design geometries such as skewing, different slot openings, and permanent magnet (PM) shaping and shifting [22,29,30]. One effective way to reduce torque pulsations is the modification and optimization of PM geometry as PM shape and its leakage flux have a significant effect on cogging torque. Indeed, as the rotor rotates and moves from one PM pole to the next pole, the rate of change in airgap flux density at the magnet edges contributes to cogging torque. Hence, the lower the rate of change in their flux density the lower the cogging torque. A commonly used method to reduce cogging torque in PMSMs is either stepwise or continuous skewing. However, this method reduces the useful flux linkage of the magnet to the stator windings, increases the manufacturing complexity due to the number of skewing stacks, and exhibits an unbalanced axial electromagnetic force which can lead to vibration and noise [23].

PMs shaped in the radial direction such as the bread-load type design result in a non-uniform air gap that eliminates some harmonics in the air gap flux linkage. Permanent demagnetization can occur due to differences in magnet thickness. This can also lead to lower torque density as the effective air gap is increased. To achieve the desired PM shape, the conventional approach is to divide magnets into several segments. These magnet segments require numerous assembly steps which contribute to the cost increase relative to such design. The number of shaped magnet segments is decided based on the trade-off between the performance and the

fabrication complexity and cost of the PMs. It follows that the economical aspects of traditional manufacturing strategies are restricting the flexibility in PM design geometries [31-39]. Shah et al. [22] presented the permanent magnet pole shaping of the surface PM motor but could not fully eliminate the cogging torque due to the stacking structure of commercial permanent magnets. Zhao et al. [23] also proposed permanent magnet shaping to minimize torque pulsations but the prototyped motor used stepwise stacking of the bar-type magnets approximating a sinusoidal shape. Du et al. [24] introduced shaped-magnet designs and analyzed them using finite element software such as Infolytica and JMAG, but hardware validation of the designs was not presented in the paper. Although the above-mentioned researchers presented the magnet shaping concept to improve the performance of the machine however the permanent magnet rotor poles were segmented and not shaped continuously. Additive manufacturing offers potential new avenues that can create new ways that magnets are fabricated allowing for unprecedented magnet shape flexibility without adding cost due to shape complexity. Among these new techniques, cold spray additive manufacturing offers the advantages of fast consolidation rate (> 1 kg/hour) and direct assembly and can readily be applied to the fabrication of prototype rotors with complex-shaped PM. [32].

A rotor design concept for a surface PMSM that utilizes magnetic materials effectively with uniform magnet thickness in the radial direction to reduce its demagnetization risk is discussed, prototyped, and evaluated in this chapter. The rotor PM with a sinusoidal shape produces sinusoidal magnetic flux distributions in the air gap and hence sinusoidal back EMF. Therefore, PMs with sinusoidal shape and symmetrically in the axial direction reduce harmonics in the back EMF which decreases cogging torque and produces a smooth electromagnetic torque in the machine. Three different motor configurations were designed and simulated using JMAG 3-D finite-element analysis (FEA) software: a conventional rectangular-shaped rotor PM with unskewed PM (Model A) and with skewed PM (Model B) as well as a sinusoidal-petal shaped rotor PM (Model C). These three rotors were prototyped using cold-spray additive manufacturing and magnetized in-situ post-assembly using an impulse magnetizer. For low-cost design, a magnetizer setup consisting of a capacitor bank with a switch connected across the motor terminals which can supply a current pulse required for magnetization using the stator winding is prototyped.

2.2. *Analysis of the Petal-shaped Rotor Permanent Magnet*

The back EMF of the machine is given by the rate of change of the magnetic flux. The magnitude and shape of the back EMF waveform depend on the amount of magnetic flux linkage as well as its cross-sectional area. The permanent magnet shape used in this study is an axial sinusoidal-petal shaped for a radial flux surface-mounted machine. To better characterize this concept, the flux linkage is computed for one pole with a fully pitched coil and then Faraday's law is applied to calculate the back EMF.

A 4-pole surface PMSM as shown in Fig. 2.1 with two slots representing a winding with N turns of coils was considered. The pictorial representation of the conventional and sinusoidal-petal-shaped rotor permanent magnet is shown at the top of Fig. 2.2. When the rotor position is at 0° electrical ($\theta_e = 0$), the fully pitched coil is centered over the north pole of the rotor permanent magnet and flux flows towards the coils across the air gap as shown in Fig. 2.1(a). The direction of this flux flow is in the same direction as that produced by the current flowing in the coil. Therefore, the flux linkage (λ) is positive and given by $\lambda = N\phi_g$ where N is the number of turns of wire and ϕ_g is the air gap flux. Rotating the rotor by 90° electrical ($\theta_e = \pi/2$) as shown in Fig. 2.1(b), the coil is now centered over both the north and south poles of the rotor permanent magnet. At this position, the flux flows equally in magnitude towards and away from the rotor due to the different polarities of the magnet. Hence, the total flux linked by the coil is zero.

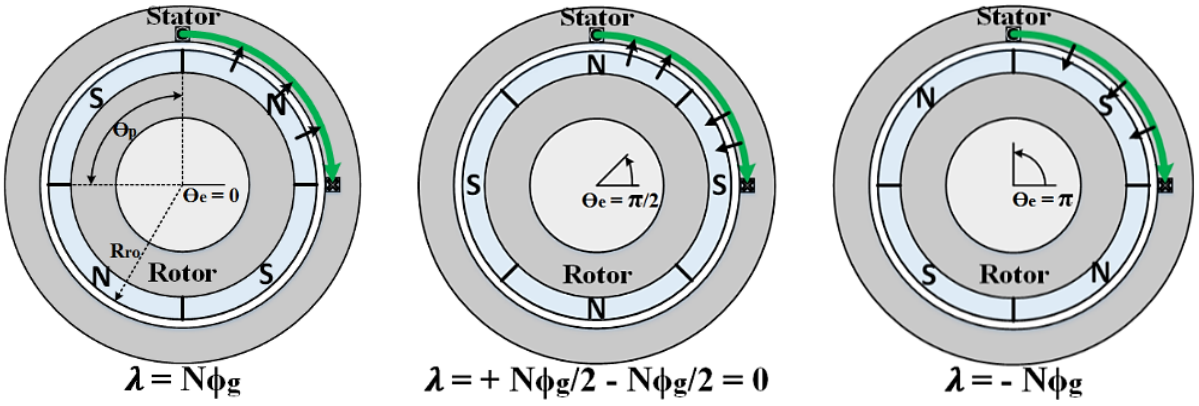

(a) (b) (c)

Fig. 2.1: Surface-mounted permanent magnet machine with full pitch coil at (a) at 0° elec. (b) at 90° elec. (c) at 180° elec.

Again, rotating the rotor by 90° electrical ($\theta_e = \pi$), the coil is centered over the south pole. The flux flows towards the rotor and is the same in magnitude as the flux linked at the initial position $\theta_e = 0,$ but in opposite direction, so the flux linkage is negative and given by $\lambda = -N\phi_g$. The flux linkage over one electrical cycle varies linearly and it will create a periodic flux linkage waveform as the magnet rotor poles alternately link the coil of the machine. The magnetic flux distribution in the air gap is constrained by the cross-sectional area of the rotor permanent magnet, conventional shaped magnet (Model A) produces rectangular whereas sinusoidal-petal shaped magnet (Model C) produces sinusoidal magnetic flux distributions through the air gap as shown in Fig. 2.2 (a) and (b) respectively. The air gap flux ϕ_g for the conventional shaped magnet design (Model A) can be expressed using equations (2.1) and (2.2),

$$\phi_g = B_g A_g \tag{2.1}$$

$$\phi_{g,Model\ A} = B_g R_{ro} \theta_p L_{stk} = \frac{2\pi}{N_m} B_g R_{ro} L_{stk} \tag{2.2}$$

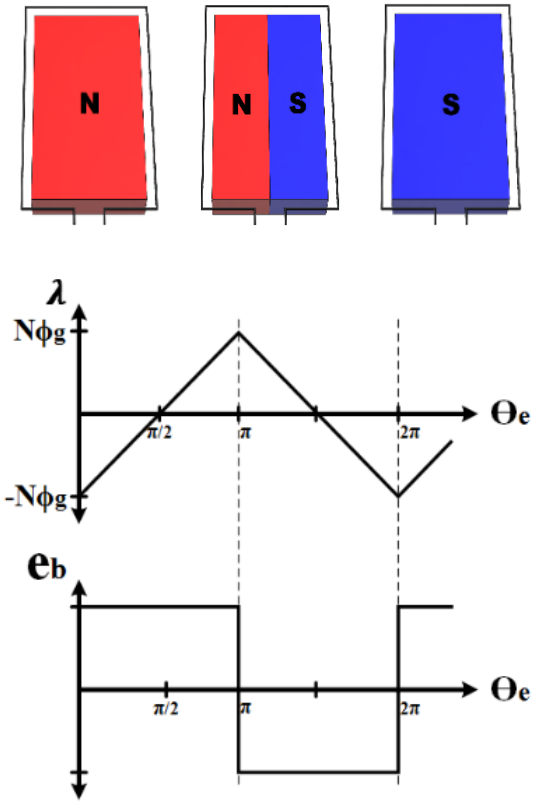

(a)

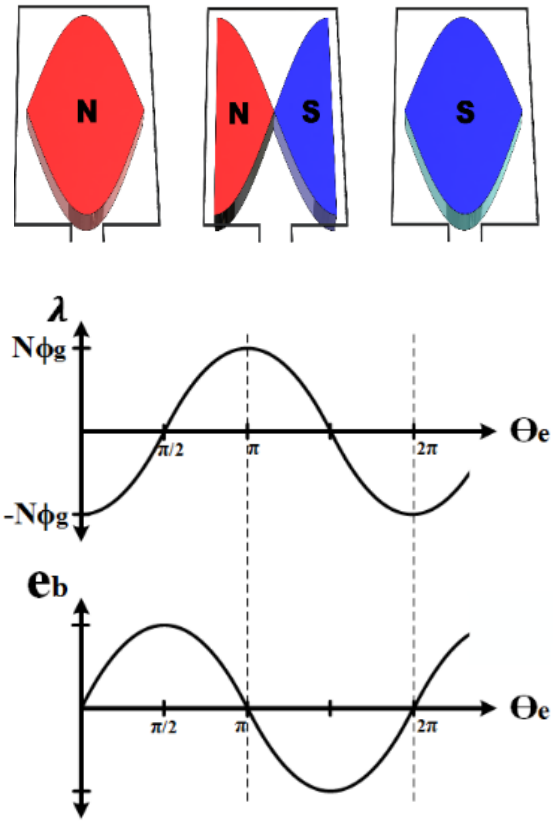

(b)

Fig. 2.2: Flux linkage and back EMF at different rotor positions. (a) Model A and (b) Model C

For Model C, the length of the rotor permanent magnet varies axially following a sinusoidal-petal shape and it is symmetrical over half the stack length as shown in Fig. 2.3. The air gap flux ϕ_g for the sinusoidal-petal-shaped magnet design Model C can be written as shown in equations (2.3) and (2.4).

$$\phi_{g,Model\,C} = B_g \times \left\{ \int_0^{2\pi R_{ro}/N_m} \left[\frac{L_{stk}}{2} \sin\left(\frac{\pi . x}{2\pi R_{ro}/N_m} \right) \right] dx \right\} \times 2 \tag{2.3}$$

$$\phi_{g,Model\,C} = \frac{4}{N_m} B_g R_{ro} L_{stk} \tag{2.4}$$

where B_g is the air gap flux density, A_g is the air gap cross-sectional area, R_{ro} is the air gap radius at the magnet surface, θ_p is the angular pole pitch in rad mech., L_{stk} is the stack length and where x varies from 0 to $2\pi R_{ro}/N_m$. The flux linkage for Model A and Model C varies over one electrical cycle and is triangular and sinusoidal in nature respectively as shown in Fig. 2.2. It can be written as $\lambda_{Model\,A} = (2N\phi_g/\pi)\theta_e$ and $\lambda_{Model\,C} = -N\phi_g \cos\theta_e$ where θ_e is the electrical rotor position angle.

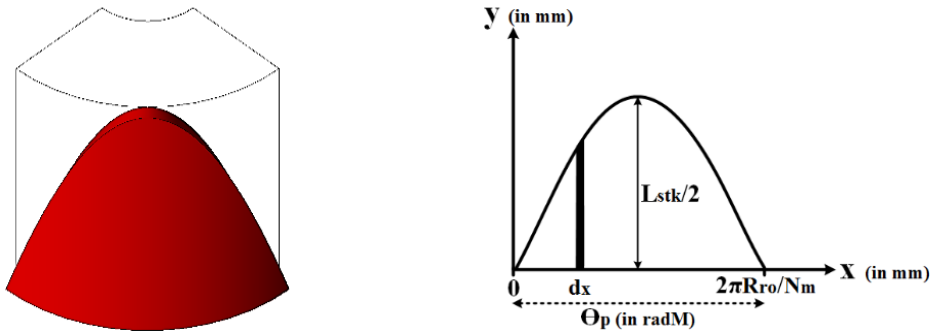

(a) (b)

Fig. 2.3: Rotor PM of Model C (a) sinusoidal-petal shaped PM geometry for half stack length (b) analytically representation of sinusoidal-petal shaped PM

Analytically, the induced back EMF and electromagnetic torque produced by the current flowing in the coil ($i\ A$) for both designs are expressed using equations (2.5) – (2.11).

$$e_b = \frac{d\lambda}{dt} = \frac{d\theta_e}{dt}\frac{d\lambda}{d\theta_e} = \omega_e \frac{d\lambda}{d\theta_e} = \frac{N_m}{2}\omega_m \frac{d\lambda}{d\theta_e} \tag{2.5}$$

$$e_{b,Model\,A} = \frac{N_m}{2}\omega_m \frac{2N\phi_g}{\pi} \tag{2.6}$$

$$\left|e_{b,Model\,A}\right| = E_{b,Model\,A} = \frac{N_m}{2}\omega_m \frac{2N}{\pi}\left(\frac{2\pi}{N_m} B_g R_{ro} L_{stk}\right) = 2NB_g R_{ro} L_{stk}\omega_m = K_{e,conv}\omega_m \tag{2.7}$$

$$|T_{Model\,A}| = \frac{E_b i}{\omega_m} = 2NB_g R_{ro} L_{stk} i = K_{t,conv} i \tag{2.8}$$

$$e_{b,Model\,C} = \frac{N_m}{2}\omega_m N\phi_g(\sin\theta_e) \tag{2.9}$$

$$\left|e_{b,Model\ C}\right| = E_{b,sine} = \frac{N_m}{2}\omega_m N\left(\frac{4}{N_m}B_g R_{ro} L_{stk}\right)\sin\theta_e$$
$$= 2NB_g R_{ro} L_{stk}\omega_m \sin\theta_e = K_{e,sine}\omega_m \tag{2.10}$$

$$|T_{Model\ C}| = \frac{E_b i}{\omega_m} = 2NB_g R_{ro} L_{stk}\sin(\theta_e)\, i = K_{t,sine} i \tag{2.11}$$

where $e_{b,Model\ A}$and $T_{Model\ A}$ are induced back EMF and electromagnetic torque expression for Model A, $e_{b,Model\ C}$ and $T_{Model\ C}$ are induced back EMF and electromagnetic torque expression for Model C, constant K_e is the back EMF constant in $V/(radM/s)$ and K_t is the torque constant in Nm/A.

2.3. In-situ Post-assembly Magnetization Current FEA-based Analysis

Domains or regions are formed by the groups of atoms in a ferromagnetic material and it exhibits a net magnetic moment. Prior to magnetization and in the absence of an external field, these individual domains are magnetized in a random direction which mutually cancels out each other. The magnet needs to be magnetized by applying an external magnetizing field with high enough magnitude to cause most of the domains to align in the direction of the applied field. The magnetic equivalent circuit (MEC) approach of the machine model can be used to analytically calculate the required magnetization current level. The magnetic flux (ϕ_m) is given by equation (2.12). Considering the magnetic circuit for each pole of the machine model, the magnetization current (I_{mag}) magnitude on the d-axis is calculated as given by equation (2.13). The magnetizing current (I_{mag}) produces a magnetic flux density (B_m) in the rotor PM. Due to the high permeability of the steel materials, stator core reluctance ($\Re_s$) and rotor core reluctance ($\Re_r$) are negligible. For simplicity leakage reluctance ($\Re_l$) can be ignored. $\Re_g$ and $\Re_m$ are the air-gap reluctance and the magnet reluctance respectively. While N is the number of current-carrying turns.

$$\phi_m = B_m A_m \tag{2.12}$$

$$\phi_m(\Re_r + 2\Re_m + 2\Re_g + \Re_s) = NI_{mag} \tag{2.13}$$

The FEM-based approach can be used to calculate the magnitude of the magnetization current at which the rotor PM is saturated. With the help of a magnetic field analysis simulation, rapid performance evaluation during the initial design stage is possible. A two-dimensional quarter cross-section view of the surface PMSM is considered for the analysis. As the cold spray technology allows the building of the magnet directly on the rotor surface from raw NdFeB powder, the PM is initially at an unmagnetized state.

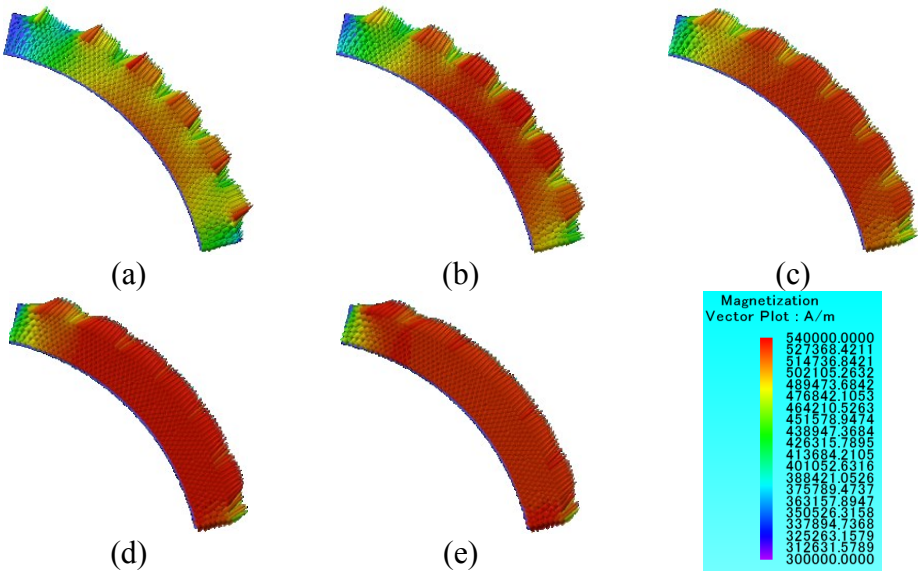

Fig. 2.4: Simulated magnetization levels in cold spray rotor PM at (a) 100 A (b) 500A (c) 1000 A (d) 1500 A and (e) 2000 A

To magnetize it, the rotor is placed inside the stator. After it is oriented with the stator windings, a current is supplied through the stator windings for a short duration to avoid heating the coils. This current-carrying coil generates the magnetization field in the rotor PMs. The magnitude of the current is varied from 100 A up to 2000 A, to ensure complete magnetization of the rotor PMs. To validate the magnetization level of the rotor permanent magnet, the back EMF of the machine at the base speed of 1800 rpm is observed at each step of the magnetization current. It is then compared with the reference back EMF obtained with the fully magnetized rotor permanent magnet in the simulation. The magnetization field in the rotor PMs at different magnetization levels is shown in Fig. 2.4 and its corresponding back-EMF waveform is shown in Fig. 2.5. At 1500 A, the magnetization level of the magnet and the back EMF generated at the base speed is very close to that of a fully magnetized magnet.

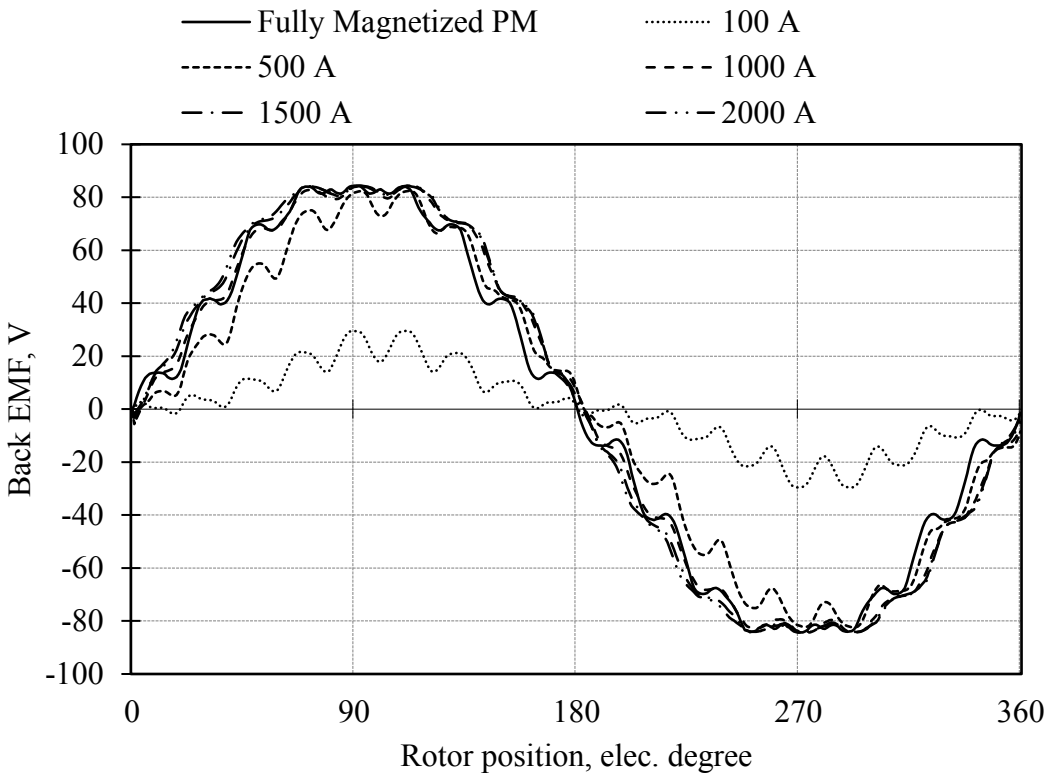

Fig. 2.5: Back EMF at base speed with different magnetization current magnitude

2.4. Three-dimensional FEM-based Performance Analysis

The rotor permanent magnet width in Model C varies throughout the axial direction, hence a 3-D FEM simulation using JMAG-Designer is necessary for the performance analysis and comparison [40]. To reduce the computational time of the software simulation, one-fourth of the radial model geometry was simulated without loss of generality. The number of elements for the one-fourth radial model obtained using JMAG-Designer is around 995823 whereas the number of nodes is 246562 with an average quality of 61.7 %. The geometrical dimension of the stator and rotor dimension is kept the same except for the shape of the rotor PMs for all three models. Fig. 2.6. shows the Model A rotor with unskewed PM, Model B skewed PM by one slot pitch (10°), and Model C rotor with sinusoidal-petal shaped PM.

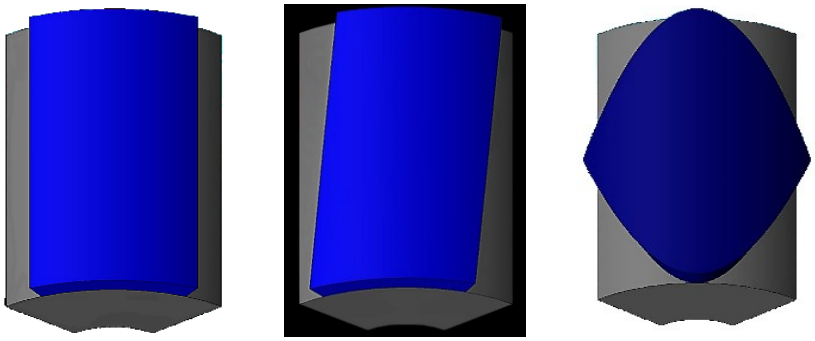

(a) (b) (c)

Fig. 2.6: Rotor geometry of (a) Model A with unskewed PM, (b) Motor B with skewed by 10° PM, and (c) Model C with sinusoidal-petal shaped PM

TABLE 2.1: DESIGN PARAMETER AND RATINGS OF THE SPMSM MODELS

Parameter	***Value***
Number of stator slots and poles	36 slots and 4 pole
Stator outer diameter	180 mm
Stator inner diameter	109 mm
Rotor outer diameter	108 mm
Rotor inner diameter	33.5 mm
Permanent magnet thickness	7.5 mm
Stack length	125 mm
Steel type	M36G29
Air gap length	0.5 mm
Rated line current (RMS)	20 A
Base speed	1800 rpm
Number of turns per coil	7
Number of layers	2
Wire size and diameter	SWG 21 and 0.813 mm

The radial thickness of all three shaped rotor PMs mounted on the surface are the same and magnetized radially. The volume of Model C with sinusoidal-petal-shaped rotor PM is reduced by 13.11 % compared to the Model A and Model rotor PMs. The design parameters are summarized in Table 2.1. As the number of coil turns is kept equal, the magnetic flux linkage will be less for Model C due to the shape of its rotor PM. The back EMF of both the models was calculated at no-load and at the rated speed of 1800 rpm. The back EMF waveforms for Model A, B, and Model C are shown in Fig. 2.7 and 2.8 respectively. Harmonic orders present in the phase back EMF are shown in Fig. 12 and summarized in Table 2.2. Model C shows sinusoidal back EMF with a fundamental peak magnitude of 77.87 V with a THD of 1.35 % whereas Model A and B consist of harmonics in the back EMF with a fundamental peak magnitude of 82.72 V for the unskewed rotor PM with a THD of 8.87 % and 82.14 V for skewed rotor PM with the THD of 5.27 %. The back EMF magnitude is higher for Model A than for Model C due to the higher magnetic flux linkage which can be adjusted in Model C if the number of coil turns is increased.

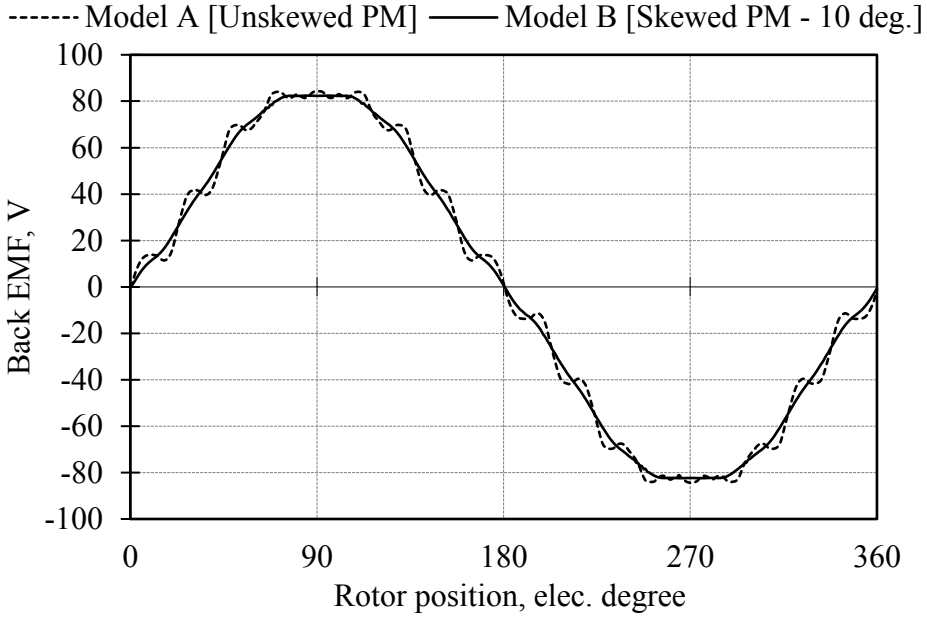

Fig. 2.7: Simulated phase back EMF of Model A with unskewed and Model B skewed PM

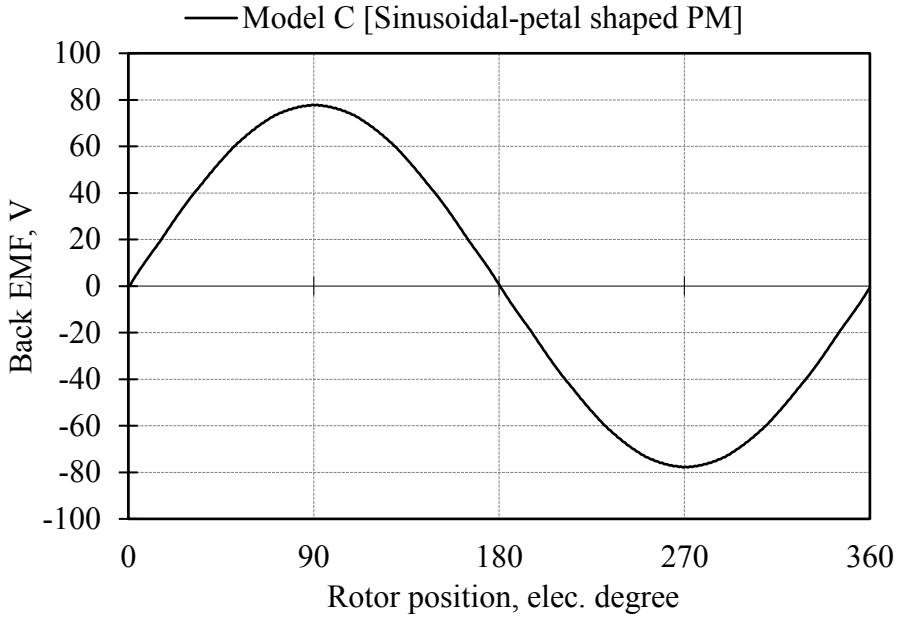

Fig. 2.8: Simulated phase back EMF of Model C with sinusoidal-petal shaped PM

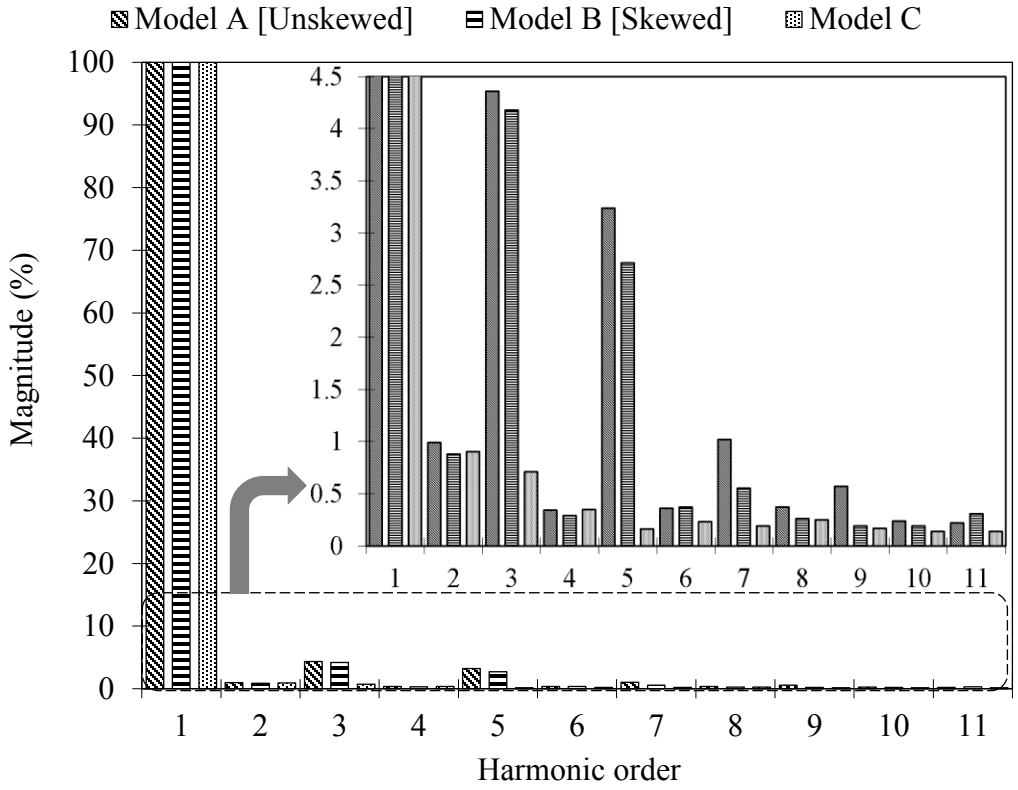

Fig. 2.9: FFT analysis of the phase back EMF for Model A, B, and C

TABLE 2.2: HARMONIC ORDER OF BACK EMF FOR MODEL A, B, AND C

Back EMF Harmonic Order	***Model A***	***Model B***	***Model C***
Fundamental (V)	82.72 V peak	82.14 V peak	77.87 V peak
3rd Harmonics (%)	4.36	4.18	0.71
5th Harmonics (%)	3.24	2.71	0.16
7th Harmonics (%)	1.02	0.55	0.19
9th Harmonics (%)	0.57	0.19	0.17
11th Harmonics (%)	0.22	0.06	0.14
THD (%)	8.87	5.27	1.35

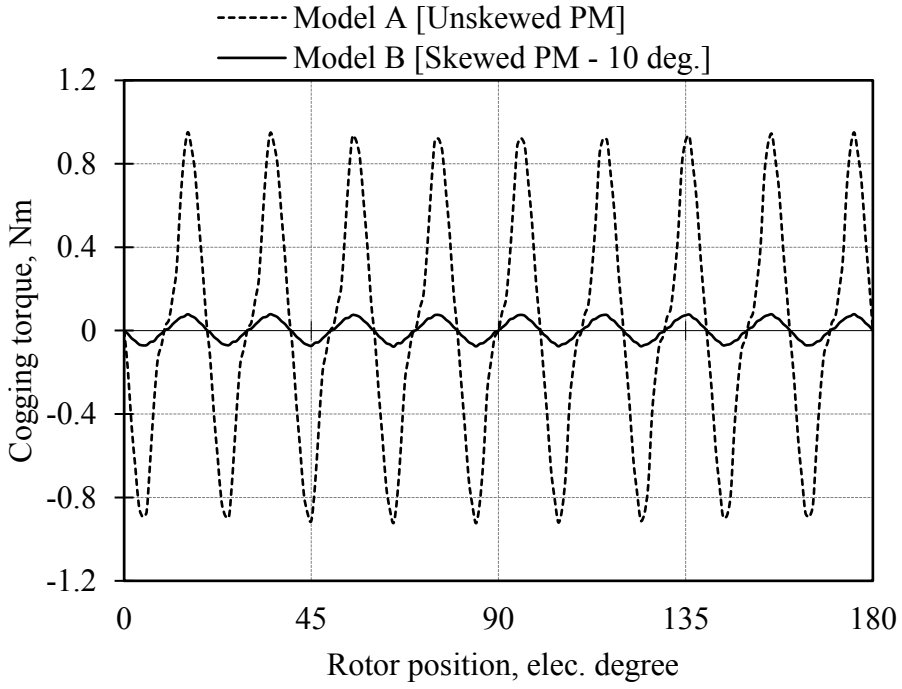

Fig. 2.10: Simulated cogging torque of Model A with unskewed and Model B skewed PM

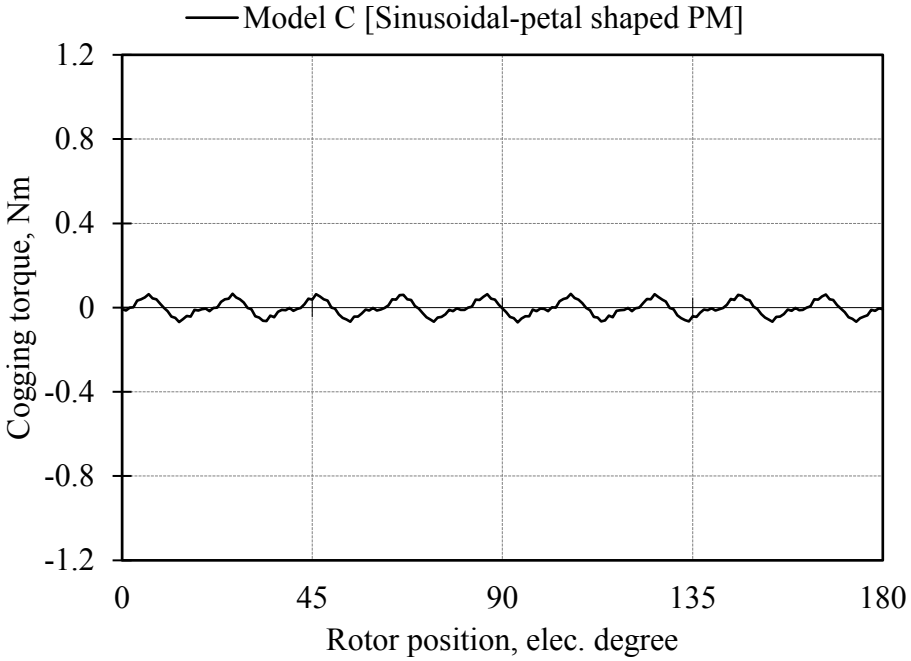

Fig. 2.11: Simulated cogging torque of Model C with sinusoidal-petal shaped PM

Fig. 2.10 shows the cogging torque of Model A and B for the unskewed and skewed rotor PM with no stator current excitation. Fig. 2.11 shows the cogging torque present in Model C. When the rotor rotates, the magnet edge passes over the slot opening resulting in a change in co-energy hence torque pulses are generated. The sum of these torque pulses produces cogging torque. The cogging torque for Model A with unskewed rotor PM is 1.9 Nm peak to peak and Model B with skewed rotor PM is 0.156 Nm peak to peak. Whereas for Model C, cogging torque is 0.13 Nm peak to peak. The electromagnetic load torque of Model A for unskewed and Model B for skewed rotor PM is shown in Fig. 2.13 at the rated load with sinusoidal current excitation. Fig. 2.14 shows the load torque of Model C. The average torque for Model A with unskewed rotor PM is 13.21 Nm and Model B with skewed rotor PM is 13.08 Nm. For Model C the average torque is 12.29 Nm. Model A with unskewed rotor PM shows a large torque pulsation of 23.08 % and Model B with skewed rotor PM shows a torque pulsation of 7.33 % due to the harmonics present in its magnetic loading.

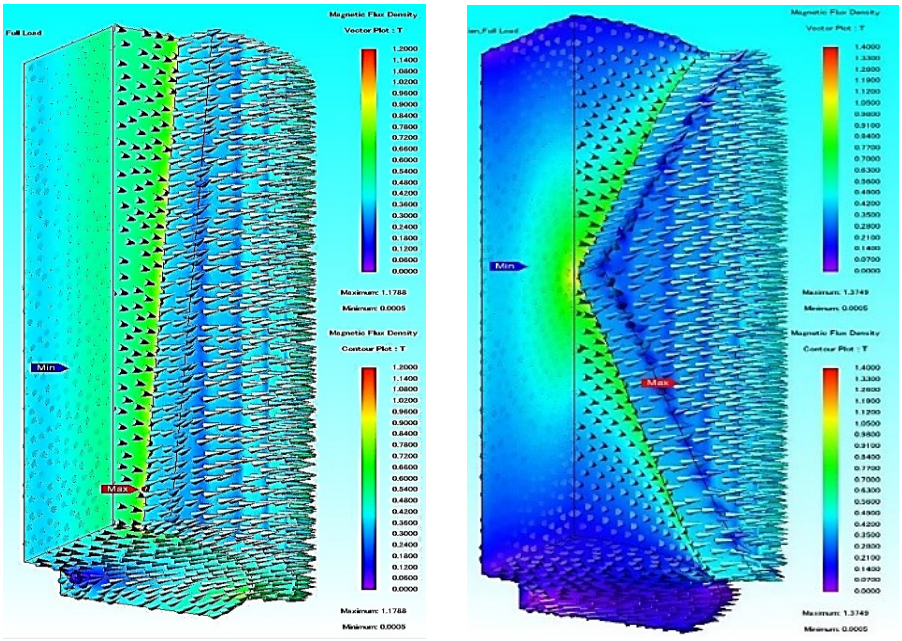

(a) (b)

Fig. 2.12: Magnetic flux lines for SPMSM (a) Model B with skewed PM and (b) Model C with sinusoidal-petal shaped PM

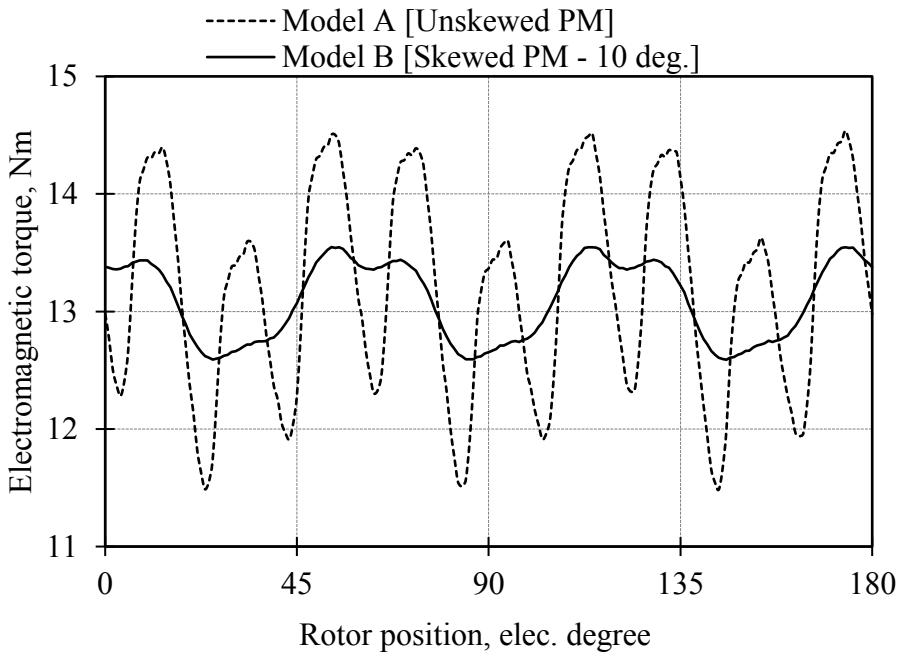

Fig. 2.13: Simulated electromagnetic torque of Model A with unskewed and Model B skewed PM

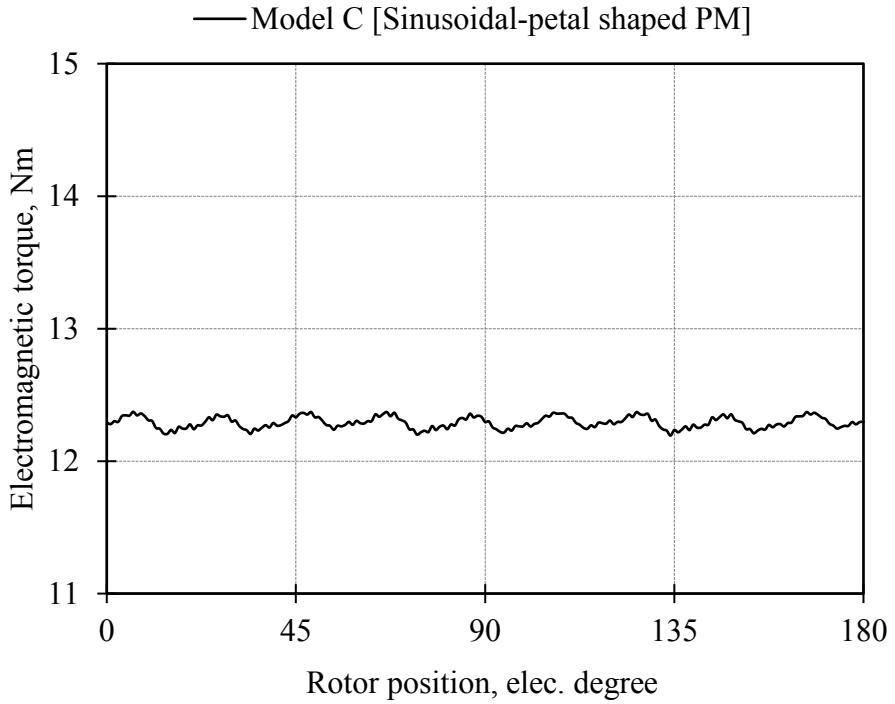

Fig. 2.14: Simulated electromagnetic torque of Model C with sinusoidal-petal shaped PM

Torque pulsation in Model C is reduced to 1.46 % compared to Model A and B. But the average torque of the Model C is reduced by 6.9 % due to the magnetic flux leakage at the edges of the sinusoidal-petal shaped rotor PM and lower magnet flux to couple with the stator windings. The magnetic flux line patterns for both models are shown in Fig. 2.12. The performance analysis is summarized in Table 2.3.

TABLE 2.3: PERFORMANCE COMPARISON OF MODEL A, B, AND C

Parameter	***Model A***	***Model B***	***Model C***
Magnet Volume (%)	100 %	100 %	86.89 %
Phase back-EMF THD	8.87 %	5.27 %	1.35 %
Cogging torque (pk-pk)	1.9 Nm	0.156 Nm	0.13 Nm
Average torque	13.21 Nm	13.08 Nm	12.29 Nm
Torque ripple	23.08 %	7.33 %	1.46 %

2.5. Conclusions

This chapter has presented a new cold-sprayed additively manufactured shaped rotor PM to reduce the torque pulsations and to improve the back EMF with lower harmonic content by using the magnetic material effectively. The surface PM pole is shaped in the sinusoidal-petal (Model C) in the axial direction and compared with the conventional rectangular shape with unskewed (Model A) and skewed (Model B) PMs. The machine characteristics such as back-EMF, cogging torque, and electromagnetic load torque are analyzed using an analytical approach and the three-dimensional Finite Element Analysis (FEA) method. Also, the magnetization current required to magnetize the rotor magnet is calculated. The THD in the measured phase back EMF for Model C is 3.07 % and the measured torque ripple is 9.31 % which is the least compared to Model A and B. However, as the number of coil turns is kept the same, the magnetic flux linkage for Model C was less due to the leakage in flux at the edges of the sinusoidal-petal-shaped rotor PM. Hence, the measured average electromagnetic torque of Model C is reduced by 17.2 % compared to Model A with unskewed rotor PM.

CHAPTER – 3

PROTOTYPING AND EXPERIMENTAL STUDY

This chapter presents the hardware setup of the impulse magnetizer, constraints, magnetization issues, and test results of the cold spray permanent magnet rotor. It also presents the experimental electromagnetic analysis such as back EMF, rated torque, and cogging torque of all the three cold spray permanent magnet models.

3.1. Introduction

Additive manufacturing techniques have been widely used due to their ability to rapidly prototype complex three-dimensional parts for electric motors [41]. Traditionally, high-performance permanent magnets (PM) are fabricated using powder compaction for sintered magnets or injection molding for bonded magnets. After its fabrication, PM is cut into the desired shape and size and then assembled in the rotor. These pre-magnetized magnets exhibit very strong attractive or repulsive force during the assembly process. Hence it requires extreme care to prevent the PM and rotor from damage as well as the people from injury [42-43]. The novel cold spray additive manufacturing (AM) technique can perform all these steps at once and could also lead to cost reduction. In the cold spray additive manufacturing process, the fine PM powder is accelerated using a high-velocity compressed jet. The magnetic parts are built layer by layer directly on the rotor surface with fewer limitations on size and shape than traditional manufacturing techniques. These advantages offered by cold spray technology could lead to enhanced motor performance [31], [32]. The cold spray additively manufactured rotor PMs are initially at a non-magnetized state. After the assembly of the complete rotor, an in-situ magnetization procedure by using the stator windings and stator core can be used to fully benefit from the more complex shaped magnets [34]. A magnetizer setup commonly referred to in literature [44-47] as an impulse magnetizer is used in this work because of its simplicity and low cost. In an impulse magnetizer, a capacitor bank is pre-charged to a pre-determined voltage and is then connected across the stator windings of the machine using a switch. An exponentially decaying current pulse flows through the stator. The exact shape and the peak value of the current depend on the initial voltage in the capacitor

bank, the value of the capacitance, the total inductance, and resistance in the circuit. There is abundant literature available on the operation and analysis of impulse magnetizers, but not many details are available from a design point of view. The impulse magnetizers can be easily constructed on an ad-hoc basis using components commonly available in a power electronics laboratory and hence are ideal for academic laboratories and workshops which do not have access to an expensive commercial magnetizer.

3.2. Impulse Magnetizer Constraints and Hardware Setup

The stator terminal connection configurations, the orientation of the rotor with respect to the stator, the stator terminal voltage limits, and the effect of saturated stator inductance are discussed in this section. For this discussion, the impulse magnetizer hardware can be considered as a series LCR circuit as shown in Fig. 3.1 (a). The capacitor C_{bank} is pre-charged to a voltage V_{dc} and connected to the machine stator terminals. Depending on the values of inductance L_s and resistance R_s of the winding, an exponentially decaying current pulse I_{mag} with a peak value of I_p flows through the winding as shown in Fig. 3.1 (b).

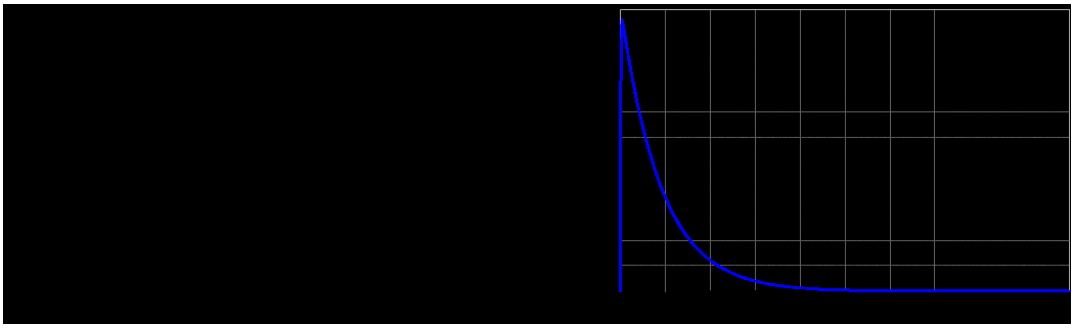

(a) (b)

Fig. 3.1: (a) Magnetizer LCR circuit, (b) Current pulse

Different stator terminal connection configurations (star, delta, and parallel) are possible as shown in Fig. 3.2 (a), 3.3 (a), and 3.4 (a). The resultant current in the stationary $\alpha\beta$-axes are shown in Fig. 3.2 (b), 3.3 (b), and 3.4 (b). A comparison of the different configurations are provided in Table 3.1. From the example provided in Table 3.1 for $V_{dc} = 1000\ V$, it is evident that the parallel connection of the stator terminals provides the highest value of $I_\alpha = 2000\ A$ which in turn results in the highest magnetizing field strength. However, the peak current drawn from the magnetizer is the highest for the parallel connection scheme. Hence, the power handling

components in the magnetizer need to be rated for high current. In addition, the parallel connection scheme requires all six terminals of the stator winding.

For the star configuration, the value of $I_\alpha = 1000\ A$ is higher than the peak current from the magnetizer, $I_p = 667\ A$. But the effective resistance R_{eff} offered by the winding to the magnetizer is high and hence, for a given value of V_{dc}, the magnetizer can generate less current compared to the other cases. In the delta configuration, the effective resistance is low compared to the star configuration and can generate a higher value of I_p for the same V_{dc}. But the value of I_α is the same as the value of I_p. The value of I_{wp} for different configurations should be taken into account for calculating the rise of the winding temperature upon applying the current pulse.

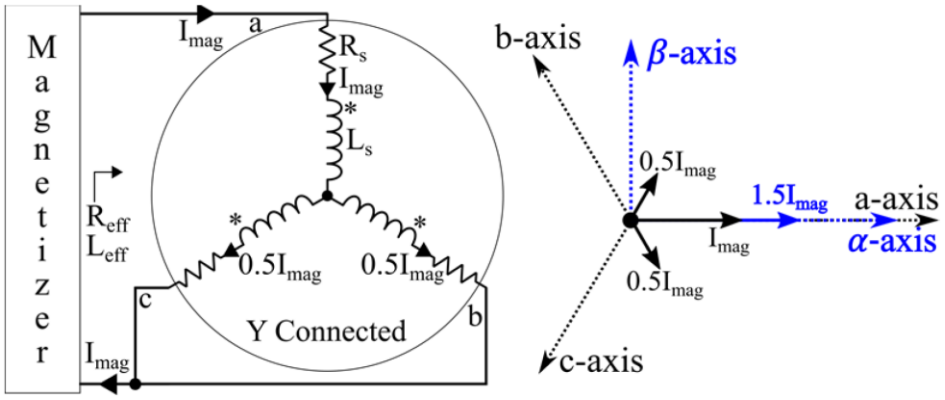

(a) (b)

Fig. 3.2: (a) Stator star connected to magnetizer (b) Resultant magnetizing current on $\alpha\beta$-axes

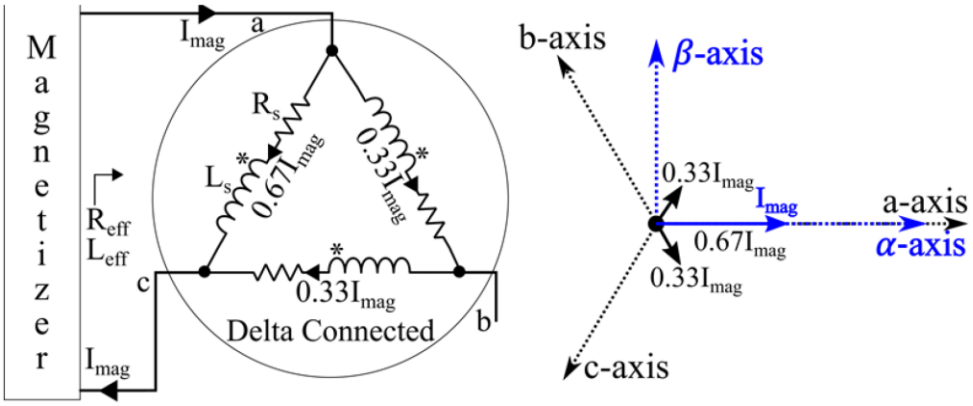

(a) (b)

Fig. 3.3: (a) Stator delta connected to magnetizer (b) Resultant magnetizing current on $\alpha\beta$-axes

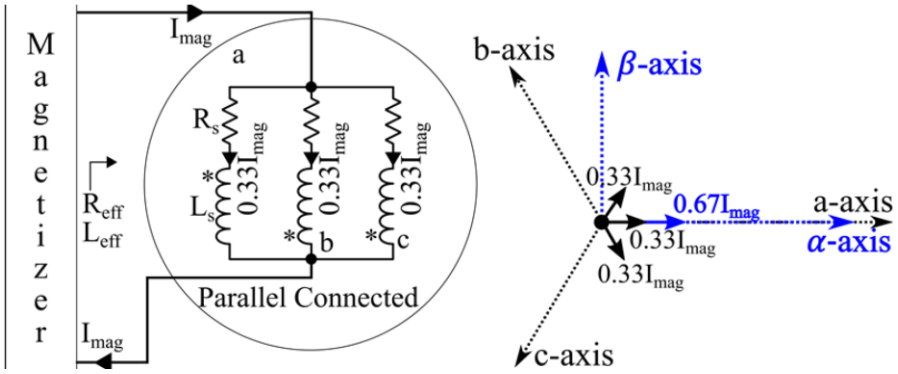

(a) (b)

Fig. 3.4: (a) Stator parallel connected to magnetizer (b) Resultant magnetizing current on $\alpha\beta$-axes

TABLE 3.1: COMPARISON OF STATOR TERMINAL CONFIGURATIONS

Stator Connections	R_{eff}	***α-axis current*** (I_α)	***Highest winding current*** (I_{wp})	***For*** $V_{dc} = 1000\ V$ $(L_s = 0\ \&\ R_s = 1\Omega)$		
				I_α ***(A)***	I_p ***(A)***	I_{wp} ***(A)***
Star	$1.5R_s$	$1.5I_{mag}$	I_{mag}	1000	667	667
Delta	$0.67R_s$	I_{mag}	$0.67I_{mag}$	1500	1500	1000
Parallel	$0.33R_s$	$0.67I_{mag}$	$0.33I_{mag}$	2000	3000	1000

For a given stator and the terminal connection configuration, the value of V_{dc} can be increased to achieve a higher value of magnetization current. However, the limit on the maximum voltage that can be safely applied on the stator terminals without causing insulation failure puts a constraint on the value of V_{dc}. The stator used in this work was impulse tested using a voltage level of $1500\ V$ by the manufacturer and hence it was chosen as the limit of V_{dc} in this work. From Fig. 3.2 (b), 3.3 (b), and 3.4 (b), it is evident that the resultant magnetization current is along the α-axis in the stationary frame of reference. The expected d-axis of the magnet should be kept aligned with the stator α-axis and the rotor have to be tightly clamped to prevent any movements while applying the magnetization pulse. In Fig. 3.1 (b), the current pulse waveform shows a sharp rise in its value at the starting. This is true only if the value of the winding inductance L_s is near zero. In practice, the rise time of the current is decided by the value of L_s. As the current increases, the stator gets

saturated and the inductance falls to a small value $L_{s,sat}$ which can still be a significant value and reduce the achievable peak current. A finite element analysis (FEA) software simulation is performed to obtain the variation of L_s versus current. In the magnetization process, the magnetization current appears along the α-axis only ($I_\beta = 0$) and since the d-axis of the rotor and the α-axis are aligned, only the d-axis inductance (L_d) of the SPMSM needs to be considered. The plot of L_d versus I_d for the SPMSM used in this work is given in Fig. 3.5. The nominal value of L_d is 3.75 mH which lowers to about 0.5 mH at 1500 A. The prototype of the magnetizer is shown in Fig. 3.6. A self-test is performed by pre-charging the capacitor bank and turning on the thyristor with the output terminals of the magnetizer shorted. The peak current obtained was 1800 A at $V_{dc} = 300\ V$. This verifies that the prototype built is capable of delivering the required current.

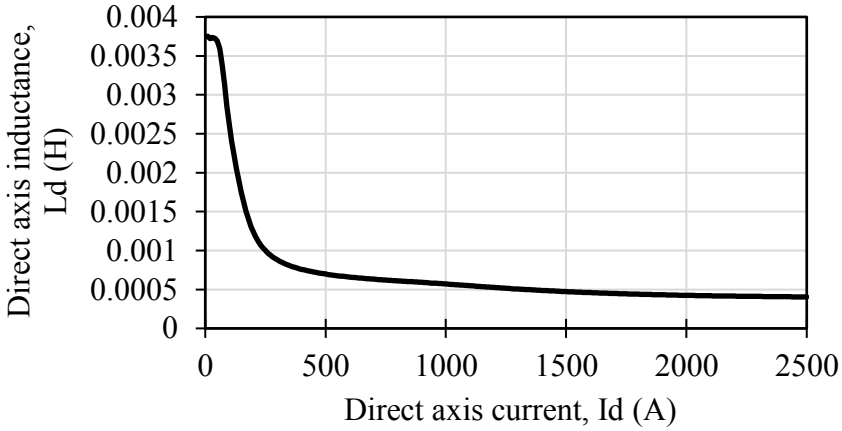

Fig. 3.5: d-axis inductance L_d versus d-axis current I_d

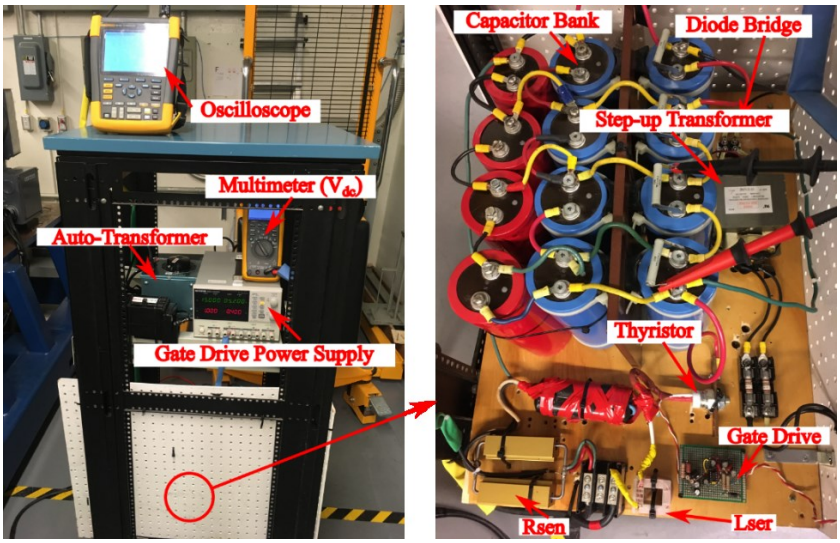

Fig. 3.6: Magnetizer prototype

3.3. *Magnetization Test Results of the Cold Spray PM Rotor*

The prototyped magnetizer is used to magnetize a PMSM with a cold-sprayed PM. In the star configuration, the value of peak current obtained was 1240 A at $V_{dc} = 1380\ V$. To obtain a higher current, the connection was changed to the delta configuration. The peak current obtained is 2000 A at $V_{dc} = 1380\ V$. The magnetization current pulse applied is shown in Fig. 3.7.

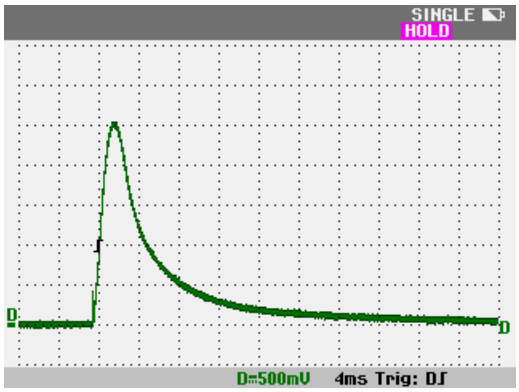

Fig. 3.7: Magnetization pulse, 2000 A peak, delta connected stator

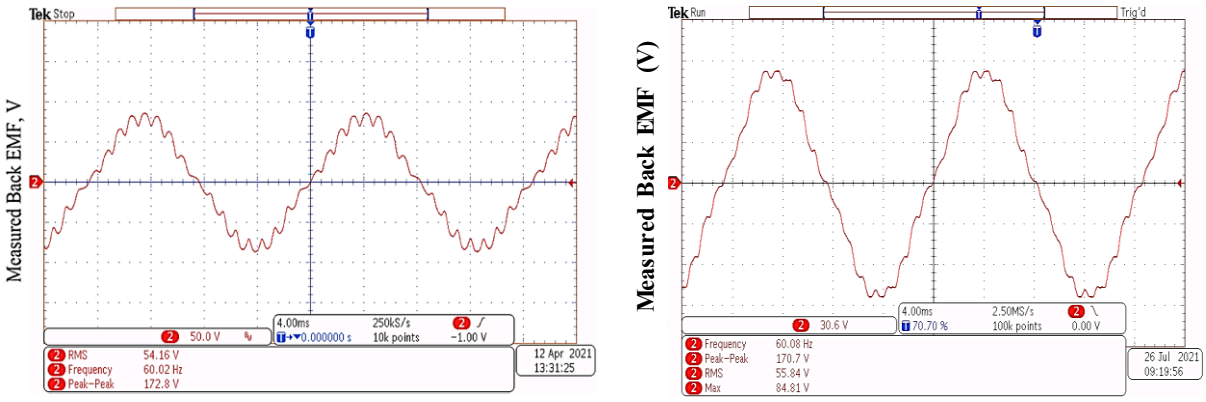

(a) (b)

Fig. 3.8: Back-EMF waveform after magnetization. (a) before shifted by 5° mechanical and (b) after shifted by 5° mechanical

It can be observed that the edges of the magnet are not magnetized fully when compared to the center region. This is due to the fact that the magnetic field generated by the stator coils is concentrated at the center of each pole. In addition, the center region is also magnetized non-uniformly. This non-uniform magnetization is due to the effect of stator teeth openings where the magnetic field is low. To address these issues and improve the back-EMF, the surface PM pole

rotor d-axis is aligned and rotated in both clockwise and anti-clockwise directions by half slot-pitch that is by 5° mechanical, and again the magnetization pulse of 2000 A is supplied to the stator windings. The back-EMF waveform obtained after magnetization at around 60 Hz before and after 5° mechanical shifts are shown in Fig. 3.8 (a) and (b) respectively. The back-EMF constant obtained is 0.9 V_{rms}/Hz and 0.93 V_{rms}/Hz. The simulation of the fully magnetized rotor gives a back-EMF constant of 0.97 V_{rms}/Hz. In order to analyze the magnetization profile, the rotor was removed from the machine and a Hall probe (Exetech MF100) was used to measure the flux density distribution on the surface of the magnets. The magnet surface was divided into 39 rectangular strips and one measurement was taken in each strip at the center of the magnet. The flux density distribution before and after 5° mechanical shifts are provided in Fig. 3.9 (a) and (b) respectively.

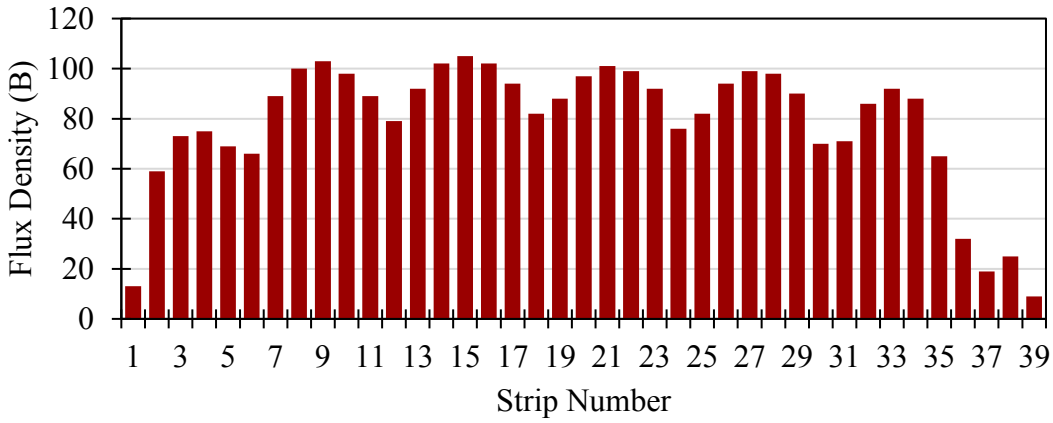

(a)

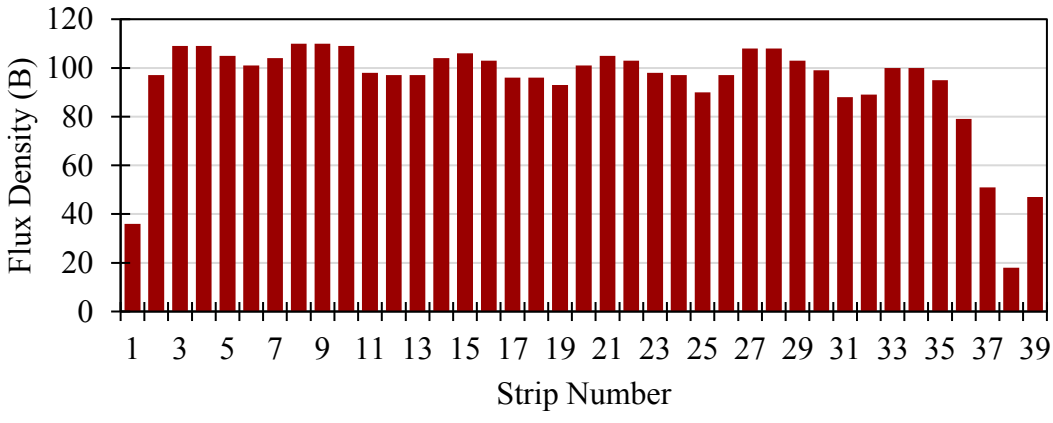

(b)

Fig. 3.9: Flux density distribution along the surface of the PM after magnetization. (a) before shifted by 5° mechanical and (b) after shifted by 5° mechanical

3.4. Experimental Electromagnetic Analysis of the Cold Spray PM Machines

The cold spray rotor for Model A with unskewed, Model B with skewed PM, and Model C with sinusoidal-petal shaped PM were all prototyped using cold spray additive manufacturing and machined to final dimensions. The 4 pole rotor core is made up of solid steel and a NdFeB-based powder mixed with an aluminum binder is used for magnet fabrication. Deposited magnets exhibited a remanence of 0.46 T. More details on the fabrication process and the magnet properties can be found in [32]. The 36-slot unskewed stator core is made up of M36G29 lamination steel sheets with a thickness of 0.35 mm. The double-layer lap-type 3-phase configuration is used as the stator winding. The additively manufactured cold-sprayed rotor PMs for Model A, B, and Model C are shown in Fig. 3.10 respectively. All three rotor cores models are assembled and magnetized in-situ post assembly with the same stator core.

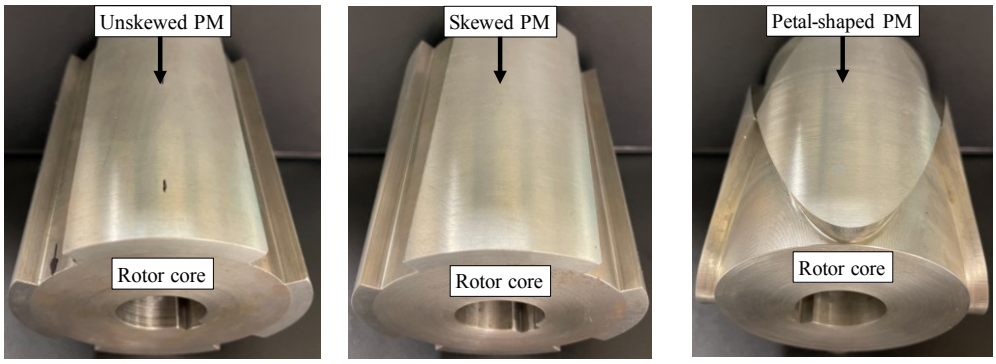

(a) (b) (c)

Fig. 3.10: Rotor core with cold-spray NdFeB PM using the additively manufacturing technique. (a) Model A with conventional rectangular shaped unskewed PM (b) Model B with conventional rectangular shaped skewed PM and (c) Model C with sinusoidal-petal shaped PM

To begin the performance comparison analysis, the back EMF of the Model A, B, and C cores are measured at the rated speed of 1800 rpm at no-load. The back EMF for all three rotor cores is shown in Fig. 3.11 (a), (b), and (c). During the in-situ magnetization process, the majority of the magnetic field lines are concentrated at the d-axis of the PM pole located at the center of the PM. Hence, the edges of the PM pole are not magnetized completely. The back EMF is the derivative of the flux linkage, therefore the tip of the back EMF waveform represents the flux linkage due to the edges of the PM pole whereas the zero-crossing of the back EMF represents the flux linkage due to the center portion of the PM pole.

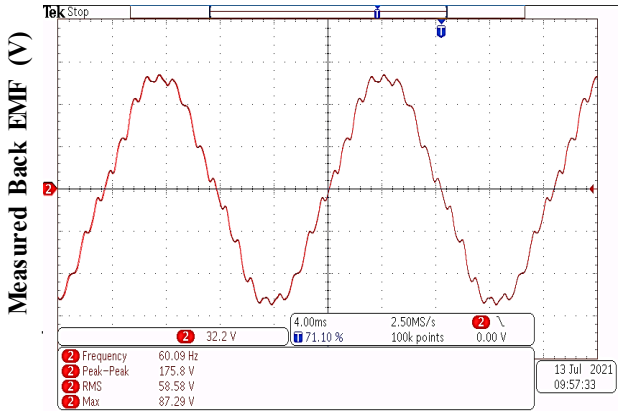

(a)

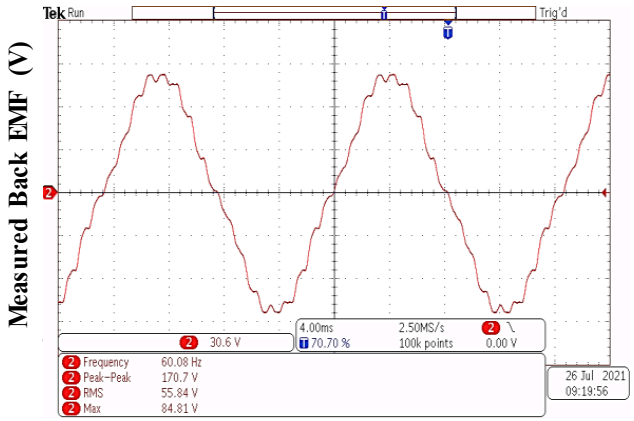

(b)

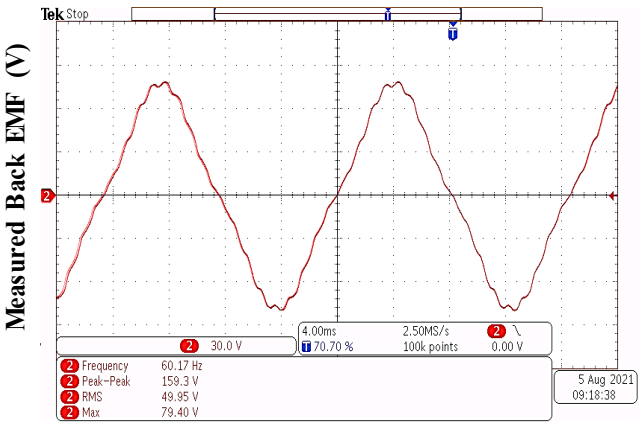

(c)

Fig. 3.11: Measured phase back EMF at no-load for rotor core with cold-spray NdFeB permanent magnet using the additively manufacturing technique. (a) Model A with conventional rectangular shaped unskewed PM (b) Model B with conventional rectangular shaped skewed PM and (c) Model C with sinusoidal-petal shaped PM

In the case of Model A with unskewed PM, as both stator and rotor core are unskewed the effects of slot-harmonics are higher compared to the skewed PM and petal-shaped PM as shown in Fig. 3.11 (a). In the case of Model B with skewed PM, as the edges of the PM poles could not get magnetized properly during the in-situ magnetization process, the effect of the reduced slot-harmonics in the back EMF waveform is not observed as expected from the FEM simulation results. The measured phase back EMF for Model B with skewed PMs is shown in Fig. 3.11 (b). Whereas in the case of Model C with sinusoidal-petal shaped PM, it is observed that the effect of slot-harmonics is reduced compared to both Model A and B designs. Similarly, due to the non-magnetization of the PM edges, its back EMF still contains ripple at the tip of the waveform as shown in Fig. 3.11 (c). Nonetheless, it is fair to compare and validate the effect of PM shape as the stator core used for testing and in-situ magnetization process are the same for all three rotor cores. Therefore, the THD analysis of the measured phase back EMF waveforms was performed and tabulated in Table 3.2. The THD for Model A with unskewed PM is the highest at 7.5 %, for Model B with skewed PM it is reduced to 6.24 % whereas for Model C with petal-shaped PM, it is further reduced to 3.07 %. Generally, the experimental results and FEM-based simulated results for phase back EMF for all three rotor cores do not match due to the non-uniform in-situ magnetization of the PM poles. It is however observed that Model C has the lowest THD among all three rotor PM designs.

TABLE 3.2: HARMONIC ORDER OF EXPERIMENTAL MEASURED PHASE BACK EMF FOR MODEL A, B, AND C

Back EMF Harmonic Order	***Model A***	***Model B***	***Model C***
Fundamental (V)	84.39 V peak	80.49 V peak	72.05 V peak
3rd Harmonics (%)	3.86	2.66	0.70
5th Harmonics (%)	3.03	3.15	1.36
7th Harmonics (%)	0.70	0.57	0.25
9th Harmonics (%)	0.15	0.17	0.23
11th Harmonics (%)	0.30	0.24	0.18
THD (%)	7.50 %	6.24 %	3.07 %

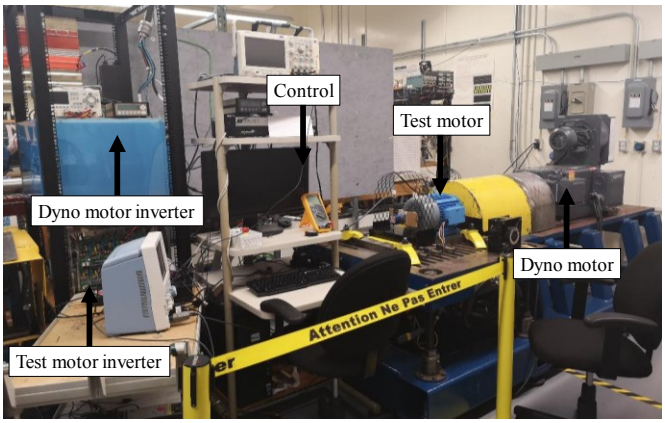

Fig. 3.12: Experimental setup to measure the electromagnetic torque vs rotor position characteristic in a test motor with Model A, B, and Model C shaped rotor PMs

To measure torque ripple characteristics of the machine, the rotor position is measured with the help of an absolute encoder and then it is aligned and locked at a zero electrical degree position. The experimental setup to measure torque is shown in Fig. 3.12. For a fixed rated stator current of 20 A peak and torque-angle reference, the output electromagnetic torque of the machine is measured and recorded. The rotor position is then rotated in steps of 2.5 electrical degrees and with a fixed rated stator current, the output electromagnetic torque is recorded for a half electrical cycle that is up to 180 degrees electrical. The recorded data are post-processed to obtain the average electromagnetic torque and torque pulsation of the machine. Fig. 3.13 presents the measured electromagnetic torque waveform for Model A, B, and C for a half electrical cycle. In the case of Model A with an unskewed rotor PM pole, the average torque is 14.27 Nm with a torque pulsation of 19.27 %. Whereas for Model B with a skewed rotor PM pole, the average torque ripple is reduced to 13.11 Nm which is inferior by 8.12 % compared to Model A with unskewed rotor PM with a torque pulsation of 18.68 %. Analytically, the average electromagnetic torque of the skewed machine is reduced by the fundamental skew factor (K_{s1}) as shown in equation (3.1) where σ_s is the skew angle in electrical radians. In Model B the rotor PM pole is skewed by 10 degrees mechanical. Therefore, the average electromagnetic torque should be reduced by about 0.5 %. As the edges of the PM pole are not magnetized properly, the effect of skewing is not observed as expected from the FEM-based simulated results.

$$K_{s1} = \frac{\sin(\frac{\sigma_s}{2})}{\frac{\sigma_s}{2}} \tag{3.1}$$

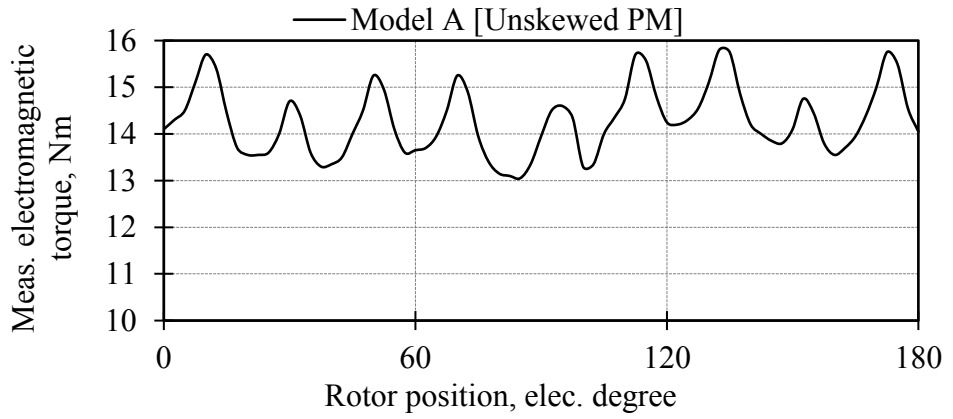

(a)

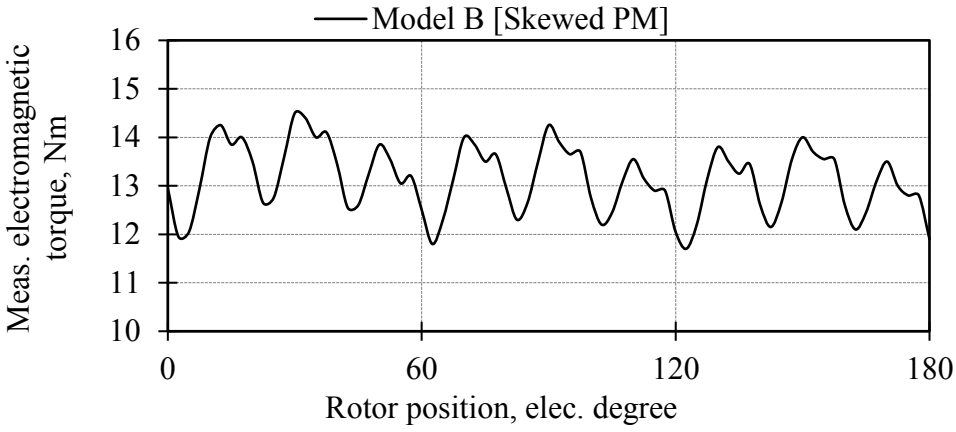

(b)

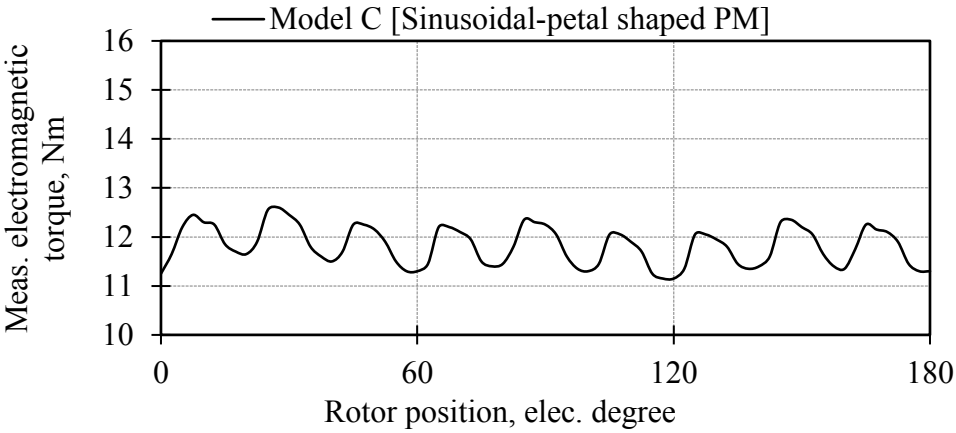

(c)

Fig. 3.13: Measured electromagnetic torque vs rotor position at full load for rotor core with cold-spray NdFeB PM using the additively manufacturing technique. (a) Model A with conventional rectangular shaped unskewed PM (b) Model B with conventional rectangular shaped skewed PM and (c) Model C with sinusoidal-petal shaped PM

In the case of Model C with a petal-shaped PM pole, the average electromagnetic torque is 11.81 Nm with a torque pulsation of 9.31 %. As discussed in section IV, due to the magnetic flux leakage at the edges of the petal-shaped PM the average torque is reduced by 17.2 %. However, it is observed that the torque pulsation in Model C is the lowest among all the rotor PM designs. The torque pulsation is reduced by 51.68 % due to the shaping of the PM pole compared to Model A with unskewed PM. Finally, the cogging torque of the machine is measured and compared using a high-precision torque transducer. Fig. 3.14 shows the experimental setup to measure cogging torque which consists of a gear motor with a constant speed of 1 rpm and a gearbox with a 1/5 ratio. The machine is rotated at a constant speed of 1/5 rpm. The sensed cogging torque is transferred and plotted to the computer system through a USB-based communication cable.

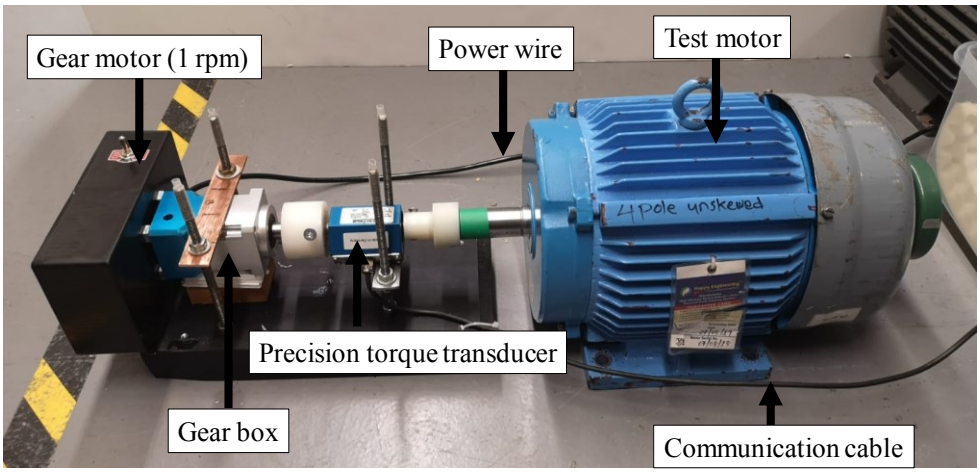

Fig. 3.14: Experimental setup to measure the cogging torque in a test motor with Model A, B, and C rotor PMs

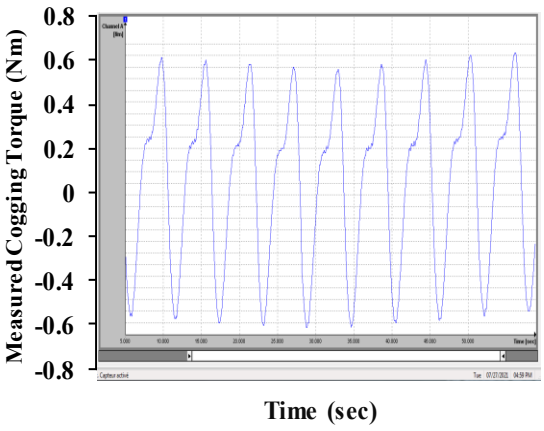

(a)

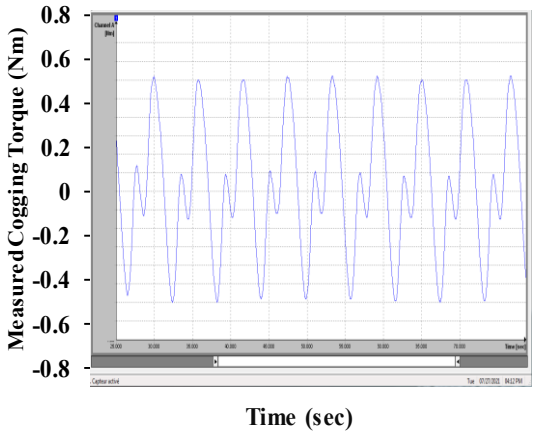

(b)

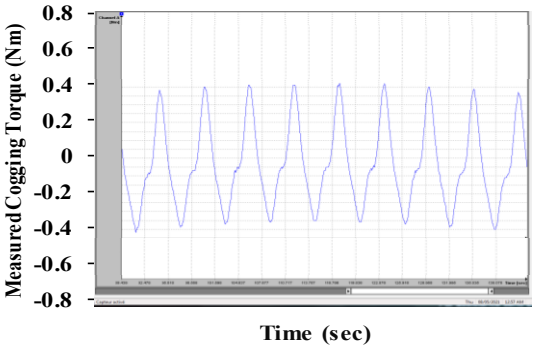

(c)

Fig. 3.15: Measured phase back EMF at no-load for rotor core with cold-spray NdFeB permanent magnet using the additively manufacturing technique. (a) Model A with conventional rectangular shaped unskewed PM (b) Model B with conventional rectangular shaped skewed PM and (c) Model C with sinusoidal-petal shaped PM

The measured cogging torque for Models A, B, and C is shown in Fig. 3.15. Model A and B with unskewed and skewed PMs, the cogging torque measured is almost the same at 1.2 Nm peak to peak whereas, for Model C with petal-shaped PMs, it is reduced to 0.78 Nm peak to peak. Therefore, a petal-shaped PM design improves the performance and reduces the torque pulsation of the machine. The experimental performance analysis for all three rotor designs is summarized and tabulated in Table 3.3. The magnetization obtained using a cost-effective in-situ magnetization technique did not yield a uniform magnetization. Improvements in the apparatus could lead to improved performance. The overall experimental analysis validates that the cold-sprayed additively manufactured PM pole provides flexibility in the magnet shaping and can be used to improve the performance of the electric machines. The simulation versus experimental performance comparison is tabulated in Appendix-I.

TABLE 3.3: EXPERIMENTAL PERFORMANCE COMPARISON OF MODEL A, B AND C

Parameter	***Model A***	***Model B***	***Model C***
Magnet Volume (%)	100 %	100 %	86.89 %
Phase back EMF THD	7.50 %	6.24 %	3.07 %
Cogging torque (pk-pk)	1.2 Nm	1.2 Nm	0.78 Nm
Average torque	14.27 Nm	13.11 Nm	11.81 Nm
Torque ripple	19.27 %	18.68 %	9.31 %

3.5. Conclusions

The design, simulation, prototyping, and testing of an impulse magnetizer to magnetize a cold-sprayed PM rotor is presented in this chapter. The magnetization is done in-situ after assembling the machine. An FEA-based simulation is performed first to obtain the requirements of the magnetizer. Various stator terminal connection configurations to the magnetizer are analyzed and compared. Due to the in-situ magnetization technique of the cold sprayed magnet poles, the magnetic field lines are concentrated at the d-axis and the edges of the poles could not be magnetized completely. Also, the slotted stator stamping laminations create an uneven magnetization pattern across the surface of a magnet pole. Therefore, the measured results do not match with the FEA simulated results perfectly however, the experimental comparison is valid as the same test procedure was used in all three models. The THD in the measured phase back EMF for Model C is 3.07 % and the measured torque ripple is 9.31 % which is the least compared to Model A and B. However, as the number of coil turns in winding is kept the same, the magnetic flux linkage for Model C was less due to the reduced magnet volume and the flux leakage at the edges of the sinusoidal-petal-shaped rotor poles. Hence, the measured average electromagnetic torque of Model C is reduced by 17.2 % compared to Model A with unskewed rotor PM. The measured results do not match with the FEA simulated results perfectly however, the experimental comparison is valid as the same test procedure was used in all three models. This experimental analysis validates that the cold spray additive manufacturing technique can lead to an improvement of the motor performance by improving the design flexibility of the machine parts such as rotor PM shape and can also be used for powdered-based fabrication of the stator and rotor.

CHAPTER – 4

DESIGN OF A SURFACE PMSM USING SOFT MAGNETIC COMPOSITES

This chapter presents the design of a 15 kW surface PMSM using soft magnetic composite (SMC) material. It presents the properties of the different soft magnetic composite materials and their impact on the losses and efficiency of surface-mounted permanent magnet electric motors. It also discusses the criteria for the 7.12 kW surface PMSM design parameters such as magnet flux linkage, the d-q axis inductances, and characteristics currents to achieve a constant power speed range during flux weakening operation.

4.1. Introduction

There is a growing need for high power density electric machines that are driven by the expanding transportation electrification as well as the development of renewable energy applications [52-56]. The advancements in power electronic devices have enabled high operating frequencies (> 500 Hz) that can lead to increased machine power density through greater machine speed and utilizing a high number of poles to reduce the magnetic material weight [57]. However, one of the drawbacks of these approaches is that the core loss in the electrical steel laminations increases rapidly at high speeds as the eddy current loss is proportional to the frequency squared [58]. SMC can be an interesting material for a design alternative as it has high electrical resistivity that can limit the eddy current losses [59]. SMC parts can be manufactured by die compaction of individually electrically insulated iron particles powder. This process produces near-net-shape parts with high dimensional tolerance and a smooth surface finish. The isotropic property of SMC can be exploited by designing unconventional machine structures with 3D magnetic flux paths that would be near to impossible to fabricate using steel laminations. On the other hand, SMC possesses lower magnetic permeability (μ_r < 1000) compared to electrical steel laminations. Therefore, SMC is typically more suitable for permanent magnet machines, where the magnetic circuit reluctance is dominated by the permanent magnets, making the machine performance less sensitive to the core permeability [60]. Different SMC motor topologies have been investigated to achieve high-

performance characteristics [61]. An SMC radial flux permanent magnet motor is presented in [62], where the core back and tooth tip are axially extended over the end windings to reduce the overall motor length. The armature core is subdivided to allow utilizing pre-pressed armature coils with high fill factor and high equivalent thermal conductivity. Recently, axial flux machines with SMC cores have gained increased industrial interest as they can provide high torque density within a short axial length [63-66]. Another promising topology that can exploit the SMC 3D flux carrying capability is the transverse flux machine [67-70]. The unique structure of this machine allows it to achieve exceptionally high torque density when designed with a high number of poles and it also has simple armature coils that can enhance the machine's reliability and simplify its winding process. The range of magnetic, electrical, and mechanical properties of SMC components is relatively extended as their properties can be readily varied by changing the parameters of the manufacturing process thus leading to a large variety of SMC grades. As we know, surface permanent magnet synchronous machines (SPMSM) have generally been considered to be poor candidates for achieving wide ranges of constant-power operation through flux weakening. In this chapter, the criteria to achieve optimal flux weakening are studied for a 7.12 kW SPMSM design.

4.2. SMC Properties for Different Materials

The SMC components are fabricated by coating individual iron powder particles with a resistive coating, adding a lubricant, and then pressing the parts. The resulting SMC structure is illustrated in Fig. 4.1. A subsequent de-lubrification and heat treatment (500-650°C) is required to increase the mechanical strength and decrease the hysteresis loss stemming from the deformation of the individual iron particles during the pressing process. The role of the insulation/resistive coating is to limit the eddy current losses that become significant when the SMC is subjected to higher frequency magnetic fields.

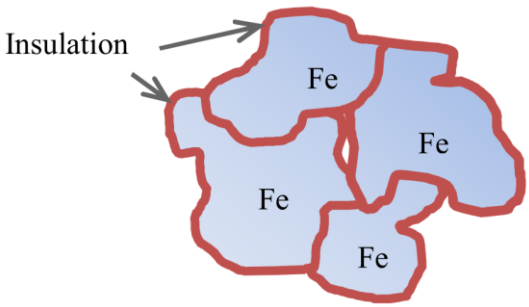

Fig. 4.1: Illustration of SMC structure

Individual SMC magnetic properties can be tailored using appropriate process parameters but generally cannot all be maximized simultaneously. In other words, using current technologies, one cannot fabricate an SMC that has high permeability, low eddy current loss, low hysteresis loss, high saturation field, and high mechanical strength; a trade-off must be made between some of these properties. Table 4.1 summarizes the impact of a few manufacturing parameters on SMC properties. These parameters should be adjusted to ensure that optimized motor performance is achieved. Three SMC materials are selected to investigate their potential for electric machines. Table 4.2 shows the properties of the three materials (A, B, and C), and their pictorial representation is shown in Fig. 4.2 [71]. Material A is selected for its very high electric resistivity, which comes at the expense of increased hysteresis loss and reduced permeability. In general, this material is heat-treated at the low end of the temperature range, maintaining strong insulation but also keeping the material coercivity and hysteresis loss high. Material C is heat-treated at a higher temperature, which leads to high permeability and low hysteresis loss, but it also has reduced electric resistivity, which may lead to high eddy current losses. The manufacturing parameters of material B are adjusted to have medium permeability, resistivity, and hysteresis loss.

TABLE 4.1: IMPACT OF MANUFACTURING PROCESS PARAMETERS ON SMC PROPERTIES

Minor changes in powder and process parameters	***Permeability and Saturation***	***Resistivity***	***Hysteresis Losses***
Increase in the powder size	↑	↓	↓
Increase in lubricant content	↓	↑	↑
Increasing compaction pressure	↑	↓	↓
Increasing heat treatment temperature	↑	↓	↓

TABLE 4.2: PROPERTIES OF THE SELECTED SMC GRADES

	Relative permeability	***Hysteresis loss per cycle (mWatt.sec/kg)***	***Resistivity (μΩm)***
Material A	220	143.12	7600
Material B	440	95.48	1000
Material C	720	62.86	90

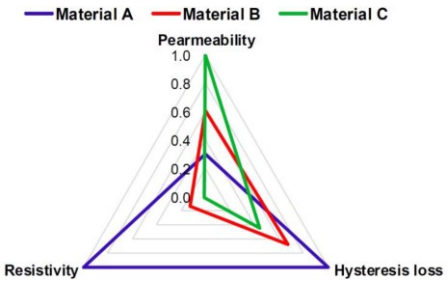

Fig. 4.2: Comparison of three different SMC materials

4.3. Three-dimensional FEM Simulations and Comparisons

The effect of the SMC material properties on the performance of the Radial flux PM machine is analyzed in this section. The design specifications of the machine are listed in Table 4.3. The number of poles and slots is chosen to meet the constant power requirements at high speeds. The structure of the radial flux PM machine is shown in Figs. 4.3. It is a conventional radial flux PM machine with an inner surface type rotor and concentrated stator windings. The SMC stator core of the radial flux motor can be segmented to allow the utilization of pre-pressed windings with a high fill factor. It is simulated using a time-dependent 3D FEA solver.

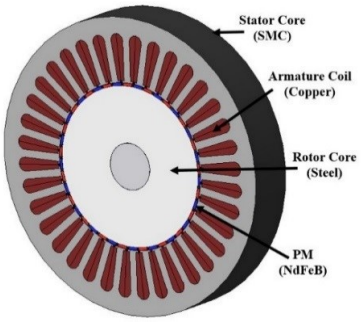

Fig. 4.3: Structure of the radial flux PM machine

Eddy currents are allowed to flow in the SMC based on the rate of change of the magnetic field and the SMC electric resistivity [72]. It is simulated using the three SMC materials (A, B, and C), whose properties are shown in Table 4.2. Fig. 4.4 shows the vector plot of the SMC eddy currents generated in the radial flux machines. Due to the skin effect, the eddy currents tend to be confined toward the surfaces of the SMC core. It is also clear that the eddy current path is highly dependent on the part geometry, which makes it very difficult to estimate using conventional loss calculation methods. The armature current is adjusted for each case to maintain an average torque of 100 N.m and Fig. 4.5 shows the loss components of the machine. The FEA results show that

material A, with high resistivity and low permeability, limits the SMC eddy current loss, but it also causes the highest copper and hysteresis losses. On the other hand, the high permeability material C achieves the lowest copper and hysteresis losses. However, its low resistivity causes significant SMC global eddy currents that result in the highest overall motor losses. It can also be seen from Fig. 4.5 that material B with its medium permeability, resistivity, and hysteresis loss achieved the lowest overall motor losses.

TABLE 4.3: MACHINE DESIGN SPECIFICATIONS

Parameter	***Value***
Base speed (rpm)	1500
Maximum speed (rpm)	7500
Rated output power (kW)	15
Rated torque (N.m)	100
Stator core material	SMC
Permanent magnet	1.2 T NdFeB
Armature current density (A/mm2)	5
Outer diameter (mm)	350
Axial length (mm)	60
Number of poles	42
Number of slots	36

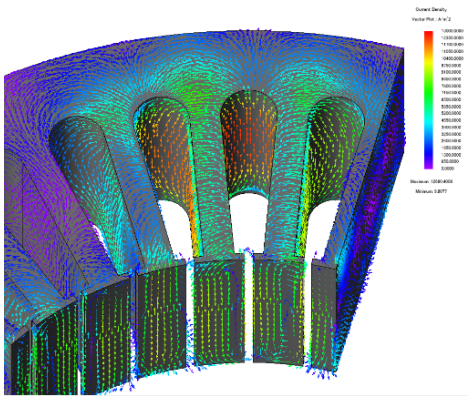

Fig. 4.4: 3D calculated eddy currents in the SMC stator core

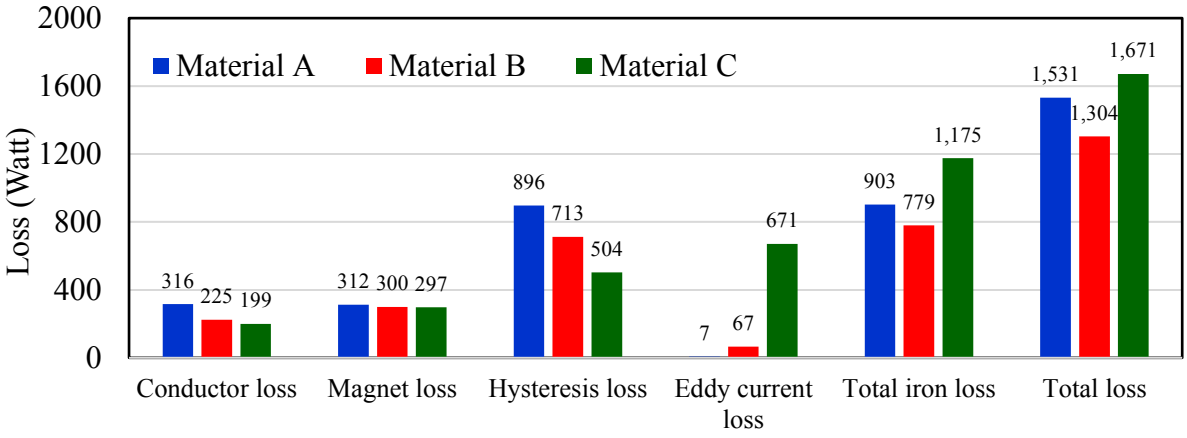

Fig. 4.5: FEA loss components of the radial flux motor at 100 N.m-1500 rpm

Fig. 4.6 (a) and (b) shows the simulated efficiencies of the machines at 100 N.m/1500 rpm and 30 N.m/4500 rpm respectively. It can be seen that material B achieved the highest efficiency followed by material A and then C. It should also be noted that the losses of all the presented machines are dominated by the SMC core loss due to the high frequency and relatively low electric loading. For other machine designs with dominant copper loss components, it is also possible that a high permeability–low resistivity SMC would result in better motor performance.

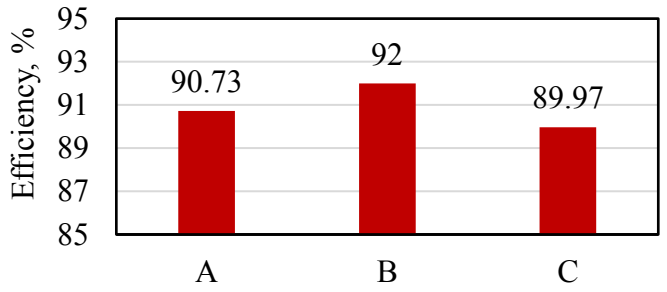

(a)

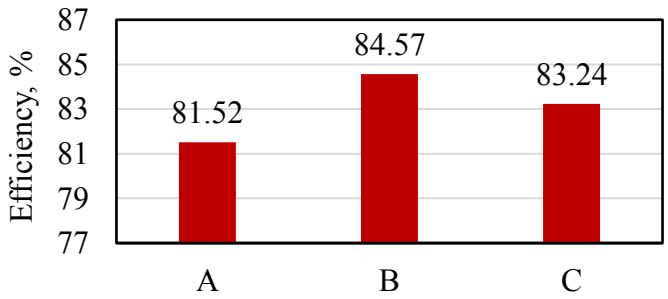

(b)

Fig. 4.6: Efficiency comparison at (a) 100 N.m-1500 rpm (b) 30 N.m-4500 rpm

4.4. Constant Power Speed Range Criteria

The surface permanent magnet synchronous machines (SPMSM) has generally been considered to be poor candidates for achieving wide ranges of constant-power operation through flux weakening. To achieve optimal flux weakening in the SPMSM, the characteristics current should be equal to the rated current of the machine as shown in equation (4.1).

$$I_{ch} \equiv \frac{\Psi_m}{L_d} \tag{4.1}$$

where Ψ_m is the rms magnet flux linkage and L_d is the d-axis inductance (equal to the q-axis inductance for SPM machines). Generally, the inductance of the SPMSM with conventional stator winding is very less, as the PM mounted on the SPMSM acts as an air gap in the machine's magnetic circuit. Also, the magnet flux linkage in PM machines cannot be reduced without compromising its torque-producing capability. For the same amount of magnet flux linkage, concentrated windings offer higher inductance than distributed windings. Therefore, the concentrated winding provides a better opportunity to improve the flux-weakening capability in the SPMSMs. It has been shown that there are several SPP values in the fractional-slot concentrated winding category that can support concentrated windings. However, different SPP values can result in very different machine characteristics. It is very important to select the SPP values that can achieve the highest machine performance. Two families of stator windings corresponding to SPP values of 2/5 and 2/7 emerge as the best candidates [73]. The d-axis magnet flux linkage is directly proportional to the magnet length. By increasing the length of the magnet (l_m), the permeance coefficient (P_c) of the magnet increases as shown in equation (4.2). The inverse of permeance is reluctance and hence the reluctance of the machine reduces. This leads to an increase in the flux linkage of the machine and vice-versa as shown in equation (4.3).

$$P_c = \frac{l_m}{g C_\varphi} \tag{4.2}$$

$$\lambda_{af} = \frac{N^2}{\Re} I \tag{4.3}$$

where, l_m is the magnet length, g is the air gap length, C_φ is the flux concentration factor, $\Re$ is the reluctance, N is the turns of the winding.

There is no straightforward approach to achieving the desired inductance of the machine. It requires an iterative process to adjust the various parameters such as the number of winding turns, air gap length, stator tooth width, and back iron width. By increasing the number of winding turns, the magnitude of inductance increases as shown in equation (4.4), but also this leads to an increase in the back EMF of the machine.

$$L = \frac{\lambda}{I} = \frac{N^2}{\Re} \tag{4.4}$$

By decreasing the air gap length (g), the flux path length (l) of the magnetic circuit decreases, and hence the reluctance also decreases as shown by equation (4.5).

$$\Re = \frac{l}{\mu A} \tag{4.5}$$

where μ is the permeability of the material. As shown in equation (4.4), a reduction in the reluctance will help to increase the inductance of the machine. But, there are mechanical limitations to decreasing the air gap length due to the vibration in the machine when the rotor rotates at high speed. Also, as the air gap length is reduced the heat dissipation of the machine decreases. Hence, the cooling performance becomes poor and affects the life of the machine. The stator tooth width (w_{tb}) and back iron width (w_{bi}) can also be decreased to improve the inductance of the machine as shown in equations (4.6) and (4.7) respectively.

$$w_{tb} = \frac{\varphi_g}{N_{sm} B_{max} k_{st} L} \tag{4.6}$$

$$w_{bi} = \frac{\varphi_g}{2 B_{max} k_{st} L} \tag{4.7}$$

where φ_g is the air gap flux, B_{max} is the maximum flux density, k_{st} is the lamination stacking factor. The flowchart to tune the motor design parameters in order to achieve a constant power speed range is shown below.

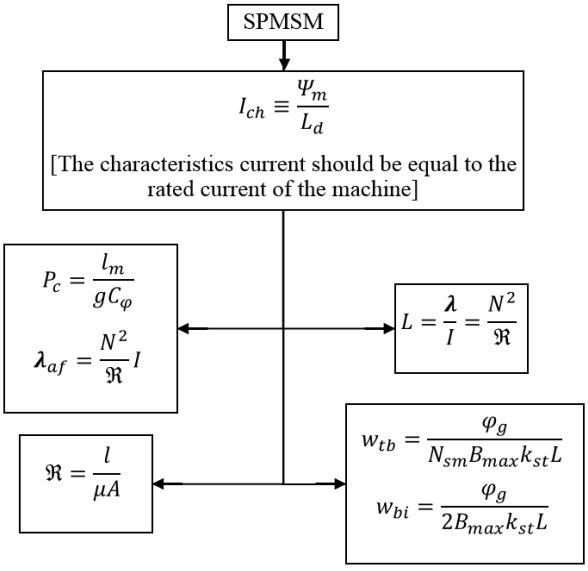

Fig. 4.7: Flowchart to tune the SPMSM design parameters to achieve optimal CPSR

To validate the concept, a 7.12 kW radial flux SPMSM is simulated using the FEA package. Fig. 4.7 shows the isometric view of the designed SPMSM. The base speed is 3400 rpm and the maximum speed of up to 10000 rpm and Table 4.4 summarizes the design parameters. The obtained back EMF, electromagnetic torque, torque-speed, and power-speed characteristics of the SPMSM are shown in Fig. 4.8 (a), (b) and (c) respectively. As can be seen, the designed PMSMs can deliver the rated torque of 20 Nm at 3400 rpm during motoring operation. They can also reach 10000 rpm as per the requirement. The torque pulsation in the waveform for SPMSM is 8.9 % without any machine optimization. These results are obtained by simply matching the analytically calculated parameters. Comparative results between analytical and designed PMSMs are shown in Table 4.4. It can be seen that the analytical and design parameters match closely.

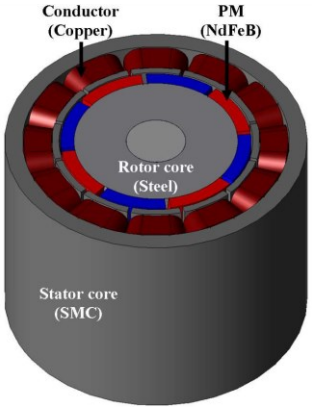

Fig. 4.8: FEA-based model of 7.12 kW SPMSM

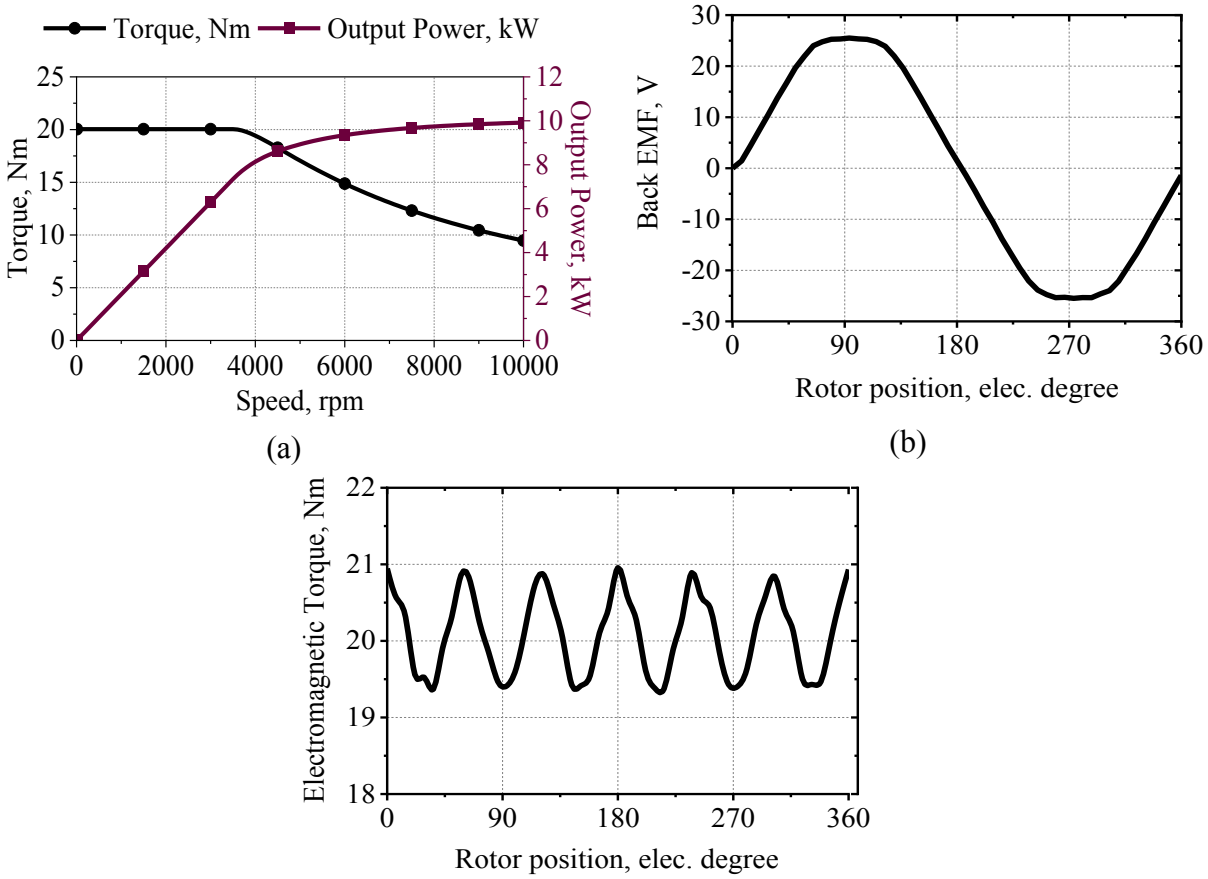

Fig. 4.9: Electromagnetic performance of a SPMSM. (a) torque-power curves, (b) back EMF, (c) electromagnetic torque.

TABLE 4.4: COMPARISON FOR SPMSM

	Analytical (Step I)	***Designed (Step II)***
I_{ch} *[A]*	156.30	156.27
λ_{af} *[Wb-turn]*	0.0214	0.0207
L_d *[mH]*	0.137	0.132
L_q *[mH]*	0.137	0.132

4.5. Conclusions

The impact of SMC material properties on the performance of a 15 kW radial flux is analyzed in this chapter. The FEA simulation results show that an SMC material with a medium magnetic permeability, electric resistivity, and hysteresis loss achieved the best overall motor performance. The requirements in terms of d and q-axis inductances and flux linkage are obtained and serve as a target toward which the machine design parameters should be tuned in the FEA software to obtain optimal flux-weakening. The case study based on a 7.12 kW industrial project validated this method for its ability to speed up the design process as well as estimate feasible parameters that can be matched using FEA software.

CHAPTER – 5

DESIGN OF A 7.12 KW HIGH TORQUE DENSITY PMSM FOR RENAULT TWIZY CAR

This presents the design of a 7.12 kW high torque density surface PMSM for a Renault Twizy car. It discusses the performance improvement of an electric motor using advanced soft magnetic composite (SMC) materials in the stator core and compared it with the laminated steel-based designs for electric vehicle application using 3D finite element software. It also discusses the ring-type Halbach-array rotor for high-speed PMSM design.

5.1. Introduction

For the complete replacement of the gasoline-powered vehicle by hybrid electric vehicles (HEVs) or fully electric vehicles, the electric machine must be as efficient as possible at different operating points [74]. To meet the power requirements, efficiency at different load conditions, installation space, and weight constraints, the selection of a suitable topology of the electric machine is a particularly challenging task. Permanent magnet synchronous machines (PMSMs) are widely used in EV applications due to their distinctive benefits such as high torque and power density, smaller size, and high efficiency [75-76]. In many PMSM designs, rare-earth permanent magnets are usually used. To further enhance the performance of PMSM, magnetic isotropy characteristics of the soft magnetic composite (SMC) material can be used in the machine core. The powder metallurgy technology helps to design and fabricate complex three-dimensional structures of PMSM parts, especially for axial and transverse flux machines. These complex structures in large volumes are difficult to realize using traditional laminated electric steel. Apart from the special physical characteristics, fabrication of the machine using SMC cores can reduce the manufacturing cost as material wastage is reduced and it mainly consists of compaction and heat treatment. The electrical resistance of the SMC materials is higher as it has a thin insulation layer around each iron powder particle, hence the eddy current losses are reduced. On the other hand, the drawbacks of the SMC are that its core loss is high at low frequency due to higher

hysteresis loss and low permeability [77]. For high-speed application, to avoid the risk of the magnet getting detached from the rotor core surface even with using carbon sleeves or high strength sticking glue, interior permanent magnet (IPM) motor topology is preferred over the surface permanent magnet (SPM) topology. Hence, it is important to design a permanent magnet motor with high torque/power density by optimally using the electromagnetic interaction between the rotor PM and the stator. For the radial flux PMSM, the coil end-turns do not contribute to the total flux linkage and thus in torque production. Reducing these coil end-turns will reduce copper loss and the overall size of the machine. Using the cold spray additive manufacturing technique for the permanent magnet fabrication, the surface ring-type Halbach-array magnet can be used for high-speed application. The research on magnetic properties, powder mix composition, metallic binder, robot toolpath programming to spray shaped PM is ongoing at the National Research Council of Canada (NRC-CNRC Canada) [78 – 82]. Two different designs of 24/20 slot-pole and 12/8 slot-pole configuration with laminated steel and SMC material in the stator core with conventional surface permanent magnet rotor are analyzed using JMAG 3D finite-element analysis (FEA) software [83].

5.2. Stator Core Topologies

Traditionally, radial flux machines are prototyped using coated lamination steel sheets which are punched and stacked together axially. These lamination coatings are used to reduce the excessive eddy current losses in the stator core which occurs due to the flux passing perpendicular through it. Hence, in laminated steel stator cores, magnetic flux can conduct only through a two-dimensional plane due to the insulation between the sheets. Various materials such as silicon steel, cobalt-iron, and nickel-iron alloys are used for the manufacturing the of stator core as it exhibits good mechanical properties, high permeability, and high saturation flux density.

However, at the high-frequency operation, the eddy current loss increases significantly in the laminated steel cores which also limits the speed of the machines. The usage of thinner lamination steel sheets is an alternative solution, but it further leads to high manufacturing costs. The SMC's unique characteristics can overcome the above-mentioned drawbacks and help to build a novel machine with a complex structure. SMC materials consist of a high purity fine iron powder particle coated with the insulation material. Hence, its electrical resistance is much higher than that

of laminated steel. Its isotropic magnetic and physical properties help flux to conduct in a three-dimensional direction and effectively dissipate the heat produced from core losses. The typical operating saturation flux density and frequency regions for SMC material, laminated electrical steel, and ferrite cores are shown in Fig. 5.1 [84 – 87].

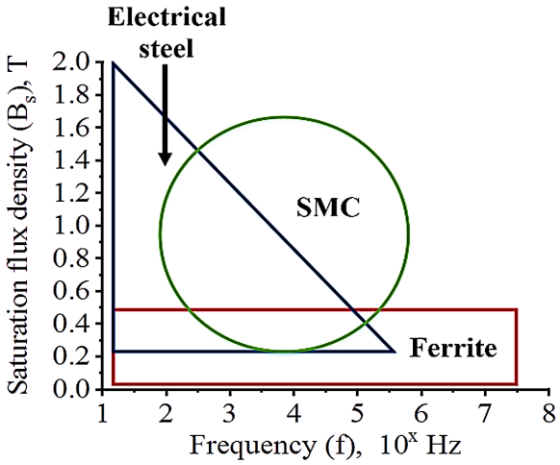

Fig. 5.1: Typical operating regions of SMC material, laminated steel, and ferrite [84-87]

Furthermore, the product developed using SMC material uses compaction, heating, and pressing techniques to achieve the desired shape and final size of the machine core parts. Hence, the material wastage is lower as compared to the laminated steel core. Besides, the machine parts with high surface quality and tolerance for complex geometry can be prototyped using SMCs resulting in high material utilization. However, the disadvantage of using SMC materials is higher hysteresis losses which is the dominant iron loss component at low-frequency operation. It also has lower magnetic permeability compared to laminated steel sheets. Therefore, the SMC is not suitable for applications such as reluctance machines because it requires a high magnetizing current. PM-assisted synchronous machines with large air gaps are more suitable for the application of SMC.

Radial flux machines are the most widely used as traction machines especially the permanent magnet topology with high energy density and limited space or volume requirement. Direct replacement of the electrical laminated steel cores with SMC cores will not improve the performance of the machines. Therefore, if carefully designed considering the advantages of the SMC material such as 3D flux capability and low eddy current losses, the machine performance can be improved. As the number of poles increases, the frequency of the supply also increases to

achieve the same base speed of the machine. Therefore, a 20-pole radial flux machine is considered with a base speed of 3400 rpm and a maximum speed of 10,000 rpm. The supply frequency at base speed is 566.67 Hz and at maximum speed is 1.667 kHz. This high-frequency operation region will help to validate the effect of iron loss in the laminated and SMC stator cores. But due to the higher number of poles, the manufacturing cost involved to cut lamination steel sheets will increase the cost of the machine. Therefore, the most popular 8 pole configuration design is also considered in this chapter for comparison analysis. For the 8-pole design, the supply frequency at a base speed of 3400 rpm is 226.67 Hz and for a maximum speed of 10,000 rpm is 666.67 Hz. The SMC stator core with the segmented tooth is initially fabricated and then later assembled to form a complete stator core. Therefore, pre-wound and pressed copper winding coils can be used to increase the high fill factor of the machine. For 20-pole and 8-pole designs, a 40 % copper fill factor is used for the lamination steel stator core and a 60 % copper fill factor for the SMC stator core with the concentrated winding pattern. As the SMC powders are compacted to form each stator tooth, the stack height of a tooth body can be reduced to adjust the overhang end-turns of the machine as shown in Fig. 5.2. This is not possible in the laminated steel sheet stator core as the magnetic flux path is limited to the two-dimensional pattern. This will help to reduce the overall stack height and volume of the machine, which is one of the key design requirements in the electric vehicle's application. Due to the high copper fill factor in the SMC stator core, to maintain the same current density for comparison analysis, the slot area of the SMC stator core is reduced and hence it leads to a smaller outer diameter of the machine as shown in Fig. 5.3.

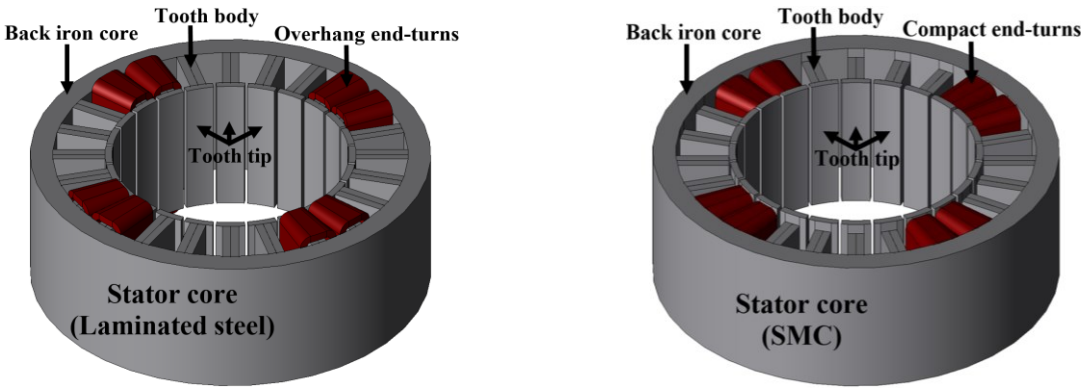

(a) (b)

Fig. 5.2: Isometric view of the stator with concentrated windings for 24/20 slot-pole configuration with a-phase windings. (a) Laminated steel stator core. (b) Soft magnetic composite stator core

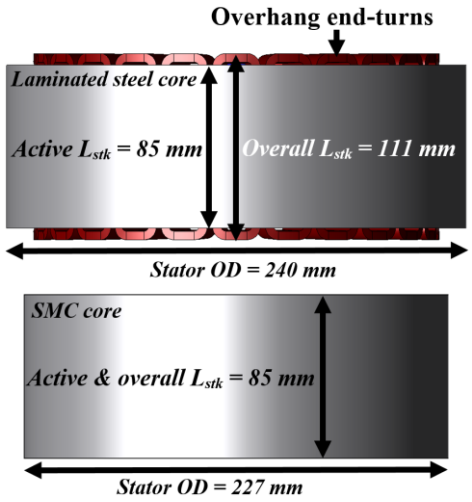

Fig. 5.3: Side view of the stator for 24/20 slot-pole configuration with laminated steel stator core and soft magnetic composite stator core

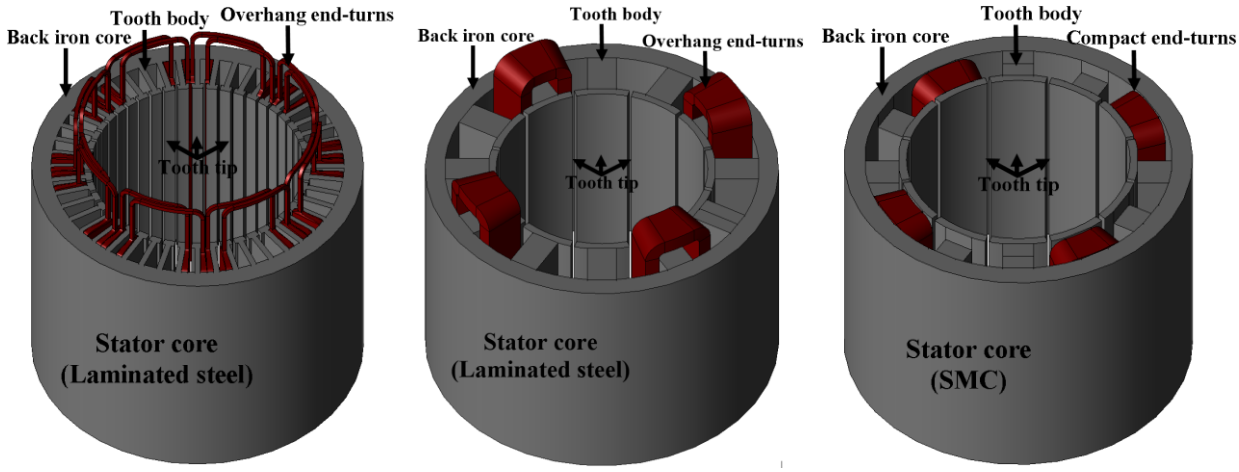

(a) (b) (c)

Fig. 5.4: Isometric view of the stator core with a-phase winding. (a) 48/8 slot-pole with laminated steed stator core. (b) 12/8 slot-pole with laminated steel stator core. (c) 12/8 slot-pole with SMC stator core.

Similarly, the 8 pole PMSM with 12 slots are designed using laminated steel and the SMC stator core. In the application of traction vehicles, the 8-pole and 48 slots laminated steel design is highly popular. Therefore, to compare the torque density of the presented design in this chapter, the 8-pole with 48 slots design with distributed winding is also considered as shown in Fig. 5.4. The output torque of the machine is dependent on the outer diameter and stack length of the rotor.

Therefore, to compare the effect of the laminated steel versus SMC stator core material, the rotor outer diameter, and stack length are kept the same for the 20-pole and 8-pole designs. The stacking factor of the laminated steel core is assumed to be 97 %. The material used for the rotor core is laminated steel of M36G29 for all the designs as SMC materials cannot be used for the rotating parts of the machine due to its poor strength capability. The surface-mounted permanent magnet fabricated using cold spray additive manufacturing with 0.49 T without any shaping is considered for comparative analysis. Section IV will discuss the ring-type Halbach-array permanent magnet rotor topology for the stator core with the best performance.

5.3. Three-dimensional FEM Simulations and Comparisons

The back EMF of 24/20 slot-pole design with laminated steel and SMC stator core were simulated at no-load and at the rated speed of 3400 rpm as shown in Fig. 5.5. Back EMF is proportional to the product of stack length and diameter of the machine assuming constant average airgap flux density. Due to the low permeability of an SMC material and reduced outer diameter of the machine, the peak phase back-EMF is reduced by 12.5 % for the SMC stator core compared to the lamination steel core. Hence the current magnitude is increased by 16.4 % to achieve the same average electromagnetic torque. The electromagnetic torque for the 24/20 slot-pole design is around 20.2 Nm with the torque ripple of 3 % for both the designs as shown in Fig. 5.6. Based on the existing literature [88], the machine belonging to slot per pole per phase (SPP) families of 2/5 and 2/7 is the best configuration for optimal flux weakening in surface PM machines. As 24/20 slot-pole configurations with three-phase supply belong to SPP value of 2/5, it achieves constant-power speed range (CPSR) during flux-weakening operation up to 10,000 rpm. Fig. 5.9 (a) and (b) show the torque versus speed and power versus speed curve for the 24/20 slot-pole design. Similar effects for the 8-pole design with 48 slots and 12 slots were observed. The peak phase back EMF for the 12/8 slot-pole design with SMC stator core is reduced by 9.4 % compared to the 48/8 slot-pole design and 12/8 slot-pole design with the laminated steel core. Therefore, the current magnitude is increased for the 12/8 slot-pole design with the SMC stator core to achieve the same average torque magnitude as shown in Fig. 5.7 and Fig. 5.8. The torque ripple for the 48/8 slot-pole design with laminated steel core is 1.9 % whereas for the 12/8 slot-pole design is 8.9 % for both the design with laminated steel and SMC core. Although the torque ripple is lower in the 48/8 slot-pole design, its SPP value is 2 and has a poor CPSR. The maximum speed attained by the 48/8

slot-pole design is 7500 rpm as shown in Fig. 5.10 (a). Both the 12/8 pole designs with laminated steel and SMC stator core belong to an SPP value of 0.5 and have good CPSR as it reaches up to a maximum speed of 10,000 rpm with almost constant power during flux weakening region as shown in Fig. 5.10 (b) and (c).

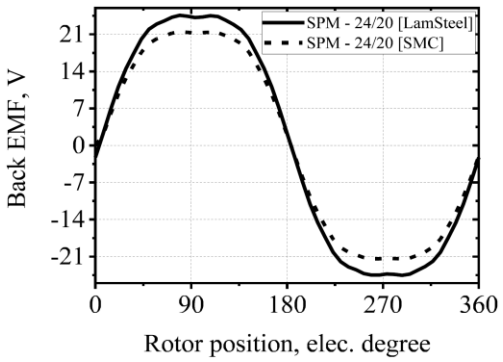

Fig. 5.5: Back EMF for 24/20 slot-pole configuration with laminated steel stator core and soft magnetic composite stator core

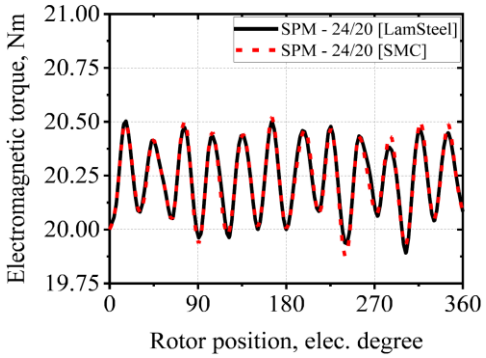

Fig. 5.6: Electromagnetic torque for 24/20 slot-pole configuration with laminated steel stator core and soft magnetic composite stator core

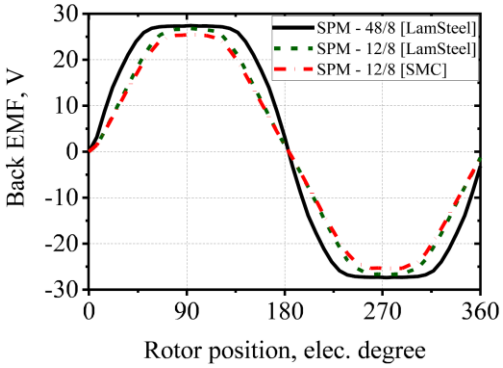

Fig. 5.7: Back EMF for 48/8 and 12/8 slot-pole configuration with laminated steel stator core and soft magnetic composite stator core

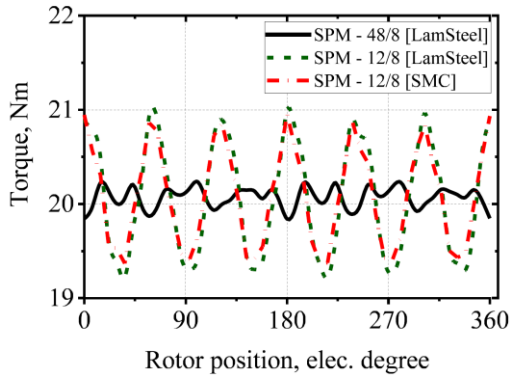

Fig. 5.8: Electromagnetic torque for 48/8 and 12/8 slot-pole configuration with laminated steel stator core and soft magnetic composite stator core

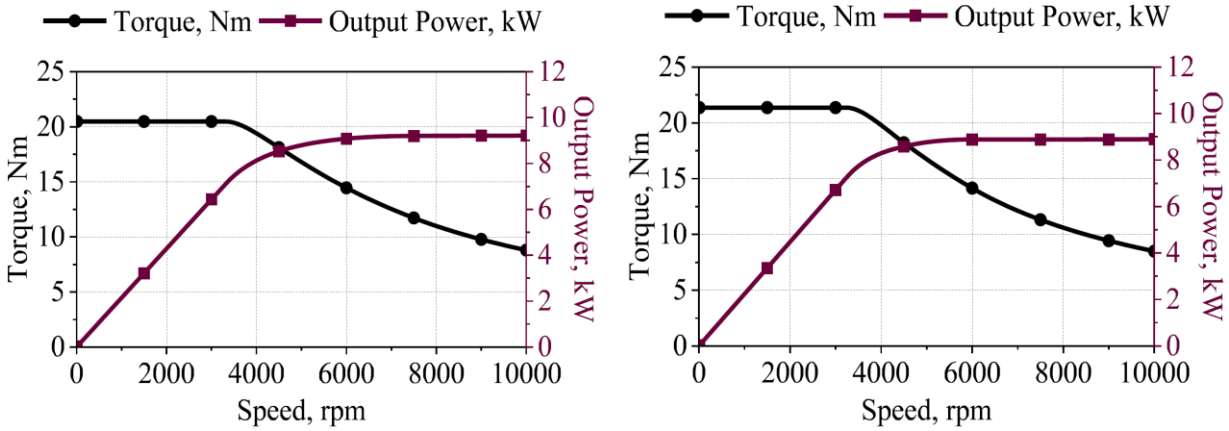

(a) (b)

Fig. 5.9: Torque-speed and power-speed curve for 24/20 slot-pole configuration. (a) laminated steel stator core. (b) soft magnetic composite stator core

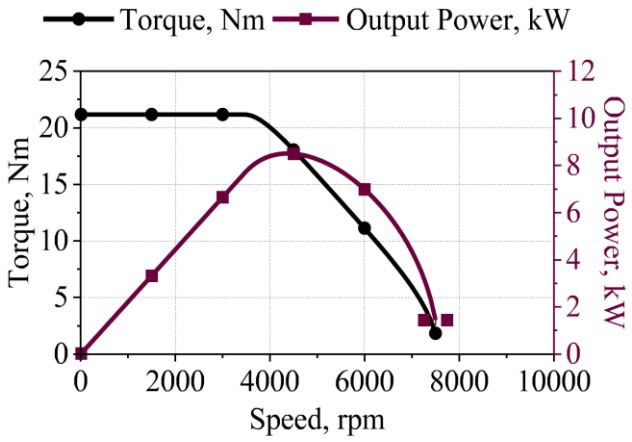

(a)

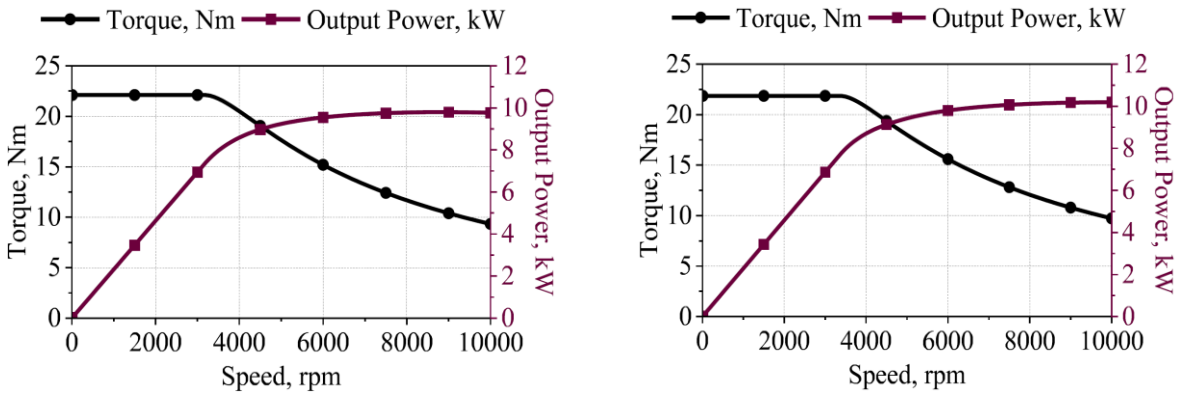

(b) (c)

Fig. 5.10: Torque-speed and power-speed curve. (a) 48/8 slot-pole with laminated steel stator core. (b) 12/8 slot-pole with laminated steel stator core. (c) 12/8 slot-pole with soft magnetic composite stator core

Table 5.1 finally summarizes all the designs discussed above. The overall stack length of 24/20 slot-pole design with SMC stator core is reduced by 23.42 % compared to its design with laminated steel core due to compact end-turns. Similarly, for the 12/8 slot-pole design with SMC stator core, 32.4 % and 20.3 % reduction in overall stack length compared to 48/8 and 12/8 slot-pole design with laminated steel core respectively. The phase resistance of both the designs with SMC stator core is reduced due to short copper winding length, but the conductors per slot increase as the fill factor is increased to 60 %. Also, the copper losses are high compared to a laminated steel core design as the current magnitude is increased to achieve the same electromagnetic torque. The total losses for a high number of pole design that is 24/20 slot-pole with SMC stator core at maximum speed are less due to lower eddy current loss compared to the laminated steel core. Therefore, it was observed that SMC materials perform better at high-frequency supply in terms of core losses.

The overall volume of the machine with SMC stator core design for both 24/20 and 12/8 slot-pole is reduced. High torque density is achieved, in the case of 20 poles with 24 slots design the torque density increases by 45.97 % and for 8 poles with 48 slots and 12 slots design, it increases by 47.89 % and 43. 96 % respectively as shown in Table 5.1. Therefore, considering the high-speed traction application, usage of SMC material to build machine parts helps to improve the torque density, reduces the copper wastage and weight also reduces the core losses in the PM machines.

TABLE 5.1: COMPARISON TABLE FOR 20 POLE AND 8 POLE DESIGN WITH LAMINATED STEEL AND SMC STATOR CORES

	Lam. Steel (24/20) [I]	***SMC Steel (24/20) [II]***	***Inference [I vs. II]***	***Lam. Steel (48/8) [III]***	***Lam. Steel (12/8) [IV]***	***SMC (12/8) [V]***	***Inference [III vs. V] [IV vs. V]***
Stator core	Steel	SMC		Steel	Steel	SMC	
Stator OD [mm]	240	227	[5.41 % ↓]	170	182	170	[0 %] [6.66 % ↓]
Rotor OD [mm]	140	140		107	107	107	
Airgap length [mm]	1	1		1	1	1	
Stacking factor [%]	97	100		97	97	100	
Active stack length [mm]	85	85		125	125	125	
Overall stack length [mm]	111	85	[23.42 % ↓]	185	157	125	[32.4 % ↓] [20.3 % ↓]
Average torque [Nm]	20	20		20	20	20	
Current (rms) [A]	124.45	144.9		110.45	123.74	131.52	
Current density (rms) [A/mm^2]	5	5		5	5	5	
Slot fill factor [%]	40	60		40	40	60	
Phase resistance [Ω]	0.002	0.0017	[15 % ↓]	0.006157	0.004369	0.004002	[35 % ↓] [8.4 % ↓]
Copper loss (3400 rpm) [W]	92.92	107.16	[14.24 W ↑]	225.33	200.73	207.72	[17.61 W ↓] [6.99 W ↑]
Stator iron loss (3400 rpm) [W]	199.39	316.73		72.91	95.69	190.03	
Rotor iron loss (3400 rpm) [W]	0.55	0.56		0.001	0.145	0.134	
Total loss (3400 rpm) [W]	292.86	424.45	[131.59 W ↑]	298.24	296.56	397.884	[99.64 W ↑] [101.32 W ↑]
Copper loss (10000 rpm) [W]	92.9	107		-	200.1	207.53	
Iron loss (10000 rpm) [W]	1889.42	1533.99		-	808.27	918.88	
Total loss (10000 rpm) [W]	1982.32	1640.99	[341.33 W ↓]	-	1008.37	1126.41	[–] [118.04 W ↑]
Total weight [Kg]	25.06	23.79		19.55	22.41	20.30	
Power density (motor vol.) [kW/m^3]	1418.04	2069.76	[45.95 % ↑]	1695.64	1743.38	2509.69	[48.0 % ↑] [43.95 % ↑]
TRV (rotor vol.) [kW/m^3]	15.29	15.29	[-]	17.79	17.79	17.79	[-]
Torque density (motor vol.) [kW/m^3]	3.98	5.81	[45.97 % ↑]	4.76	4.89	7.04	[47.89 % ↑] [43.96 % ↑]

5.4. Ring-type Halbach-Array Rotor PM Topology

As discussed in the previous section, a high pole number increases the supply frequency, which is suitable for the SMC-based stator core as its eddy current losses are lower compared to the laminated steel core. However, the 7.12 kW SMC-based stator core with 12 slots and 8-pole configurations is considered for further analysis as a trade-off between the performance and manufacturing cost of the machine. The rated torque is 20 Nm with a base speed of 3400 rpm. The rotor with surface-mounted PM requires retention sleeves to prevent movement of the magnet during high-speed operation. Therefore, banding and gluing the PM further increases the cost and complexity of the manufacturing process. Whereas, the PM buried in the rotor core increases the magnet leakage flux and these PMs are mostly pre-magnetized, which need extreme care while inserting into the rotor core. Therefore, the cold spray additive manufacturing technique helps to fabricate the PM rotor of complex shape directly on the rotor core surface without the need for these additional steps. But these PMs need to be magnetized either using a stator core as a magnetizer or an additional magnetizer hardware setup needs to be built. For high-speed application, the ring-type PM is analyzed in this chapter as shown in Fig. 5.11 (a). The ring-type PM can be easily fabricated using the cold spray technique without much material wastage. As the PM is continuous and forming a ring shape, the risk of rotor PM pole movement is lower and can be used at high speeds.

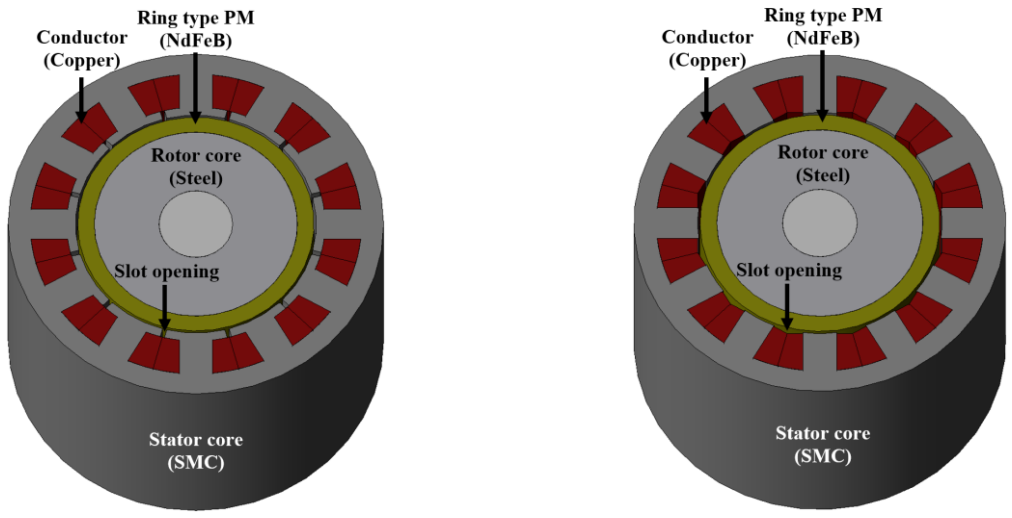

(a) (b)

Fig. 5.11: Isometric view of 12 slots and 8-pole with ring-type Halbach-array cold spray rotor PM and SMC stator core. (a) with stator tooth tip (b) without stator tooth tip

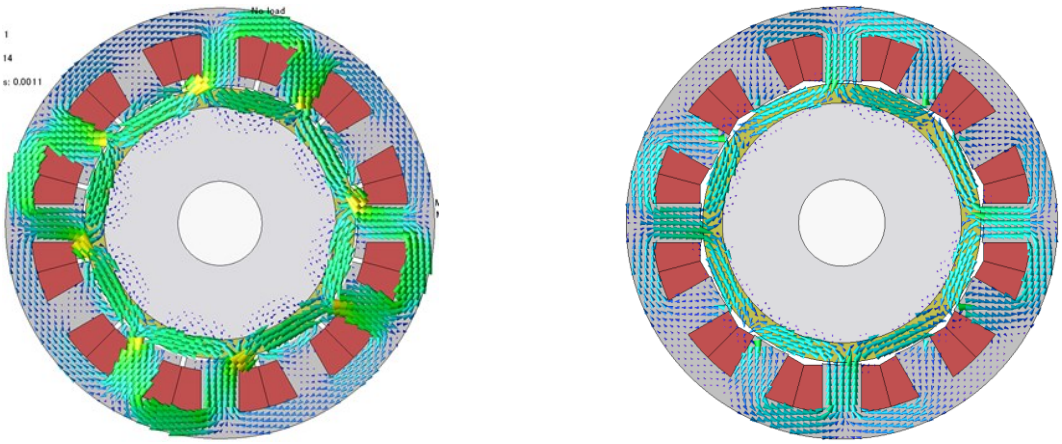

(a) (b)

Fig. 5.12: Magnetic flux path at no-load for 12 slots and 8-pole with ring-type Halbach-array cold spray rotor PM and SMC stator core. (a) with stator tooth tip (b) without stator tooth tip

To reduce the magnet leakage flux and to improve the magnet area utilization, the rotor is magnetized as Halbach-array configuration as shown in Fig. 5.12 (a). The flux path of Halbach-array PM is in tangential directional to the rotor instead of radial direction as of the conventional surface PM machine. Hence, the tooth tip of the stator core carries the large leakage flux as shown in Fig. 5.12 (a) and hence it affects the back EMF of the machines and the average electromagnetic torque is reduced to 16.9 Nm with the torque ripple of 38.76 % as shown in Fig. 5.13 and 5.14. To avoid these leakage fluxes, the tooth-tip of the machine is eliminated as shown in Fig. 5.11 (b). It helps to conduct the magnetic flux path around the stator coil windings and eliminates the flux leakage through the stator core as shown in Fig. 5.12 (b). Therefore, the effective interaction of the magnet flux and armature flux increases which leads to an increase in the average electromagnetic torque. Therefore, average torque is improved to the required rated average torque which is 20.03 Nm with a torque ripple of 32.20 %. The optimal angle to reduce the cogging torque for 12 slots and 8-pole configurations is 15°. Therefore, after skewing the SMC-based stator core, the torque ripple is reduced to 3.2 % with an average electromagnetic torque of 20 Nm. The back EMF of the machine further improves, and its total harmonic distortion analysis is done as shown in Fig. 5.15. The THD in the phase back EMF for stator with a tooth tip thickness of 4 mm is 14.15 % with the fundamental peak voltage of 21.87 V. The THD in the phase back EMF is optimized and reduced to 5.79 % by increasing the slot-opening of the stator tooth design. Finally, with the help of skewing the stator core by 15°, the THD of the phase back EMF is further reduced to 2.04 % with the fundamental peak voltage of 24.16 V.

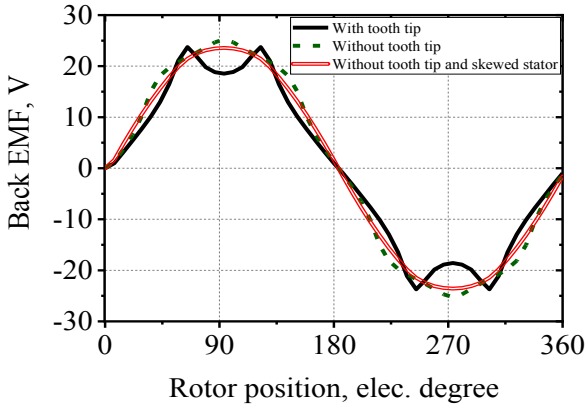

Fig. 5.13: Back EMF for 12 slots and 8-pole with ring-type Halbach-array cold spray rotor PM and SMC stator core

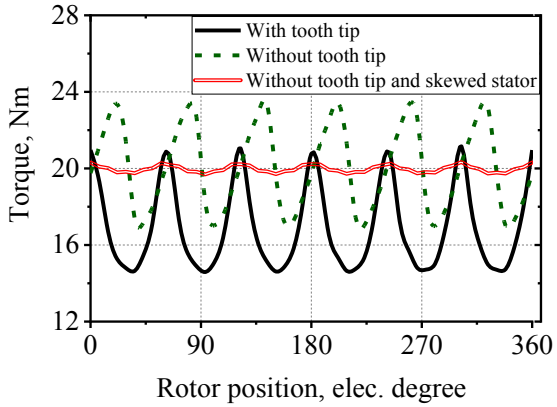

Fig. 5.14: Electromagnetic torque for 12 slots and 8-pole with ring-type Halbach-array cold spray rotor PM and SMC stator core

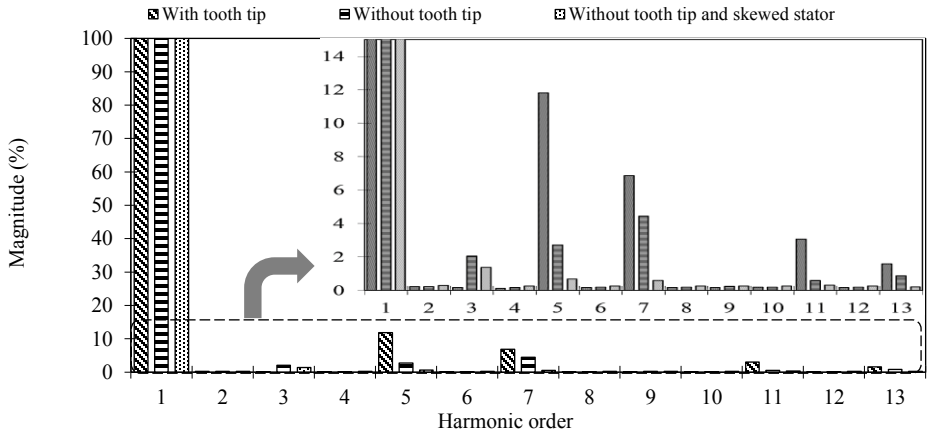

Fig. 5.15: FFT analysis of the phase back EMF for 12 slots and 8-pole with ring-type Halbach-array cold spray rotor PM and SMC stator core

For laboratory testing purposes, a scaled-down design of a 10-pole ring-type PM rotor is designed for the 12 slots SMC stator core as shown in Fig. 5.16. Since the PM material is in powder form, the effectiveness of the cold spray PM material sticking on the rotor core surface needs to be verified. Therefore, different lamination thicknesses of the rotor core are analyzed such as 0.35 mm, 0.5 mm, 0.65 mm, and complete solid steel cores. Since the rotor is rotating at a synchronous speed, the magnitude of rotor core loss is low compared to stator core loss because of its constant field flux density. Also, the ring-type PM considered in the simulated design is arranged in a Halbach pattern, therefore the flux lines passing through the rotor core are lower as shown in Fig. 5.16. The rotor core loss for the different lamination thicknesses at base speed and maximum speed is as shown in Fig. 5.17 (a) and (b).

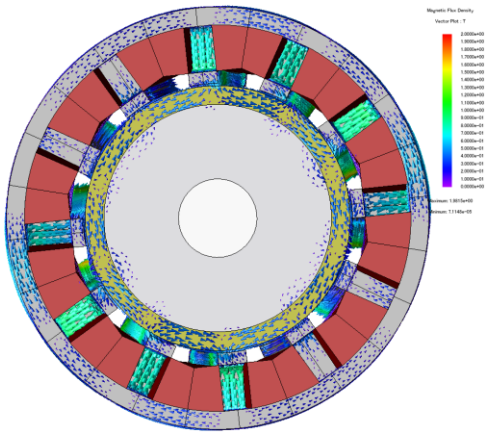

Fig. 5.16: Magnetic flux path at no-load for 12 slots and 10-pole with ring-type Halbach-array cold spray rotor PM and SMC stator core

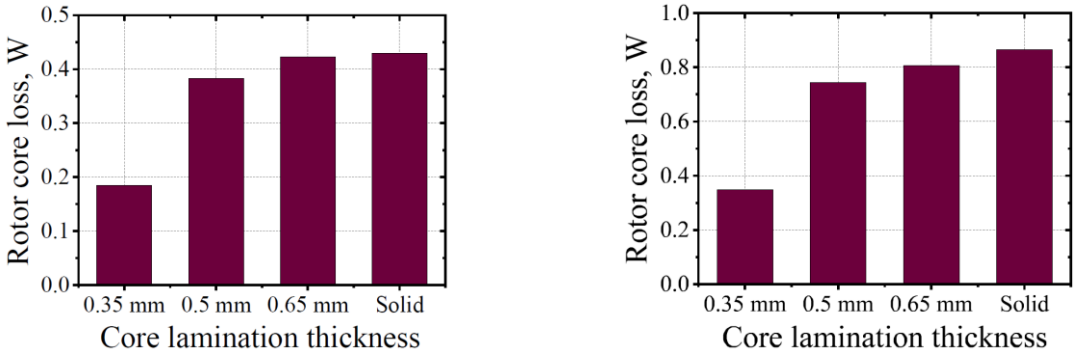

(a) (b)

Fig. 5.17: Rotor core loss for 10-pole with ring-type Halbach-array cold spray rotor PM at different core lamination thickness. (a) At a base speed of 3400 rpm. (b) At a maximum speed of 10,000 rpm

It can be observed that the overall rotor core losses are negligible compared to the total loss of the machine, but it increases with the core lamination thickness. Hence, it can be concluded that for the cold spray additive manufacturing of PM materials, a solid steel rotor core can also be considered as the rotor core losses are not significantly increased compared to the laminated rotor cores. The back EMF and electromagnetic torque of the 12/10 slot-pole design with a laminated steel thickness of 0.35 mm and SMC stator core at the rated speed of 3400 rpm are as shown in Fig. 18 and 19. The average electromagnetic torque is 11.84 Nm with a torque ripple of 2.26 %.

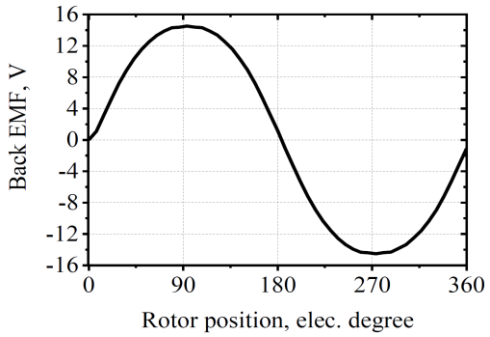

Fig. 5.18: Back EMF for 12 slots and 10-pole with ring-type Halbach-array cold spray rotor PM and SMC stator core

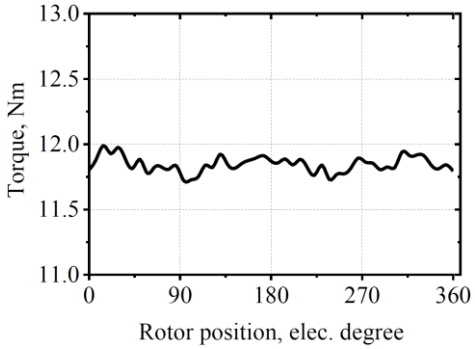

Fig. 5.19: Electromagnetic torque for 12 slots and 10-pole with ring-type Halbach-array cold spray rotor PM and SMC stator core

5.5. Conclusions

This chapter has presented a comparison between the laminated steel core and the SMC stator core for the 7.12 kW design with a base speed of 3400 rpm and a maximum speed of 10,000 rpm. A various configuration such as a high pole number of 20-pole with 24 slots and a low number of 8-pole with 12 slots and 48 slots is considered for analysis. The SMC design with a 20-pole

design is suitable for the high-speed traction application as its overall total core losses are less compared to the laminated steel core design. The SMC-based core helps to improve the torque density of the machine by 45.97 % for the 24/20 design and by 47.89 % and 43.96 % for the 48/8 and 12/8 design respectively which is one of the key parameters for the electric vehicle design. The concentrated winding with the SPP 2/5, helps to achieve a wider constant-power speed ratio for the surface-mounted PM machines. The overall stack length and the weight of the copper are reduced in the SMC-based stator core due to the compact end turns. As windings are tooth wounds, the copper fill factor for SMC-based core is increased to 60 % to achieve better performance. The cold spray additive manufacturing technique helps to directly fabricate the shaped PM with less material wastage. The surface-mounted 8-pole ring-type Halbach-array rotor PM for high-speed application was designed and optimized to improve its THD in the back EMF and torque ripple. The THD in the phase back EMF is reduced by 85.58 % and the electromagnetic torque ripple is reduced by 90.06 %. Also, the scaled-down model of the 10-pole ring-type rotor design with the different rotor core lamination is analyzed. Usage of SMC-based core and cold-spray additively manufactured PM enhances the motor performance by improving the design and flexibility in the shape of the machine parts.

CHAPTER – 6

CONCLUSIONS AND FUTURE WORK

The purpose of this thesis was to design a permanent magnet-based traction motor topologies to leverage the additively manufacturing cold-spray PM technique and enhance its performance using advanced magnetic material such as soft magnetic composites in the stator core.

6.1. Conclusions

A literature review of permanent magnet electric motors in chapter 1 showed that electric vehicles (EVs) and hybrid electric vehicles (HEVs) have emerged as viable solutions in the transportation sector. The usage of permanent magnets for various applications has tremendously increased the development and improvement of permanent magnet materials, especially rare-earth magnets.

Electric vehicles demand lower torque pulsation and vibrations in the machines as it can lead to a harsh driving experience for passengers. One of the effective ways to reduce torque pulsations is the modification and optimization of permanent magnet geometry as its shape and flux leakage have a significant effect on cogging torque. A literature review on the usage of advanced magnetic material such as soft magnetic composites (SMC) showed that it increases the design and flexibility in the shape of the motor parts and hence enhances the motor performance.

The magnitude and shape of the back EMF waveform depends on the magnetic flux linkage as well as its cross-sectional area. An analysis was performed by deriving the flux linkage for one pole with a fully pitched coil and then Faraday's law was applied to calculate the back EMF for conventional rectangular-shaped unskewed permanent magnet rotor (Model A) and petal-shaped permanent magnet rotor (Model C).

As the cold spray additively manufactured rotor PMs are initially in a non-magnetized state. A FEM-based magnetic field simulation approach was used to calculate the magnitude of the magnetization current at which the rotor PM is saturated.

The 3-D finite element electromagnetic performance analysis was performed for three different rotor topologies with conventional rectangular-shaped skewed and unskewed permanent magnet rotors (Model A and Model B) and petal-shaped permanent magnet rotor (Model C). The THD in the simulated phase back EMF for Model C is 0.69 % and the torque ripple is 1.3 % which is the lower when compared to Models A and B.

As the number of coil turns in the winding is kept the same, the magnetic flux linkage for Model C was lower due to the reduced magnet volume and the flux leakage at the edges of the sinusoidal-petal-shaped rotor poles. Hence, the average simulated electromagnetic torque of Model C is reduced by 6.8 % compared to Model A with unskewed rotor PM.

For the in-situ impulse magnetizer test prototype, various stator terminal connection configurations such as star, delta, and parallel were analyzed and compared. For $V_{dc} = 1000\ V$, it was evident that the parallel connection provides the highest value of $I_{\alpha} = 2000\ A$ which in turn results in the highest magnetizing field strength. However, the peak current drawn from the magnetizer was the highest for the parallel connection scheme. Hence, the power handling components in the magnetizer need to be rated for high current. For the star configuration, the value of $I_{\alpha} = 1000\ A$ which was higher than the peak current from the magnetizer, $I_p = 667\ A$. But the effective resistance R_{eff} offered by the winding to the magnetizer was high. In the delta configuration, the effective resistance is low compared to star configuration and can generate a higher value of I_p for the same V_{dc}. But the value of I_{α} is the same as the value of I_p. Therefore, a delta connection was used for magnetization and its flux density distribution profile on the surface of the magnets was analyzed using a hall probe.

The cold spray rotor for Model A with unskewed, Model B with skewed PM, and Model C with sinusoidal-petal shaped PM were all prototyped using cold spray additive manufacturing and machined to final dimensions. After the magnetization, it was observed that the edges of the magnet were not magnetized fully when compared to the center region. This was due to the fact that the magnetic field generated by the stator coils is concentrated at the center of each pole. In addition, the center region was also magnetized non-uniformly. This non-uniform magnetization was due to the effect of stator teeth openings where the magnetic field was low. To address these issues and improve the back-EMF, the surface PM pole rotor d-axis is aligned and rotated in both

clockwise and anti-clockwise directions by half slot-pitch that was by 5° mechanical, and again the magnetization pulse was supplied to the stator windings.

The experimental electromagnetic analysis such as back EMF, rated torque, and cogging torque was measured and compared. The THD in the measured phase back EMF for Model C is 3.07 % and the measured torque ripple is 9.31 % which is the least compared to Model A and B. The measured average electromagnetic torque of Model C is reduced by 17.2 % compared to Model A with unskewed rotor PM.

The measured results do not match with the FEA simulated results perfectly however, the experimental comparison is valid as the same test procedure was used in all three models. This experimental analysis validates that the cold spray additive manufacturing technique can lead to an improvement of the motor performance by improving the design flexibility of the machine parts such as rotor PM shape and can also be used for powdered-based fabrication of the stator and rotor.

The impact of a few manufacturing parameters on SMC properties to ensure that optimized motor performance is achieved was analyzed using three SMC materials (A, B, and C) in 3-D FEA software. The armature current of the 15 kW surface-mounted PMSM was adjusted for each case to maintain an average torque of 100 N.m. The FEA results showed that material A, with high resistivity and low permeability, limits the SMC eddy current loss, but it also caused the highest copper and hysteresis losses. On the other hand, the high permeability material C achieves the lowest copper and hysteresis losses. However, its low resistivity caused significant SMC global eddy currents that result in the highest overall motor losses. Material B with its medium permeability, resistivity, and hysteresis loss achieved the lowest overall motor losses and achieved the highest efficiency.

Also, the optimal flux weakening in the 7.12 kW surface-mounted PMSM was analyzed. The desired magnet flux linkage and d-axis inductance were obtained analytically which served as a target toward which the machine design parameters such as the winding configuration, the number of turns, air gap length, stator tooth width, and back iron width were finalized in the FEA software to obtain a wide constant power speed range.

Direct replacement of the electrical laminated steel cores with SMC cores will not improve the performance of the machines. Therefore, an FEA-based study is performed for a 7.12 kW surface-mounted PMSM with 24/20 slot-pole and 12/8 slot-pole configurations with a base speed of 3400 rpm and a maximum speed of 10,000 rpm in chapter 5. It was observed that the overall stack length of the 24/20 slot-pole design with SMC stator core is reduced by 23.42 % compared to its design with laminated steel core due to compact end-turns. Similarly, for the 12/8 slot-pole design with SMC stator core, 32.4 % and 20.3 % reduction in overall stack length compared to 48/8 and 12/8 slot-pole designs with laminated steel core respectively.

The phase resistance of both the designs with SMC stator core was reduced due to short copper winding length, but the conductors per slot increased as the fill factor was increased to 60 %. The total losses for a high number of pole designs that is 24/20 slot-pole with SMC stator core at maximum speed were lower due to reduced eddy current loss compared to the laminated steel core. Therefore, it was observed that SMC materials perform better at high-frequency in terms of core losses.

The overall volume of the machine with SMC stator core design for both 24/20 and 12/8 slot-pole was reduced. In the case of 20 poles with 24 slots design the torque density was increased by 45.97 % and for 8 poles with 48 slots and 12 slots design, it was increased by 47.89 % and 43. 96 % respectively. Therefore, considering the high-speed traction application, usage of SMC materials to build machine parts helps to improve the torque density, reduces the copper wastage and weight also reduces the core losses in PM machines.

For high-speed applications, the ring-type Halbach-array rotor PM using the cold spray technique was also analyzed in chapter 5. Due to the flux path of Halbach-array PM being in a tangential direction to the rotor core, the electromagnetic performance of the motor was improved by modifying the tooth-tip of the stator core in order to reduce its flux leakage. The THD of the phase back EMF was reduced to 2.04 % and torque ripple was reduced to 3.2 % with an average electromagnetic torque of 20 Nm.

6.2. Proposed Future Work

- An inset petal-shape rotor or buried shaped PM topology using the cold spray technique can be designed to further improve the electromagnetic performance of the PM machines.
- The residual flux density of the permanent magnets fabricated using additively manufactured cold spray technique has to be improved.
- Improvements in the magnetization prototype and test procedure for the cold-spray PM can lead to uniform magnetization and further enhance motor performance.
- Intensive research work has to be done on the composition of soft magnetic composites materials to improve its permeability and mechanical strength.
- Usage of Litz wire or rectangular copper conductors in the SMC-based design will improve the slot fill-factor and thermal performance of the machines.

REFERENCES

Chapter 1:

[1] B. Bilgin and A. Emadi. “Electric motors in electrified transportation: A step toward achieving a sustainable and highly efficient transportation system,” IEEE Power Electronics Magazine, volume. 1, no. 2, pp. 10-17, (2014).

[2] B. Bilgin, P. Magne, P. Malysz, Y. Yang, V. Pantelic, M. Preindl, A. Korobkine, W. Jiang, M. Lawford, and A. Emadi, "Making the case for electrified transportation," IEEE Transactions on Transportation Electrification, vol. 1, no. 1, pp. 4-17, 2015.

[3] Z.Q. Zhu and David Howe, "Electrical machines and drives for electric, hybrid, and fuel cell vehicles," in Proceedings of the IEEE, vol. 95, no. 4, pp. 746-765, 2007.

[4] Automotive industry, [Online]. Available: https://en.wikipedia.org/wiki/Automotive_industry

[5] F. Ahmed, E. Ghosh, S. Mukundan, H. Dhulipati, and N. C. Kar, “LPTN and FEA Modeling for Thermal Characterization of an Interior Permanent Magnet Synchronous Motor (IPMSM) for Electric Vehicle Application,” in the Proc. of 2018 Energy & Sustainability Symposium, Windsor, ON, June 2018

[6] A. Mollaeian, E. Ghosh, H. Dhulipati, J. Tjong and N. C. Kar, "3-D Sub-Domain Analytical Model to Calculate Magnetic Flux Density in Induction Machines With Semiclosed Slots Under No-Load Condition," in IEEE Transactions on Magnetics, vol. 53, no. 6, pp. 1-5, June 2017

[7] E. Ghosh, F. Ahmed, A. Mollaeian, J. Tjong and N. C. Kar, "Online Parameter Estimation and Loss Calculation Using Duplex Neural — Lumped Parameter Thermal Network for Faulty Induction Motor," in the Proc. of IEEE Conference on Electromagnetic Field Computation (CEFC), pp. 1-1, Miami, FL, 2016.

[8] E. Ghosh, A. Mollaeian, W. Hu and N. C. Kar, " A Novel Control Strategy for Online Harmonic Compensation in Parametrically Unbalanced Induction Motor," in the Proc. of 2016 IEEE International Magnetics Conference, pp. 1-1, San Diego, 2016.

[9] F. Ahmed, E. Ghosh and N. C. Kar, "Transient Thermal Analysis of a Copper Rotor Induction Motor Using a Lumped Parameter Temperature Network Model," in the Proc. of IEEE Transportation Electrification Conference and Expo, pp. 1-6, Dearborn, MI, 2016.

[10] Libert, F. “Design, Optimization and Comparison of Permanent Magnet Motors for a Low-Speed Direct-Driven Mixer.” (2004).

[11] J. F. Gieras and M. Wing, Permanent Magnet Motor Technology (Design and Application), Marcel Dekker Inc, second edition, revised and expanded ed.,2002.

[12] Hard magnets made easy. Stanley R. Trout, Molycorp Minerals, LLC Greenwood Village, CO 80111 USA

[13] M.J. Kramer, R. W. McCallum, I. A. Anderson, and S. Constantinides, “Prospects for Non-Rare Earth Permanent Magnets for Traction Motors and Generators,” The Journal of The Minerals, Metals & Materials Society, vol. 64, issue 7, pp. 752-763, July 2012

[14] https://www.hsmagnets.com/support/physical-properties/

[15] https://etn-demeter.eu/rotor-shaping-technologies-for-permanent-magnet-electrical-machines/

[16] Lamarre, J., Bernier, F. Permanent Magnets Produced by Cold Spray Additive Manufacturing for Electric Engines. J Therm Spray Tech 28, 1709–1717 (2019)

[17] Zhang, B. Soft Magnetic Composites in Novel Designs of Electrical Traction Machines. KIT Scientific Publishing, 2017

[18] Boehm and I. Hahn, "Comparison of soft magnetic composites (SMCs) and electrical steel," 2012 2nd International Electric Drives Production Conference (EDPC), 2012, pp. 1-6

Chapter 2:

[19] F. Ahmed, E. Ghosh, S. Mukundan, H. Dhulipati, and N. C. Kar, “LPTN and FEA Modeling for Thermal Characterization of an Interior Permanent Magnet Synchronous Motor (IPMSM)

for Electric Vehicle Application," in the Proc. of 2018 Energy & Sustainability Symposium, Windsor, ON, June 2018

[20] Y. Yang et al., "Design and Comparison of Interior Permanent Magnet Motor Topologies for Traction Applications," in IEEE Transactions on Transportation Electrification, vol. 3, no. 1, pp. 86-97, March 2017

[21] Automotive industry, [Online]. Available: https://en.wikipedia.org/wiki/Automotive_industry

[22] S. Q. A. Shah, T. A. Lipo and B. Kwon, "Modeling of Novel Permanent Magnet Pole Shape SPM Motor for Reducing Torque Pulsation," in IEEE Transactions on Magnetics, vol. 48, no. 11, pp. 4626-4629, Nov. 2012.

[23] W. Zhao, T. A. Lipo and B. Kwon, "Material-Efficient Permanent-Magnet Shape for Torque Pulsation Minimization in SPM Motors for Automotive Applications," in IEEE Transactions on Industrial Electronics, vol. 61, no. 10, pp. 5779-5787, Oct. 2014.

[24] Z. S. Du and T. A. Lipo, "High Torque Density and Low Torque Ripple Shaped-Magnet Machines Using Sinusoidal Plus Third Harmonic Shaped Magnets," in IEEE Transactions on Industry Applications, vol. 55, no. 3, pp. 2601-2610, May-June 2019.

[25] Z. Yang, F. Shang, I. P. Brown and M. Krishnamurthy, "Comparative Study of Interior Permanent Magnet, Induction, and Switched Reluctance Motor Drives for EV and HEV Applications," in IEEE Transactions on Transportation Electrification, vol. 1, no. 3, pp. 245-254, Oct. 2015

[26] Z. Yang, F. Shang, I. P. Brown and M. Krishnamurthy, "Comparative Study of Interior Permanent Magnet, Induction, and Switched Reluctance Motor Drives for EV and HEV Applications," in IEEE Transactions on Transportation Electrification, vol. 1, no. 3, pp. 245-254, Oct. 2015

[27] Y. Jiang, Z. Yang and M. Krishnamurthy, "Optimal design considerations for interior permanent magnet motor for a range-extended electric vehicle," 2013 IEEE Transportation Electrification Conference and Expo (ITEC), 2013, pp. 1-6

[28] W. Deng and S. Zuo, "Electromagnetic Vibration and Noise of the Permanent-Magnet Synchronous Motors for Electric Vehicles: An Overview," in IEEE Transactions on Transportation Electrification, vol. 5, no. 1, pp. 59-70, March 2019

[29] M. Salameh, S. Yaman, Y. Jiang, M. Krishnamurthy and S. Li, "Analytical Approach for Calculating Magnetic Field Distribution in Surface Mount PM Motor Including Stator Slot Effect," 2019 IEEE Transportation Electrification Conference and Expo (ITEC), 2019

[30] Zhi Yang, S. Yaman and M. Krishnamurthy, "Mitigation of electromagnetic vibration in PMSM: A rotor position related variable switching frequency technique," 2017 IEEE Transportation Electrification Conference and Expo (ITEC), 2017, pp. 448-452

[31] M. Ibrahim, F. Bernier and J. Lamarre, "Design of a PM-Assisted Synchronous Reluctance Motor Utilizing Additive Manufacturing of Magnetic Materials," 2019 IEEE Energy Conversion Congress and Exposition (ECCE), Baltimore, MD, USA, 2019, pp. 1663-1668.

[32] Lamarre, J., Bernier, F. Permanent Magnets Produced by Cold Spray Additive Manufacturing for Electric Engines. J Therm Spray Tech 28, 1709–1717 (2019)

[33] D. G. Dorrell, M. -. Hsieh and Y. -. Hsu, "Post Assembly Magnetization Patterns in Rare-Earth Permanent-Magnet Motors," in IEEE Transactions on Magnetics, vol. 43, no. 6, pp. 2489-2491, June 2007

[34] S. Singh and P. Pillay, "Sinusoidal Shaped Surface Permanent Magnet Motor Using Cold Spray Additive Manufacturing," 2020 IEEE Energy Conversion Congress and Exposition (ECCE), Detroit, MI, USA, 2020, pp. 2089-2094

[35] M. Ibrahim, F. Bernier and J. -M. Lamarre, "Novel Multi-layer Design and Additive Manufacturing Fabrication of a High Power Density and Efficiency Interior PM Motor," 2020 IEEE Energy Conversion Congress and Exposition (ECCE), 2020, pp. 3601-3606

[36] M. Ibrahim, F. Bernier and J. -M. Lamarre, "A Novel Toroidal Permanent Magnet Motor Structure with High Torque Density and Enhanced Cooling," 2020 IEEE Energy Conversion Congress and Exposition (ECCE), 2020, pp. 4044-4049

[37] S. Oh, S. Min and J. Hong, "Air Gap Flux Density Waveform Design of Surface-Mounted Permanent Magnet Motor Considering Magnet Shape and Magnetization Direction," in IEEE Transactions on Magnetics, vol. 49, no. 5, pp. 2393-2396, May 2013

[38] B. Bilgin and A. Emadi. “Electric motors in electrified transportation: A step toward achieving a sustainable and highly efficient transportation system,” IEEE Power Electronics Magazine, volume. 1, no. 2, pp. 10-17, (2014).

[39] B. Bilgin, P. Magne, P. Malysz, Y. Yang, V. Pantelic, M. Preindl, A. Korobkine, W. Jiang, M. Lawford, and A. Emadi, "Making the case for electrified transportation," IEEE Transactions on Transportation Electrification, vol. 1, no. 1, pp. 4-17, 2015.

[40] https://www.jmag-international.com/

Chapter 3:

[41] R. Wrobel and B. Mecrow, “A Comprehensive Review of Additive Manufacturing in Construction of Electrical Machines,” in IEEE Transactions on Energy Conversion, vol. 35, no. 2, pp. 1054-1064, June 2020

[42] M. Hsieh, Y. Lien and D. G. Dorrell, “Post-Assembly Magnetization of Rare-Earth Fractional-Slot Surface Permanent-Magnet Machines Using a Two-Shot Method,” in IEEE Transactions on Industry Applications, vol. 47, no. 6, pp. 2478-2486, Nov.-Dec. 2011

[43] Q. Wang et al., “Research of Post-Assembly Magnetization of LargePower Surface-Mounted Rare-Earth Permanent Magnet Machines With Integrated Magnetizing Winding,” in IEEE Transactions on Applied Superconductivity, vol. 30, no. 4, pp. 1-5, June 2020

[44] L. Chang, T. R. Eastham and G. E. Dawson, "In-situ magnetization of NdFeB magnets for permanent magnet machines," in IEEE Transactions on Magnetics, vol. 27, no. 5, pp. 4355-4359, Sept. 1991

[45] Pill-Soo Kim and Yong Kim, "Part I-circuit, thermal and cost modeling of impulse magnetizer, "Proceedings of the IEEE 1999 International Conference on Power Electronics and Drive Systems. PEDS'99 (Cat. No.99TH8475), 1999, pp. 371-376 vol.1

[46] S. B. Sriveni, V. K. Chinnaiyan and J. Jerome, "A simple low cost energy efficient magnetizer for industrial applications," 2006 India International Conference on Power Electronics, 2006, pp. 94-97

[47] M. Hsieh, Y. Lien and D. G. Dorrell, "Post-Assembly Magnetization of Rare-Earth Fractional-Slot Surface Permanent-Magnet Machines Using a Two-Shot Method," in IEEE Transactions on Industry Applications, vol. 47, no. 6, pp. 2478-2486, Nov.-Dec. 2011

[48] F.Bernier, M. Ibrahim, M. Mihai, Y, Thomas, J.M. Lamarre, "Additive manufacturing of soft and hard magnetic materials used in electrical machines" vol. 75 (6), pp. 334-343.

[49] JMAG-Designer, (2018-2019), Available: https://www.jmaginternational.com/products/jmag-designer/.

[50] Vishay appnote: Shunts, Current Shunts, And Current-Sensing Resistors, www.vishay.com/docs/49159/_power-metal-strip-shunts-currentshunts_pl0005-1801.pdf

[51] G. W. Jewell, D. Howe and C. D. Riley, "The design of radial-field multipole impulse magnetizing fixtures for isotropic NdFeB magnets," in IEEE Transactions on Magnetics, vol. 33, no. 1, pp. 708-722, Jan. 1997

Chapter 4:

[52] Z. Q. Zhu and D. Howe, "Electrical Machines and Drives for Electric, Hybrid, and Fuel Cell Vehicles," in Proceedings of the IEEE, vol. 95, no. 4, pp. 746-765, April 2007

[53] A. M. El-Refaie, "Motors/generators for traction/propulsion applications: A review," in IEEE Vehicular Technology Magazine, vol. 8, no. 1, pp. 90- 99, March 2013

[54] I. Boldea, L. N. Tutelea, L. Parsa and D. Dorrell, "Automotive electric propulsion systems with reduced or no permanent magnets: An overview," in IEEE Transactions on Industrial Electronics, vol. 61, no. 10, pp. 5696-5711, Oct. 2014

[55] J. de Santiago et al., "Electrical Motor Drivelines in Commercial AllElectric Vehicles: A Review," in IEEE Transactions on Vehicular Technology, vol. 61, no. 2, pp. 475-484, Feb. 2012

[56] W. Cao, B. C. Mecrow, G. J. Atkinson, J. W. Bennett and D. J. Atkinson, "Overview of electric motor technologies used for more electric aircraft (MEA)," in IEEE Transactions on Industrial Electronics, vol. 59, no. 9, pp. 3523-3531, Sept. 2012

[57] E. A. Jones, F. F. Wang and D. Costinett, "Review of Commercial GaN Power Devices and GaN-Based Converter Design Challenges," in IEEE Journal of Emerging and Selected Topics in Power Electronics, vol. 4, no. 3, pp. 707-719, Sept. 2016

[58] N. Bianchi, S. Bolognani and F. Luise, "Potentials and limits of highspeed PM motors," in IEEE Transactions on Industry Applications, vol. 40, no. 6, pp. 1570-1578, Nov.-Dec. 2004

[59] A. Krings, A. Boglietti, A. Cavagnino and S. Sprague, "Soft Magnetic Material Status and Trends in Electric Machines," in IEEE Transactions on Industrial Electronics, vol. 64, no. 3, pp. 2405-2414, March 2017

[60] A. Schoppa and P. Delarbre, "Soft Magnetic Powder Composites and Potential Applications in Modern Electric Machines and Devices," in IEEE Transactions on Magnetics, vol. 50, no. 4, pp. 1-4, April 2014.

[61] C. Liu, G. Lei, T. Wang, Y. Guo, Y. Wang and J. Zhu, "Comparative Study of Small Electrical Machines With Soft Magnetic Composite Cores," in IEEE Transactions on Industrial Electronics, vol. 64, no. 2, pp. 1049-1060, Feb. 2017

[62] A. G. Jack et al., "Permanent-magnet machines with powdered iron cores and prepressed windings," in IEEE Transactions on Industry Applications, vol. 36, no. 4, pp. 1077-1084, July-Aug. 2000

[63] C. Kim, G. Jang, J. Kim, J. Ahn, C. Baek and J. Choi, "Comparison of Axial Flux Permanent Magnet Synchronous Machines With Electrical Steel Core and Soft Magnetic Composite Core," in IEEE Transactions on Magnetics, vol. 53, no. 11, pp. 1-4, Nov. 2017

[64] T. J. Woolmer and M. D. McCulloch, "Analysis of the Yokeless and Segmented Armature Machine," 2007 IEEE International Electric Machines & Drives Conference, Antalya, 2007, pp. 704-708

[65] Y. Wang, J. Lu, C. Liu, G. Lei, Y. Guo and J. Zhu, "Development of a High-Performance Axial Flux PM Machine With SMC Cores for Electric Vehicle Application," in IEEE Transactions on Magnetics, vol. 55, no. 7, pp. 1-4, July 2019

[66] F. Marignetti and V. Delli Colli, "Thermal Analysis of an Axial Flux Permanent-Magnet Synchronous Machine," in IEEE Transactions on Magnetics, vol. 45, no. 7, pp. 2970-2975, July 2009

[67] J. G. Zhu, Y. G. Guo, Z. W. Lin, Y. J. Li and Y. K. Huang, "Development of PM Transverse Flux Motors With Soft Magnetic Composite Cores," in IEEE Transactions on Magnetics, vol. 47, no. 10, pp. 4376-4383, Oct. 2011

[68] J. Cros and P. Viarouge, "New structures of polyphase claw-pole machines," in IEEE Transactions on Industry Applications, vol. 40, no. 1, pp. 113-120, Jan.-Feb. 2004

[69] R. P. Deodhar, A. Pride and J. J. Bremner, "Design Method and Experimental Verification of a Novel Technique for Torque Ripple Reduction in Stator Claw-Pole PM Machines," in IEEE Transactions on Industry Applications, vol. 51, no. 5, pp. 3743-3750, Sept.-Oct. 2015

[70] Y. Guo, J. Zhu and D. G. Dorrell, "Design and Analysis of a Claw Pole Permanent Magnet Motor With Molded Soft Magnetic Composite Core," in IEEE Transactions on Magnetics, vol. 45, no. 10, pp. 4582-4585, Oct. 2009

[71] JMAG Version 19.1 Material library, JSOL Corporation, Tokyo, Japan, 2020

[72] JMAG Version 19.1 Reference Manual, Volume 1, 1st ed., JSOL Corporation, Tokyo, Japan, 2020

[73] A. M. EL-Refaie and T. M. Jahns, "Optimal flux weakening in surface PM machines using fractional-slot concentrated windings," in IEEE Transactions on Industry Applications, vol. 41, no. 3, pp. 790-800, May-June 2005

Chapter 5:

[74] T. Finken, M. Hombitzer and K. Hameyer, “Study and comparison of several permanent-magnet excited rotor types regarding their applicability in electric vehicles,” 2010 Emobility – Electrical Power Train, Leipzig, 2010, pp. 1-7.

[75] A. Chen, R. Nilssen and A. Nysveen, "Performance comparisons among radial flux, multi-stage axial flux and three-phase transverse flux PM machines for downhole applications," 2009 IEEE International Electric Machines and Drives Conference, Miami, FL, 2009, pp. 1010-1017

[76] Y. Wang and D. Gao, "A comparison of different types of motors used for low speed electric vehicles: Experiments and simulations," 2014 IEEE Conference and Expo Transportation Electrification Asia-Pacific (ITEC Asia-Pacific), Beijing, 2014, pp. 1-5

[77] C. Liu, J. Zhu, Y. Wang, G. Lei, Y. Guo and X. Liu, "Development of a novel axial-flux claw pole machine with soft magnetic composite core," 2015 IEEE International Magnetics Conference (INTERMAG), Beijing, 2015, pp. 1-1

[78] S. Singh and P. Pillay, "Sinusoidal Shaped Surface Permanent Magnet Motor Using Cold Spray Additive Manufacturing," 2020 IEEE Energy Conversion Congress and Exposition (ECCE), Detroit, MI, USA, 2020, pp. 2089-2094

[79] M. Ibrahim, F. Bernier and J. Lamarre, "Design of a PM-Assisted Synchronous Reluctance Motor Utilizing Additive Manufacturing of Magnetic Materials," 2019 IEEE Energy Conversion Congress and Exposition (ECCE), 2019, pp. 1663-1668

[80] M. Ibrahim, F. Bernier and J. -M. Lamarre, "Novel Multi-layer Design and Additive Manufacturing Fabrication of a High Power Density and Efficiency Interior PM Motor," 2020 IEEE Energy Conversion Congress and Exposition (ECCE), 2020, pp. 3601-3606

[81] M. Ibrahim, F. Bernier and J. -M. Lamarre, "A Novel Toroidal Permanent Magnet Motor Structure with High Torque Density and Enhanced Cooling," 2020 IEEE Energy Conversion Congress and Exposition (ECCE), 2020, pp. 4044-4049

[82] Lamarre, J., Bernier, F. Permanent Magnets Produced by Cold Spray Additive Manufacturing for Electric Engines. J Therm Spray Tech 28, 1709–1717 (2019)M. Young, The Technical Writer's Handbook. Mill Valley, CA: University Science, 1989.

[83] https://www.jmag-international.com/

[84] A. Boehm and I. Hahn, "Comparison of soft magnetic composites (smcs) and electrical steel", in Electric Drives Production Conference (EDPC), 2012 2nd International, Oct. 2012, pp. 1–6.

[85] H. Shokrollahi and K. Janghorban, "Soft magnetic composite materials (smcs)", Journal of Materials Processing Technology, vol. 189, no. 1, pp. 1–12, 2007.

[86] O. Andersson and P. Hofecker, "Advances in soft magnetic composites - materials and applications", PowderMet2009, pp. 1–12, Jul. 2009.

[87] Zhang, B. (2017) Soft Magnetic Composites in Novel Designs of Electrical Traction Machines. Karlsruhe: KIT Scientific Publishing.

[88] A. M. EL-Refaie and T. M. Jahns, "Optimal flux weakening in surface PM machines using fractional-slot concentrated windings," in IEEE Transactions on Industry Applications, vol. 41, no. 3, pp. 790-800, May-June 2005

APPENDIX – I

The simulation versus experimental performance comparison is tabulated as shown below.

Parameter	***Model A***		***Model B***		***Model C***	
	Simulation	Experimental	Simulation	Experimental	Simulation	Experimental
Magnet volume (%)	100 %	100 %	100 %	100 %	86.89 %	86.89 %
Phase back-EMF THD	8.87 %	7.50 %	5.27 %	6.24 %	1.35 %	3.07 %
Cogging torque (pk-pk)	1.9 Nm	1.2 Nm	0.156 Nm	1.2 Nm	0.13 Nm	0.78 Nm
Average torque	13.21 Nm	14.27 Nm	13.08 Nm	13.11 Nm	12.29 Nm	11.81 Nm
Torque ripple	23.08 %	19.27 %	7.33 %	18.68 %	1.46 %	9.31 %